

Experimental Investigation of Partial Cavitation

Jahangir, Saad

DOI

[10.4233/uuid:a855e51e-368f-4f0e-afc0-07acfe8da2b0](https://doi.org/10.4233/uuid:a855e51e-368f-4f0e-afc0-07acfe8da2b0)

Publication date

2020

Document Version

Final published version

Citation (APA)

Jahangir, S. (2020). *Experimental Investigation of Partial Cavitation*. [Dissertation (TU Delft), Delft University of Technology]. <https://doi.org/10.4233/uuid:a855e51e-368f-4f0e-afc0-07acfe8da2b0>

Important note

To cite this publication, please use the final published version (if applicable).
Please check the document version above.

Copyright

Other than for strictly personal use, it is not permitted to download, forward or distribute the text or part of it, without the consent of the author(s) and/or copyright holder(s), unless the work is under an open content license such as Creative Commons.

Takedown policy

Please contact us and provide details if you believe this document breaches copyrights.
We will remove access to the work immediately and investigate your claim.

**EXPERIMENTAL INVESTIGATION
OF PARTIAL CAVITATION**

EXPERIMENTAL INVESTIGATION OF PARTIAL CAVITATION

Proefschrift

ter verkrijging van de graad van doctor
aan de Technische Universiteit Delft,
op gezag van de Rector Magnificus prof. dr. ir. T.H.J.J. van der Hagen,
voorzitter van het College voor Promoties,
in het openbaar te verdedigen op dinsdag 9 juni 2020 om 15:00 uur

door

Saad JAHANGIR

Master of Science in Power Engineering
Brandenburg University of Technology Cottbus - Senftenberg, Germany
geboren te Lahore, Pakistan

Dit proefschrift is goedgekeurd door de

promotor: Prof. dr. ir. C. Poelma

promotor: Prof. dr. ir. J. Westerweel

Samenstelling promotiecommissie:

Rector Magnificus,

Prof. dr. ir. C. Poelma,

Prof. dr. ir. J. Westerweel,

voorzitter

Technische Universiteit Delft

Technische Universiteit Delft

Onafhankelijke leden:

Prof. dr. ir. K.T. Kiger,

Prof. dr. ir. H.W.M. Hoeijmakers,

Prof. dr. C.W.M. van der Geld,

Prof. dr. ir. T.J.C. van Terwisga,

Prof. dr. ir. J.T. Padding,

University of Maryland

Universiteit Twente

Technische Universiteit Eindhoven

Technische Universiteit Delft

Technische Universiteit Delft

This research was funded by Marie Curie Horizon 2020 Research and Innovation programme Grant 642536 'CaFE'.



Keywords: hydrodynamic cavitation, venturi, partial cavitation

Printed by: Gildeprint - Enschede

Front & Back: Space-time diagrams of partial cavitation regimes. Reproduced from International Journal of Multiphase Flow **106**, 34-45 (2018).

<https://doi.org/10.1016/j.ijmultiphaseflow.2018.04.019>.

Copyright © 2020 by S. Jahangir

ISBN 978-94-6366-280-2

An electronic version of this dissertation is available at

<http://repository.tudelft.nl/>.

To my family

CONTENTS

Summary	ix
Samenvatting	xi
1 Introduction	1
1.1 Cavitation	2
1.2 CaFE project	4
1.3 Partial cavitation	5
1.4 Selection of geometry	5
1.5 Flow characteristics in venturi	8
1.6 Research Structure	10
1.6.1 Chapter 2: Dynamics of partial cavitation in an axisymmetric converging-diverging nozzle	11
1.6.2 Chapter 3: Direct comparison of shadowgraphy and X-ray imaging for void fraction determination	11
1.6.3 Chapter 4: Void fraction measurements in partial cavitation regimes by X-ray computed tomography	11
1.6.4 Chapter 5: Conclusions and Perspectives	12
References	12
2 Dynamics of partial cavitation in an axisymmetric converging-diverging nozzle	15
2.1 Introduction	16
2.2 Experimental details	18
2.2.1 Flow facility	18
2.2.2 Experimental procedure	19
2.2.3 Shadowgraphy	20
2.3 Data processing	21
2.3.1 Image processing	21
2.3.2 X-t diagrams	23
2.4 Results	24
2.4.1 Pressure loss and cavity length	24
2.4.2 Shedding frequency and temporal development of cavity cloud	26
2.4.3 Re-entrant jet mechanism and bubbly shock mechanism	28
2.5 Discussion	33
2.6 Conclusions and Outlook	35
References	37

3	Direct comparison of shadowgraphy and X-ray imaging for void fraction determination	41
3.1	Introduction	42
3.2	Methodology	43
3.2.1	Setup.	43
3.2.2	Quality of the imaging modalities	45
3.2.3	Data processing	46
3.3	Results	48
3.4	Discussion	51
3.5	Conclusions.	55
	References	55
4	Void fraction measurements in partial cavitation regimes by X-ray computed tomography	59
4.1	Introduction	60
4.2	Experimental details	62
4.2.1	Flow facility	62
4.2.2	Experimental procedure	63
4.2.3	X-ray imaging	63
4.3	Data processing	65
4.3.1	Image processing	65
4.3.2	Computed tomography	67
4.4	Results	70
4.4.1	Pressure loss coefficient	70
4.4.2	CT void fraction calibration	71
4.4.3	Cross-sectional distribution of void fraction	74
4.5	Conclusions and Outlook	81
	References	81
5	Conclusions and perspectives	85
5.1	Conclusions.	86
5.2	Perspectives on future research	87
	References	89
	Acknowledgements	92
	Curriculum Vitæ	93
	List of Publications	95

SUMMARY

Cavitation is a well-known phenomenon, occurring in a wide range of applications. In most applications, cavitation is undesirable, such as turbines, pumps, ship propellers and diesel injector nozzles. Cavitation can cause material erosion, flow blockage, noise and degradation of equipment over time. The ability to predict the behavior of this type of flow will be beneficial to a wide range of systems. One complex form of cavitation is the periodic shedding of cavitation clouds. This thesis experimentally describes the mechanisms which are responsible for the periodic shedding of vapor clouds. A converging-diverging nozzle (venturi) is selected as a canonical geometry for this project. The venturi has the highest contraction ratio, due to its shape, which results in a broader dynamic cavitation range. The venturi gives us the ability to precisely differentiate between different cavitation mechanisms due to their more intense nature.

First of all, in order to understand the flow field in the venturi, particle image velocimetry (PIV) is performed on the non-cavitating flow. The measurements are conducted in a closed flow loop. In the converging section, the mean velocity field along the axis of the venturi increases, as expected. At the throat, the radial variation of velocity reveals distinct peaks close to the venturi wall. In the diverging section, the velocity decreases and a jet is formed in the center of the diffuser. It follows from potential flow theory and PIV results that cavitation would initiate near the wall of the throat.

The partial cavitation regimes are examined using a high-speed shadowgraphy experiment. These regimes are generated by changing the global static pressure and flow velocity independently. Using a space-time diagram, we show that for cavitation number $\sigma > 0.95$ the cavity shedding is caused by the re-entrant jet mechanism, and for $\sigma < 0.75$ the mechanism responsible for periodic cavity shedding is the bubbly shock mechanism. Both mechanisms are observed in the transition region, $0.75 < \sigma < 0.95$.

The re-entrant jet mechanism is a pressure gradient driven phenomenon, which is caused by a temporary stagnation point at the cavity front. This leads to stick-slip behavior of the cavity. In the bubbly shock regime, a shock wave is induced by a collapse of the previously shed vapor bubbles downstream of the venturi, which triggers the initiation of the detachment of the growing cavity. The propagation velocity of the shock wave is quantified both in the liquid and the mixture phase.

The second part of this thesis presents a quantitative comparison of shadowgraphy and X-ray imaging to demonstrate the need for X-ray imaging. The need for this study arises from the fact that shadowgraphs are sometimes utilized to quantify void fraction profiles, which is an unproven method. Time-averaged X-ray images are used to evaluate the performance of the time-averaged shadowgraphs. The cavitating flow through the venturi is considered, for three separate cavitation numbers. The complex nature of the cavitating flow through the venturi manifests itself in the occurrence of three distinct regimes: a swarm of tiny bubbles; a large, coalesced cavity near the wall; and a drifting/collapsing cavity. The flow regime governs the performance of shadowgraphy for

void fraction determination, with two of the three regimes deemed acceptable for shadowgraphy. The quantitative comparison exemplifies that sole reliance on shadowgraphy may lead one to draw improper conclusions on the void fraction distributions, even at a qualitative level.

Finally, X-ray computed tomography (CT) is used to measure the void fractions in partial cavitation regimes. 3D reconstruction of the X-ray images is used to differentiate between vapor and liquid phase. The void fraction downstream of the venturi in the bubbly shock mechanism is found to be more than twice compared to the re-entrant jet mechanism. The results show the presence of intense cavitation at the walls of the venturi. Moreover, the vapor phase mixes with the liquid phase downstream of the venturi, resulting in cloud-like cavitation.

The results in this thesis show that the combination of high-speed shadowgraphy and X-ray CT are suitable methods to study partial cavitation regimes. The data gives a novel insight into this complex multiphase flow phenomenon. Nevertheless, the application of these experimental techniques is expected to be limited to the lab experiments only, as it is unrealistic to perform these types of investigations to the great variety of practical applications. Based on the results in this thesis, various perspectives are provided for new and improved studies that can be used to investigate real-life practical cavitating flows effectively.

SAMENVATTING

Cavitatie is een welbekend fenomeen, dat voorkomt in tal van toepassingen. In de meeste toepassingen is cavitatie ongewenst, te denken valt aan turbines, pompen, scheepsschroeven en in diesilverstuivers. Cavitatie kan materiaal-erosie, stromingsweerstand, lawaaioverlast en op termijn schade aan onderdelen veroorzaken. De mogelijkheid om het gedrag van dit type stroming te voorspellen zal voordelig zijn voor tal van systemen. Eén complexe vorm van cavitatie is het periodieke afschudden van cavitatie bellen. Deze thesis beschrijft de mechanismen die verantwoordelijk zijn voor het periodiek afschudden van dampbellen, door middel van experimenten. Een convergerend-divergerend geometrie (venturi) is geselecteerd als basisgeometrie voor deze thesis. Door de specifieke vorm heeft de venturi de grootste contractieverhouding, wat resulteert in een groter dynamisch cavitatie bereik. De venturi geeft ons de mogelijkheid om de verschillende cavitatie mechanismen precies te onderscheiden, door hun meer intensieve natuur.

In de eerste plaats is particle image velocimetry (PIV) toegepast op een niet-caviterende stroming, om het stromingsveld in de venturi te begrijpen. De metingen zijn uitgevoerd in een gesloten flowloop. In het convergerende deel neemt de gemiddelde snelheid (d.w.z. langs de as van de venturi) toe, zoals verwacht. Op de keeldoorsnede, dichtbij de wand van de venturi, laat de variatie in de radiale snelheid onderscheiden pieken zien. In het divergerende deel neemt de snelheid af en wordt er een waterstraal gevormd in het midden van de diffusor. Van potentiaalstromingstheorie en PIV volgt dat de cavitatiebellen het eerst bij de wand van de keel gevormd worden.

De partiële cavitatie regimes zijn onderzocht met een hogesnelheidsvisualisatie. Deze regimes zijn gemaakt door de globale statische druk en de stroomsnelheid onafhankelijk van elkaar te variëren. Door gebruik te maken van een ruimtetijd diagram, laten we zien dat voor cavitatie getallen $\sigma > 0.95$ het afschudden van cavitatiebellen veroorzaakt wordt door het 're-entrant jet' mechanisme. Voor $\sigma < 0.75$ is het verantwoordelijke mechanisme voor het periodiek afschudden het 'bubbly shock' mechanisme. Beide mechanismen zijn geobserveerd in het transitie gebied, $0.75 < \sigma < 0.95$.

Het re-entrant jet mechanisme is een fenomeen dat gedreven wordt door een drukgradiënt, die veroorzaakt wordt door een tijdelijk stagnatiepunt aan de voorkant van de caviteit. Dit leidt tot stick-slip gedrag van de caviteit. In het bubbly shock gebied wordt een schokgolf gecreëerd door een implosie van de voorgaande afgeschudde dampbel, stroomafwaarts ten opzichte van de venturi. Dit is een trigger voor de initiatie van de loslating van de aangroeiende caviteit. De voortplantingssnelheid van de schokgolf is gekwantificeerd in zowel de vloeistof als in de gemengde fase.

Het tweede deel van deze thesis presenteert een kwantitatieve vergelijking van 'shadowgraphy' en 'X-ray imaging' (röntgenopnames) om de noodzaak van X-ray imaging te laten zien. De noodzaak van deze studie komt van het feit dat shadowgraphy soms gebruikt worden om de gasfractie profielen te kwantificeren, hoewel dit niet een bewezen methode is. Tijds-gemiddelde X-ray afbeeldingen zijn gebruikt om de resultaten

van de tijd-gemiddelde shadowgraphy te evalueren. De caverende stroming door de venturi is beschouwd voor drie afzonderlijke cavitatie getallen. De complexe natuur van de caverende stroming door de venturi openbaart zichzelf in drie onderscheiden regimes: een zwerm kleine bellen; een grote, samengestelde bel dichtbij de wand; en een bewegende/imploderende caviteit. Het flowregime bepaalt de prestatie van shadowgraphy voor het bepalen van de gasfractie. Voor twee van de drie regimes shadowgraphy is aanvaardbaar. De kwantitatieve vergelijking laat zien dat afhankelijkheid van alleen shadowgraphy kan leiden tot onjuiste conclusies voor de gasfractie verdeling, zelfs op het kwalitatieve niveau.

Tenslotte is X-ray computed tomography (CT) gebruikt om de gasfracties in partiële cavitatie regimes te meten. 3D reconstructie van X-ray afbeeldingen is toegepast om de gas en vloeistof fase van elkaar te onderscheiden. De gasfractie in het bubbly shock mechanisme is meer dan twee keer zo hoog vergeleken bij het re-entrant jet mechanisme. De resultaten laten de aanwezigheid van intense cavitatie aan de wand van de venturi zien. Stroomafwaarts van de venturi mixt de dampfase met de vloeistoffase wat resulteert in wolkachtige cavitatie.

De resultaten in deze thesis laten zien dat de combinatie van hogesnelheid shadowgraphy en X-ray CT een geschikte methode is om partiële cavitatie regimes te bestuderen. De data geeft nieuwe inzichten in dit complexe meerfasen-stromings fenomeen. Desondanks is de verwachting dat de toepassing van deze experimentele technieken gelimiteerd wordt tot alleen laboratoriumexperimenten. Dit omdat het onrealistisch is om deze vormen van onderzoek toe te passen tot een grote verscheidenheid van praktische toepassingen. Gebaseerd op de resultaten in deze thesis, worden er verschillende perspectieven aangereikt voor nieuw en beter onderzoek. Deze perspectieven kunnen gebruikt worden om praktische caverende stromingen effectief te onderzoeken.

1

INTRODUCTION

1.1. CAVITATION

The process of rupturing a liquid to vapor by a decrease in pressure at roughly constant liquid temperature is generally called cavitation (Brennen, 2013). Depending on the flow configuration and the physical properties of the liquid, it can present various features (Franc and Michel, 2006). In engineering, cavitation is identified as the vapor pockets created by a blend of low pressure and high-speed flows. The difference between cavitation and boiling is that the cavitation arises due to a decrease in pressure, while boiling occurs due to an increase in temperature. As soon as the cavitation bubble reaches a high-pressure region, it collapses. Cavitation has been a subject of research since the late 19th century. In 1873, Reynolds was among the initial few scientists who attempted to explain this phenomenon in ship propellers (Reynolds, 1873).

The initiation of vapor formation is a complex phenomenon. The water molecules in pure water can sustain lower pressures than vapor pressure due to the cohesive forces. Therefore, cavitation is generally initiated by cavitation nuclei. The cavitation nuclei may be free gas bubbles in the bulk of water, or interfacial gaseous voids located on the surface of particles in the water, or on bounding walls (Mørch, 2015). Many studies have shown that impurities in the water can significantly change the stochastic behavior of its cavitation compared to the behavior in pure water (Caupin et al., 2012; Caupin and Herbert, 2006; Fisher, 1948; Herbert et al., 2006). The cavitation nuclei, usually together with the roughness, contribute to the inception of cavitation. The vapor and gas-filled bubbles grow rapidly as a result of hydrodynamic forces. Detailed information regarding cavitation inception mechanisms can be found in a review paper by Rood (1991).

Cavitation can be classified as:

- **bubble cavitation:** a cavitation bubble develops in a low-pressure region due to a rapid increase of existing cavitation nuclei in the liquid. These bubbles move with the flow and as soon as the liquid reaches a high-pressure zone, they collapse.
- **sheet cavitation:** a large, stable zone containing vapor resides around at the same location corresponding to the profile of the test section.
- **partial cavitation:** also known as periodic cavitation, a vapor cloud is formed and shed as the sheet cavity periodically oscillates. An example of partial cavitation inside a converging-diverging nozzle is presented in Fig. 1.1.
- **vortex cavitation:** the rotational motion of the fluid in a vortex creates a low-pressure region in the core of the vortex, hence inducing a cavitating vortex.
- **supercavitation:** the sheet cavity elongates considerably and covers the entire solid body in vapor (Franc and Michel, 2006).

In practical applications, the presence of cavitation in hydraulic systems, which are designed for homogeneous flows, is viewed as a nuisance due to several reasons. The cavitation bubbles or clouds violently collapse as soon as they reach a high-pressure

region. These collapses cause pressure fluctuations in the flow, sometimes resulting in shock waves.

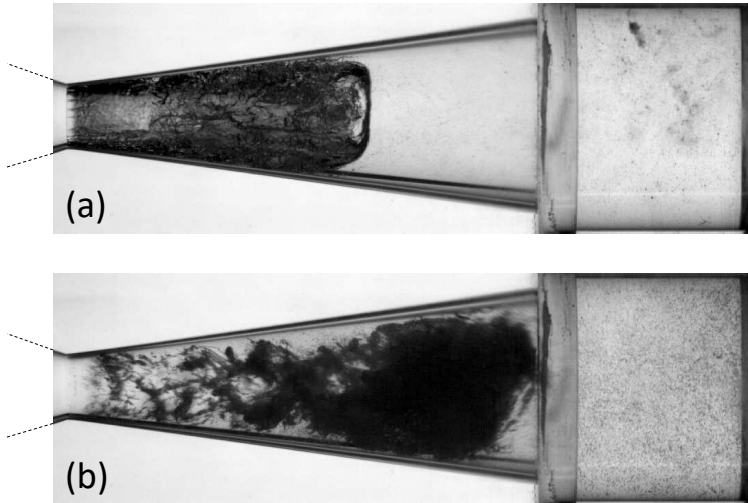


Figure 1.1: Example of partial cavitation in a converging-diverging nozzle. Flow is from left to right. (a) A growing cavity can be seen. (b) The cavity detaches. Obtained from the experiment described in chapter 2. The cavitation number is $\sigma = 0.40$.

The following are the main disadvantages of cavitation:

- a reduction in performance of hydraulic systems (flow blockage and increase in drag);
- noise production and system vibrations;
- erosion leading to failure fatigue.

Cavitation induced erosion is one of the most researched topics in this field, as it has a severe impact on materials and equipment over time. The first comprehensive theoretical study on the collapse of an empty cavity at a rigid wall was reported by Plesset and Chapman (1971). These theoretical results were experimentally validated by Lauterborn and Bolle (1975). Dular et al. (2013) showed the time evolution of the erosion pit shape on an aluminum foil. The authors showed that the foil is deformed multiple times before a hole is eventually punctured. It was also concluded that larger single pits were created from several impacts of shock waves on the same area. A detailed review of the physical mechanisms responsible for cavitation erosion can be found in a paper by Van Terwisga et al. (2009). In Fig. 1.2, an example of erosion caused by cavitation on the blade of a boat propeller can be seen. Erosion caused by cavitation was witnessed in many other devices like diesel injector nozzles (Gavaises et al., 2007), gear pumps (Hunt et al., 1981), and bearings (Cole and Hughes, 1956).

In some instances, cavitation can have benefits. Cavitation helps in the mixing of fuel and air in marine diesel engines (Habchi et al., 2014). Cavitating jets are also used to clean



Figure 1.2: Example of blade damage caused by cavitation erosion on a boat propeller (this photograph has been obtained from the Britannica website, where it was made available by Erik Ax Dahl).

surfaces. Moreover, it can also be utilized for ultrasonic drug delivery (Ibsen et al., 2013). While significant research has been performed in developing ways to avoid cavitation, there have been relatively few investigations in the cause of this complex phenomenon. Hence, correct knowledge of the cavitation physics is essential, so that its negative aspects can be mitigated or reduced in a controlled way.

1.2. CAFE PROJECT

This research was performed with the Marie Curie Horizon 2020 ITN program ‘CaFE’. The primary aim of this program was to provide new state-of-the-art experimental data and an open-source simulation tool for the investigation of cavitation and cavitation induced erosion. Sixteen Ph.D. students were hired in the consortium, and they were divided among four work packages. Three out of sixteen Ph.D. students (work package 2) performed the experimental research and provided a high-quality dataset for the validation of numerical studies. The rest of the Ph.D. students numerically investigated cavitating flows. This Ph.D. project consists of the experimental work within work package 2. In the CaFE project, frequent progress meetings took place between the partners. The project also provided the opportunity to spend two months on numerically validating the experimental results at City University London under the supervision of Prof. Manolis Gavaises. Moreover, an experimental campaign was conducted in a channel to investigate cavitation erosion at the Hydraulic Laboratory of ANDRITZ HYDRO in Vevey under the supervision of Dr. Magdalena Neuhauser.

1.3. PARTIAL CAVITATION

Partial cavitation is one of the most interesting and complex types of cavitation. Partial cavities generally undergo self-sustaining oscillations in cavity length, which results in the shedding of vapor clouds. Shedding of vapor clouds and their violent collapses are principal agents of erosion induced by cavitation.

Classically, the re-entrant jet mechanism was considered to be the only responsible mechanism for the cloud shedding. The re-entrant jet mechanism is attributed to the presence of a re-entrant flow at the closure of the cavity, which moves upstream. As the minimum pressure transpires in the cavity, the curvature of the surrounding streamlines tends to be directed towards the cavity, which can be seen in Fig. 1.3 (Callenaere et al., 2001). Clock-wise oriented vorticity is generated in the closure region. After shedding of the cavity, this vortical flow region is convected downstream by the free stream velocity minus the velocity induced by the vorticity. Many researchers investigated the conditions necessary for the evolution of a re-entrant jet and succeeding cloud shedding (e.g., Bensch (2011); Kawanami et al. (1997); Knapp (1955)).

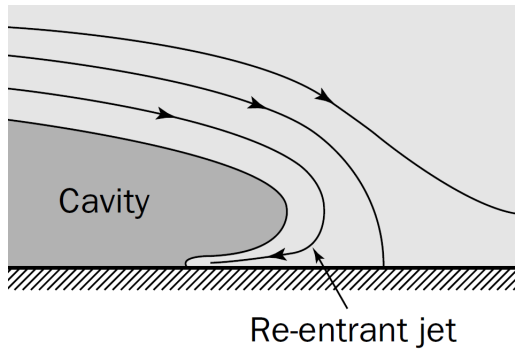


Figure 1.3: Schematic illustration of the re-entrant jet in the closure region of an attached cavity (from: Callenaere et al. (2001)).

The condensation shocks from the previously shed vapor clouds were investigated by several researchers (e.g., Jakobsen (1964); Reisman et al. (1998)). However, Ganesh (2015) recently demonstrated that the ‘bubbly shock mechanism’ can cause the shedding of vapor clouds. The authors used X-ray densitometry to investigate void fractions in the cavity. The presence of relatively high void fraction at the closure of the cavity was attributed to the bubbly shock mechanism. Bhatt and Mahesh (2020) and Budich et al. (2018) numerically investigated these experiments and found that the bubbly shock mechanism is initiated by the impingement of the collapse-induced pressure waves from the previously shed cloud.

1.4. SELECTION OF GEOMETRY

The first goal of this study was to obtain measurements of high quality to investigate partial cavitation regimes and to investigate their characteristics. Hydrodynamic cavitation is usually generated by passing a liquid through a contracted channel or past a propeller,

but the later one is a much more complex geometry. The flow velocity in the constriction increases, which results in a decrease in pressure, and high energy cavitation bubbles are generated. In literature, hydrofoils (Fig. 1.4(a)) and two-dimensional wedges (Fig. 1.4(b)) are the most frequently used test-geometries to investigate partial cavitation regimes. Periodic cloud shedding can be observed in both geometries, but due to their shape, it is not possible to distinguish quantitatively between the re-entrant jet and the bubbly shock mechanism. The main reason is that the range in which partial cavitation occurs is quite small, and the cavitation switches to supercavitation as soon as the cavitation intensity increases, as discussed below. Hence, the physical characteristics of the partial cavitation mechanisms can not be investigated.

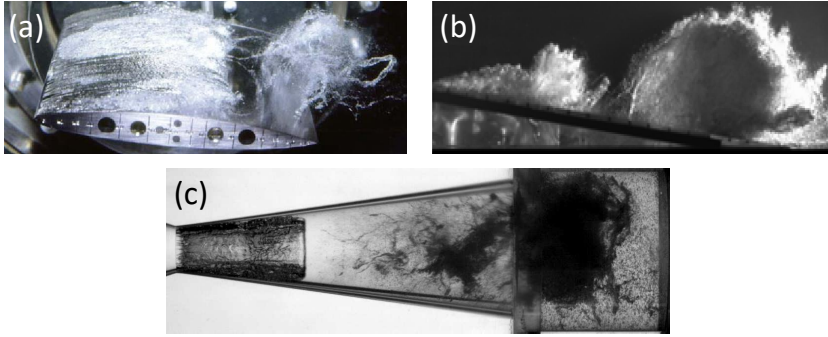


Figure 1.4: Typical examples of partial cavitation in three different geometries: (a) NACA 16012 hydrofoil at $\sigma \approx 0.60$ (from: Franc and Michel (2006)), (b) two-dimensional wedge at $\sigma = 1.95$ (from: Ganesh et al. (2016)) and (c) converging-diverging nozzle at $\sigma = 0.40$ (obtained from the experiment described in chapter 2). Flow is from left to right in all three snapshots.

An important parameter for classification of cavitating flows is the cavitation number (σ):

$$\sigma = \frac{p - p_v}{\frac{1}{2}\rho u_0^2}, \quad (1.1)$$

where p is the reference pressure, p_v the vapor pressure at the reference temperature, ρ the density of the fluid, and u_0 the free stream velocity. Franc and Michel (2006) used a two-dimensional hydrofoil to produce various cavitation patterns (see Fig. 1.5). The results are displayed in a map depicting the various cavitation patterns as a function of the angle of attack α and the cavitation number σ . l is the cavity length, and e is the maximum thickness of the cavity. On this map, the area of partial cavitation on the flat upper side of the foil extends between cavitation inception, limited by a cavity length l equal to zero. The supercavitation corresponds to a cavity length l equal to the chord length c . In the case of an unsteady cavity, l stands for the maximum length of the cavity (Franc and Michel, 2006). In Fig. 1.5, it can be seen that at specific conditions, the cavity is shorter in length in comparison with the chord length, and it is notably stable. The authors state that for the small values of σ and α , the partial cavities are smaller in length and thinner, and they refer them as the re-entrant jet dominant regimes. In the upper side of the map, for large values of σ and α , the cavities become thicker and more unstable.

However, it is not stated what causes the periodic shedding in this regime. One of the hypotheses from this regime (also explained in chapter 2) is that it is governed by the bubbly shock regime.

As mentioned above, the range of cavitation numbers for which a hydrofoil geometry produces partial cavitation regimes is very small. Therefore, a converging-diverging nozzle (venturi) was selected for this project (see Fig. 1.4(c)). The venturi has the highest contraction ratio compared to the hydrofoil and wedge, due to its shape, which results in a broader dynamic cavitation range. The venturi gives us the ability to clearly distinguish between different cavitation mechanisms due to their more intense nature.

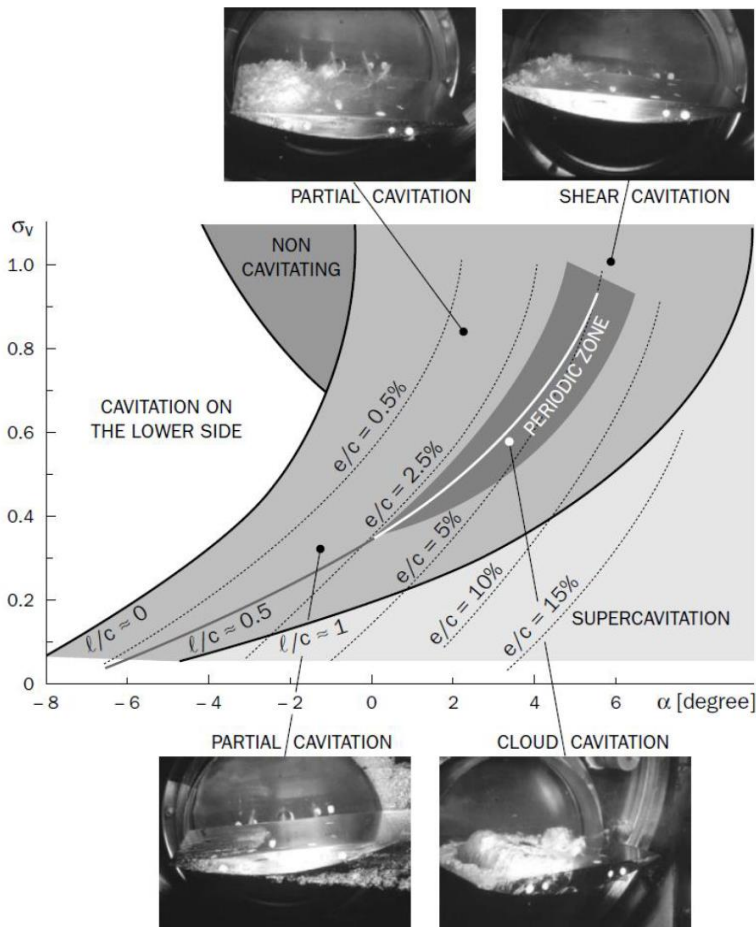


Figure 1.5: Cavitation patterns on a two-dimensional hydrofoil at free stream velocity of 10 m/s (from: Franc and Michel (2006)). l is the cavity length, e is the maximum thickness of the cavity, α is the angle of attack, σ_v is the cavitation number, and c is the chord length. The region of periodic oscillations is indicated by the shaded area.

1.5. FLOW CHARACTERISTICS IN VENTURI

Fig. 1.6 schematically shows the pressure and velocity profiles at the centerline along the throat (assuming uniform profiles). A photograph of the venturi can be seen in Fig. 1.6(a). Note that the throat has a sharp edge. Fig. 1.6(b) represents the superficial velocity profile (solid blue line) based on mass conservation and assuming uniform velocity. Fig. 1.6(c) shows the corresponding pressure profile (solid blue line) estimated using the 1D Euler equation. For the cases with flow separation and/or a significant cavity, we can no longer predict the pressure using this method due to the flow blockage caused by cavitation (explained in more detail in Section 2.4.1). However, using the shape of the geometry, we can predict it qualitatively: for a very low σ , we have a very large cavity which extends the effective throat diameter and leads to a larger high-velocity region. For low σ , the pressure recovery is thus delayed and not complete, as shown by dashed lines (Fig. 1.6).

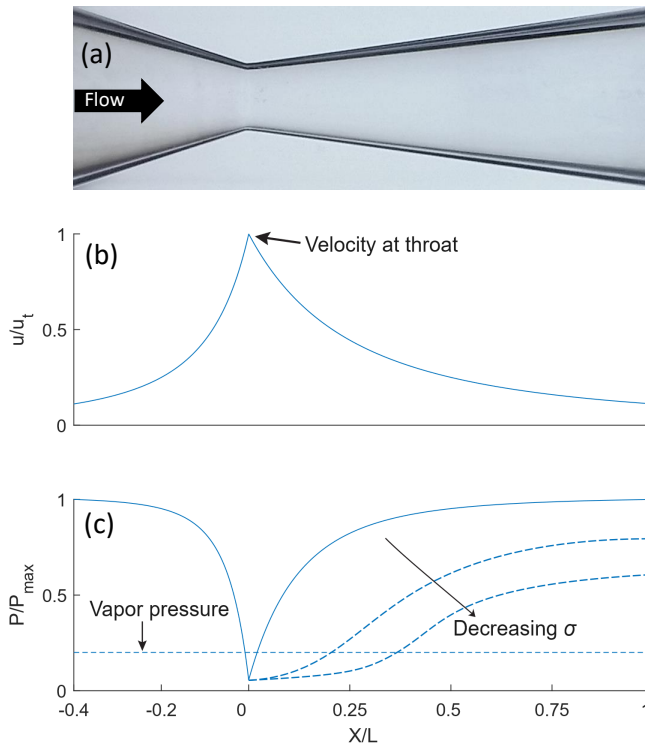


Figure 1.6: Schematic representation of the dimensionless velocity and pressure profiles along the length of the venturi (reproduced from chapter 2). The velocity is normalized with the maximum velocity at the throat and pressure with the maximum upstream pressure. Flow is from left to right.

In order to understand the flow field in the venturi, particle image velocimetry (PIV) was performed on the non-cavitating flow. A Reynolds number of 60×10^3 was selected, as this is the highest Reynolds number before the initiation of cavitation in this venturi. The Reynolds number is here based on the venturi throat diameter. PIV was adopted

because this returns valuable velocity information in the converging-diverging section. The measurements were conducted in a closed loop system. The detailed experimental setup is described in chapter 2 and the details on PIV measurements are given in a paper by John et al. (2020) (the same venturi was used for both experiments). The flow was seeded with hollow glass particles. These particles had a mean diameter of $12\ \mu\text{m}$ and a density of $1.1 \pm 0.5\ \text{g/cm}^3$ (Sphericell 110P8, Potter Industries). The field of view (FOV) was illuminated using a laser sheet with approximately 1 mm thickness entering from the top in the x-y plane. A typical particle image with the vector field is shown in Fig. 1.7.

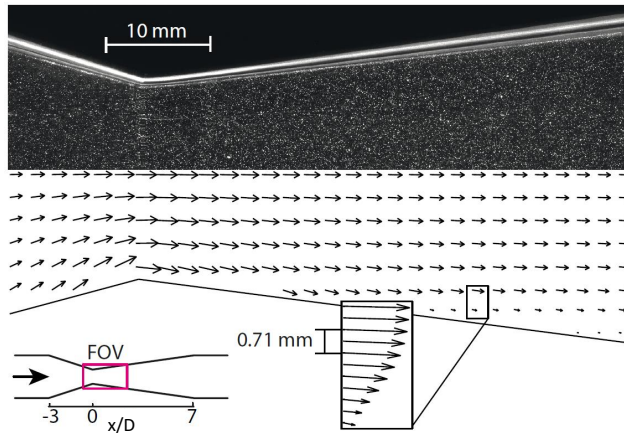


Figure 1.7: (Top) typical particle image of the PIV acquisition. (Bottom) the resulting time-averaged vector field at the center plane. Every fifth vector is shown. The inset shows the boundary layer with the actual resolution (from: John et al. (2020)).

The time-averaged velocity field for the Reynolds number of 60×10^3 is shown in Fig. 1.8. The FOV was selected at the throat region as this is the location where cavitation initiates. x/D represents the axial locations, where D represents the throat diameter ($D = 16.67\ \text{mm}$). First, we examine the converging section of the venturi. It is a positively strained region; the mean velocity along the axis of the venturi increases, as expected. The mean velocity along the axis of the venturi has a visible peak at the throat. At $x/D = 0$, the mean velocity is at a maximum, in particular, close to the venturi wall. The velocity vectors converge at the walls of the throat as shown in the bottom half of Fig. 1.7. An adverse pressure gradient can be seen at the venturi throat. In the diverging section, the velocity decreases. The flow in the diverging section is complex due to a velocity gradient and flow separation in the wall-normal direction at approximately $x/D = 1.4$. A jet forms in the center of the diffuser which causes this velocity gradient. The mean velocity profile is very flat in the core region except near the wall and it resembles a plug flow profile. As we go further downstream of the venturi ($x/D = 2.8$), the velocity in the core decreases, but the jet is not disturbed.

It follows from potential flow theory and PIV results that cavitation would initiate near the wall of the throat. This is further verified from the shadowgraphy results in chapter 2 and the X-ray results in chapter 4.

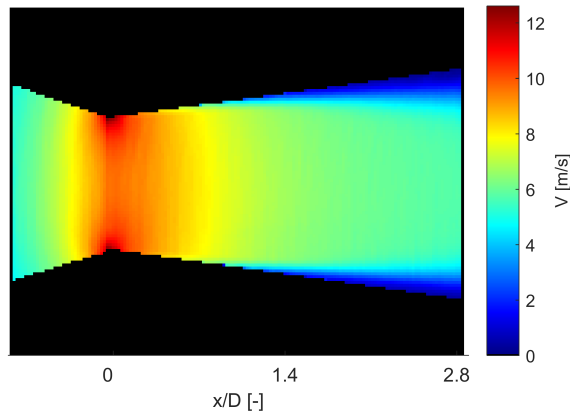


Figure 1.8: Time-averaged velocity field in midplane of the venturi. Flow is from left to right. The Reynolds number is 60×10^3 based on the venturi throat diameter.

1.6. RESEARCH STRUCTURE

The starting point of this study is the investigation of partial cavitation regimes performed by Ganesh et al. (2016) on a two-dimensional wedge. Physical mechanisms responsible for partial cavitation regimes were described. However, little quantitative information was available at the time regarding the dependence of partial cavitation regimes on the cavitation number. The main aim of this research is to present experimental proof for mechanisms responsible for the partial cavitation regimes. The experimental validation tasks are formed as follows:

1. Develop a method based on high-speed visualization to differentiate between the re-entrant jet mechanism and the bubbly shock mechanism (chapter 2)
2. Experimentally show that the governing parameter, which determines either of these mechanisms, is the cavitation number (chapter 2)
3. Quantitative comparison of shadowgraphy and X-ray imaging to demonstrate the need for X-ray imaging (chapter 3)
4. Experimentally reconstruct the three-dimensional flow structures using X-ray computed tomography to obtain radial geometric features of the cavitating flow (chapter 4)
5. Quantification of the void fractions in these regimes using X-ray computed tomography (chapter 4)

Three main experiments were performed to achieve these goals. The results of these experiments were published in three journal articles represented by three chapters in this

thesis. Below, we give brief overview of the topics covered in different chapters of this thesis.

1.6.1. CHAPTER 2: DYNAMICS OF PARTIAL CAVITATION IN AN AXISYMMETRIC CONVERGING-DIVERGING NOZZLE

Partial cavitation regimes in the venturi are investigated using shadowgraphy. These regimes are generated by changing the global static pressure and flow velocity independently. The dynamics are investigated using a space-time diagram. Using such a diagram we show that for cavitation number $\sigma > 0.95$ the cavity shedding is caused by the re-entrant jet mechanism, and for $\sigma < 0.75$ the mechanism responsible for periodic cavity shedding is the bubbly shock mechanism. Both mechanisms are observed in the transition region, $0.75 < \sigma < 0.95$. The shedding frequencies, expressed as Strouhal numbers, collapse on a single curve when plotted against the cavitation number, except for the transition region. The re-entrant jet mechanism is a pressure gradient driven phenomenon, which is caused by a temporary stagnation point at the cavity front. This leads to stick-slip behavior of the cavity. In the bubbly shock regime, a shock wave is induced by a collapse of the previously shed vapor bubbles downstream of the venturi, which triggers the initiation of the detachment of the growing cavity. The propagation velocity of the shock wave is quantified both in the liquid and the mixture phase by means of a space-time diagram.

1.6.2. CHAPTER 3: DIRECT COMPARISON OF SHADOWGRAPHY AND X-RAY IMAGING FOR VOID FRACTION DETERMINATION

A quantitative analysis of two imaging modalities, shadowgraphy and X-ray imaging, is presented in the framework of void fraction determination. The need for this arises from the fact that shadowgraphs are sometimes utilized to quantify void fraction profiles, which is an unproven method. Time-averaged X-ray images are used to evaluate the performance of the time-averaged shadowgraphs. A cavitating flow through the venturi is considered, for three separate cavitation numbers. The complex nature of the cavitating flow through the venturi manifests itself in the occurrence of three distinct regimes: a swarm of tiny bubbles; a large, coalesced cavity near the wall; and a drifting/collapsing cavity. The flow regime governs the performance of shadowgraphy for void fraction determination, with two of the three regimes deemed acceptable for shadowgraphy. The quantitative comparison exemplifies that sole reliance on shadowgraphy may lead one to draw improper conclusions on the void fraction distributions, even at a qualitative level.

1.6.3. CHAPTER 4: VOID FRACTION MEASUREMENTS IN PARTIAL CAVITATION REGIMES BY X-RAY COMPUTED TOMOGRAPHY

We use X-ray computed tomography to obtain the time-averaged void fraction distribution in the venturi. Using this technique, the partial cavitation mechanisms are examined. 3D reconstruction of the X-ray images is used (i) to differentiate between vapor and liquid phase, (ii) to obtain radial geometric features of the flow, and (iii) to quantify the local void fraction. The void fraction downstream of the venturi in the bubbly shock mechanism is found to be more than twice compared to the re-entrant jet mechanism. The results show the presence of intense cavitation at the walls of the venturi. Moreover, the vapor phase

mixes with the liquid phase downstream of the venturi, resulting in cloud-like cavitation.

1.6.4. CHAPTER 5: CONCLUSIONS AND PERSPECTIVES

Finally, in chapter 5, we present a summary of the conclusions presented in this thesis. We give the concluding remarks, as well as perspectives for future work. Furthermore, we briefly report the remaining open questions.

REFERENCES

- Bensow, R. E. (2011). Simulation of the unsteady cavitation on the Delft Twist11 foil using RANS, DES and LES. In *Proceedings of the 2nd International Symposium on Marine Propulsors, Hamburg, Germany*.
- Bhatt, M. and Mahesh, K. (2020). Numerical investigation of partial cavitation regimes over a wedge using Large Eddy Simulation. *International Journal of Multiphase Flow*, 122:103155.
- Brennen, C. E. (2013). *Cavitation and bubble dynamics*. Cambridge University Press.
- Budich, B., Schmidt, S., and Adams, N. (2018). Numerical simulation and analysis of condensation shocks in cavitating flow. *Journal of Fluid Mechanics*, 838:759–813.
- Callenaere, M., Franc, J.-P., Michel, J.-M., and Riondet, M. (2001). The cavitation instability induced by the development of a re-entrant jet. *Journal of Fluid Mechanics*, 444:223–256.
- Caupin, F., Arvengas, A., Davitt, K., Azouzi, M. E. M., Shmulovich, K. I., Ramboz, C., Sessoms, D. A., and Stroock, A. D. (2012). Exploring water and other liquids at negative pressure. *Journal of Physics: Condensed Matter*, 24(28):284110.
- Caupin, F. and Herbert, E. (2006). Cavitation in water: a review. *Comptes Rendus Physique*, 7(9):1000 – 1017.
- Cole, J. and Hughes, C. (1956). Oil flow and film extent in complete journal bearings. *Proceedings of the Institution of Mechanical Engineers*, 170(1):499–510.
- Dular, M., Delgosha, O. C., and Petkovšek, M. (2013). Observations of cavitation erosion pit formation. *Ultrasonics Sonochemistry*, 20(4):1113 – 1120.
- Fisher, J. C. (1948). The fracture of liquids. *Journal of applied Physics*, 19(11):1062–1067.
- Franc, J.-P. and Michel, J.-M. (2006). *Fundamentals of cavitation*, volume 76. Springer Science & Business Media.
- Ganesh, H. (2015). Bubbly Shock Propagation as a Cause of Sheet to Cloud Transition of Partial Cavitation and Stationary Cavitation Bubbles Forming on a Delta Wing Vortex. PhD thesis, The University of Michigan.

- Ganesh, H., Mäkiharju, S. A., and Ceccio, S. L. (2016). Bubbly shock propagation as a mechanism for sheet-to-cloud transition of partial cavities. *Journal of Fluid Mechanics*, 802:37–78.
- Gavaises, M., Papoulias, D., Andriotis, A., Giannadakis, E., and Theodorakakos, A. (2007). Link between cavitation development and erosion damage in diesel injector nozzles. Technical report, SAE Technical Paper.
- Habchi, C., Gillet, N., Velghe, A., Bohbot, J., Schmid, A., Von Rotz, B., and Herrmann, K. (2014). On the role of cavitation in marine large diesel injector: numerical investigation of nozzle orifices eccentricity. In *Annual Conference on Liquid Atomization and Spray Systems, Bremen, Germany*.
- Herbert, E., Balibar, S., and Caupin, F. (2006). Cavitation pressure in water. *Phys. Rev. E*, 74:041603.
- Hunt, J., Ryde-Weller, A., and Ashmead, F. (1981). Cavitation between meshing gear teeth. *Wear*, 71(1):65 – 78.
- Ibsen, S., Schutt, C. E., and Esener, S. (2013). Microbubble-mediated ultrasound therapy: a review of its potential in cancer treatment. *Drug design, development and therapy*, 7:375.
- Jakobsen, J. (1964). On the Mechanism of Head Breakdown in Cavitating Inducers. *Journal of Basic Engineering*, 86(2):291–305.
- John, K., Jahangir, S., Gawandalkar, U., Hogendoorn, W., Poelma, C., Grundmann, S., and Bruschi, M. (2020). Magnetic resonance velocimetry in high-speed turbulent flows: sources of measurement errors and a new approach for higher accuracy. *Experiments in Fluids*, 61(2):27.
- Kawanami, Y., Kato, H., Yamaguchi, H., Tanimura, M., and Tagaya, Y. (1997). Mechanism and control of cloud cavitation. *Journal of Fluids Engineering*, 119(4):788–794.
- Knapp, R. T. (1955). Recent investigations of the mechanics of cavitation and cavitation damage. *Transactions of the ASME*, 77:1045–1054.
- Lauterborn, W. and Bolle, H. (1975). Experimental investigations of cavitation-bubble collapse in the neighbourhood of a solid boundary. *Journal of Fluid Mechanics*, 72(2):391–399.
- Mørch, K. A. (2015). Cavitation inception from bubble nuclei. *Interface Focus*, 5(5):20150006.
- Plesset, M. S. and Chapman, R. B. (1971). Collapse of an initially spherical vapour cavity in the neighbourhood of a solid boundary. *Journal of Fluid Mechanics*, 47(2):283–290.
- Reisman, G., Wang, Y.-C., and Brennen, C. E. (1998). Observations of shock waves in cloud cavitation. *Journal of Fluid Mechanics*, 355:255–283.

- Reynolds, O. (1873). The causes of the racing of the engines of screw steamers investigated theoretically and by experiment. *Trans. Inst. Naval Arch*, 14:56–67.
- Rood, E. P. (1991). Review-Mechanisms of Cavitation Inception. *Journal of Fluids Engineering*, 113(2):163–175.
- Van Terwisga, T., Fitzsimmons, P., Li, Z.-r., and Foeth, E. J. (2009). Cavitation erosion-a review of physical mechanisms and erosion risk models. *Proc. 7th Int. Sym. Cavitation, CAV2009, Ann Arbor, MI*.

2

DYNAMICS OF PARTIAL CAVITATION IN AN AXISYMMETRIC CONVERGING-DIVERGING NOZZLE

This chapter is based on: S. Jahangir, W. Hogendoorn, C. Poelma, *Dynamics of partial cavitation in an axisymmetric converging-diverging nozzle*, International Journal of Multiphase Flow **106**, 34-45 (2018). The footnotes with symbols are not present in the original article.

2.1. INTRODUCTION

Cavitation is a phenomenon with mostly negative effects, occurring in a wide variety of applications. For instance, cavitation occurring in turbomachinery may cause erosion of the impeller blades, noise production, and system vibrations, leading to failure fatigue (Balas et al., 2006; Van Terwisga et al., 2009). Intense cavitation occurring at ship propellers is also a problem, because of efficiency drop, wear, and noise production. However, in some cases cavitation can have positive effects, for example, to mix two or more dissimilar fluids such as in marine diesel engines (Avellan et al., 1991; Habchi et al., 2014). Understanding the cavitation physics is important because then the harmful effects of cavitation can be minimized and the positive effects can be maximized.

One interesting form of cavitation is the periodic shedding of cavitation clouds. Due to the complex mix of unsteadiness, two-phase flow dynamics, turbulence and fluid-structure interactions, this is a very complicated research field. In previous research usually three different test geometries are used to visualize this cloud shedding: (1) hydrofoils (Callenaere et al., 2001; Danlos et al., 2014; De Lange and De Bruin, 1997; Foeth et al., 2008; Long et al., 2018), (2) planar converging-diverging nozzles with a rectangular cross-section ("wedges") (Chen et al., 2015; Croci et al., 2016; Ganesh et al., 2016; Jana et al., 2016) and (3) converging-diverging axisymmetric nozzles ("venturis") (Hayashi and Sato, 2014; Long et al., 2017; Rudolf et al., 2014; Tomov et al., 2016). Although in all geometries periodic cloud shedding can be observed, due to the specific shape of each of the geometries, they all have their own characteristic flow dynamics. Generally, the venturi has the highest contraction ratio, due to its shape, which results in a wider dynamic cavitation range. In this research, a venturi has been used, which gives us the ability to clearly distinguish between different cavitation mechanisms due to their more intense nature.

Thus far in the literature, two different mechanisms that initiate periodic cloud shedding are described: the re-entrant jet mechanism and the bubbly shock mechanism. There is also a third mechanism, the side-entrant jet (Foeth et al., 2008; Ji et al., 2013; Peng et al., 2016), which is associated with the part of the re-entrant flow that has a strong spanwise velocity component such as in hydrofoils. Decaix and Goncalves (2013) reported on the presence of an oblique mode of the cavity oscillations and Timoshevskiy et al. (2016) concluded that the oblique mode of sheet cavity oscillations associated with the development of the spanwise instability exists for all test objects independent of their shape. Because of the similarity between the side-entrant jet to the re-entrant jet, the side-entrant jet is not discussed in further detail.

In the re-entrant jet mechanism, the occurrence of periodic shedding is generally related to the presence of a re-entrant flow in the closure region of the cavity which forms as the liquid flow outside the cavity reattaches in the closure region (Bensow, 2011; Ganesh, 2015). Knapp (1955) discovered a re-entrant jet by means of high-speed imaging. Different studies towards the velocity of the re-entrant jet have been conducted. Pham et al. (1999) measured the velocity of this jet by means of a surface electrical probe. At different foil positions, the mean velocity of the jet was determined. They found that the velocity of the jet was of an equal order of magnitude to that of the free stream velocity. It was also found that the velocity of the re-entrant jet increased with the distance from the leading edge. They further observed that the frequency of the re-entrant jet, measured

with the surface electrical probes, was equal to the cloud shedding frequency, measured by pressure measurements. The authors concluded that the re-entrant jet mechanism drives the cloud cavitation shedding process. Kawanami et al. (1997) also investigated the influence of the re-entrant jet on the cloud shedding. In this study, an obstacle was placed at the wall, in order to prevent the re-entrant jet to proceed to the vapor cloud origin. The re-entrant jet could not proceed and vapor cloud shedding was not observed during this experiment. In this way, they proved that the re-entrant jet is the cause of cavity cloud shedding. Callenaere et al. (2001) stated that two parameters are important for the re-entrant jet: the cavity thickness with respect to the re-entrant jet thickness and the adverse pressure gradient. The latter is the sum of the pressure recovery and the friction losses that the re-entrant jet encounters in order to propagate to the leading edge. If the energy budget provided by the adverse pressure gradient is not sufficient to overcome these friction losses, the re-entrant jet cannot proceed and the unsteady cavitation cloud shedding is not started. This clearly indicates that re-entrant jet cavity shedding is a pressure driven phenomenon. Research towards the shedded cloud velocity was performed by Kubota et al. (1989). They studied the flow structures around unsteady cloud cavitation on a hydrofoil experimentally. To that end, Laser Doppler Anemometry with a conditional sampling technique was used. It was found that the convection velocity of this cloud is lower than the global flow velocity. Stanley et al. (2014) experimentally investigated the re-entrant jet mechanism for periodic cloud shedding in a large-scale cylindrical orifice. They provided a refined mechanism of the re-entrant jet development. Unrestricted optical access to the near-wall region showed the presence of a liquid film throughout the shedding cycle. The mechanism causing the periodic shedding was shown to be a combination of a traveling wave style deformation of the cavity interface and a translational pulse, each with different velocities. Generally, for the re-entrant jet driven cavitating flow a Strouhal number based on the cavity length in the range of 0.18-0.35 is found, irrespective if the flow is external (hydrofoil flow) or internal (venturi flow) (Dular et al., 2012; Ganesh, 2015; Stutz and Reboud, 1997). This Strouhal number (St_l) is defined as:

$$St_l = \frac{fl}{u_0}, \quad (2.1)$$

where l is the length of the cavity at the time of detachment, the shedding frequency of the cavitation clouds is given by f and u_0 is the free stream velocity of the flow. An alternate definition of the Strouhal number is also used in axisymmetric geometries, in which the throat diameter¹ is used as characteristic length. Therefore, the cavity length (l) is replaced with the throat diameter (d):

$$St_d = \frac{fd}{u_0}. \quad (2.2)$$

In 1964, the occurrence of condensation shocks in cavitating inducers was predicted by Jakobsen (1964); they were studied experimentally by Reisman et al. (1998) using a hydrofoil. Recently, the bubbly shock mechanism as an initiator of the unsteady cloud

¹For constant diameter geometries, such as diesel injector nozzles, the characteristic length is simply the diameter.

cavitation shedding was mentioned by Ganesh (2015). In this study, time-resolved X-ray densitometry was used to visualize the void fraction in the flow field. These experiments were performed on a 2D wedge. Gnanaskandan and Mahesh (2016) performed large-eddy simulations on the same configuration to analyze transitional cavitation behavior. Detailed analysis of velocity and void fraction variations were presented. In Ganesh et al. (2016) the bubbly shock phenomenon is observed. According to the authors, this mechanism starts to play a role when the cavitation number is decreased and by that the void fraction in the cavity is increased. In this situation, the shedding process is initiated by the bubbly shock mechanism instead of the re-entrant jet mechanism. The bubbly shock phenomenon can be explained as follows: at a certain moment, a well-defined void fraction front can be observed in the cavity. This front spans the complete cavity height and propagates upstream in the direction of the wedge apex. If the void fraction front reaches the wedge apex the attached cavity is separated from the wedge apex and the vapor cloud is shed. Wang et al. (2017) reported that a shock wave is generated by the collapse of a large-scale cavity structure, and propagates within the attached cavity. A significant void fraction variation was witnessed across the shock wave front. Based on these observations, it can be argued that cavity shedding in the bubbly shock regime is shock-wave driven.

Arndt et al. (2000) performed an experimental and numerical investigation on a 2D NACA 0015 hydrofoil to understand the two competing mechanisms responsible for the shedding of cloud cavitation. They found that at high values of $\sigma/2\alpha$ (σ is the cavitation number and α is the angle of attack), the re-entrant jet mechanism dominates while at low values of $\sigma/2\alpha$, the bubbly shock mechanism dominates. A sharp transition was observed at $\sigma/2\alpha = 4$.

At the moment, there is limited literature present which quantitatively clearly distinguishes between the re-entrant jet mechanism and the bubbly shock mechanism. We introduce a method based on high-speed visualization and Strouhal numbers to identify and distinguish both mechanisms without the need for void fractions. The data will be used in the future to validate numerical models.

The outline of this chapter is as follows: the experimental details are explained in Section 2.2 of the chapter, while Section 2.3 explains in detail the data processing and methods used to explain the flow dynamics in different cavitation regimes. The results are reported in Section 2.4. Discussions and the conclusions follow in Section 2.5 and Section 2.6, respectively.

2.2. EXPERIMENTAL DETAILS

2.2.1. FLOW FACILITY

In Fig. 2.1, a picture of the venturi can be seen with its geometrical parameters. This venturi is milled out* from a rectangular block of polymethylmethacrylate (PMMA, 'perspex'). The most important property of this material is the high light transmission because the refractive index of perspex is very close to that of water. This gives good optical access to the cavitation dynamics. The flow direction is from left to right. The convergence and

*The interior of the venturi was polished to avoid cavitation inception due to roughness. Note that the throat has a sharp edge.

divergence angles (2α) are 36° and 16° , respectively (inspired by previous studies: Hayashi and Sato (2014); Long et al. (2017); Rudolf et al. (2014); Tomov et al. (2016)). The divergence angle of 16° is selected, in order to avoid flow separation while maintaining fairly rapid pressure recovery (Idelchik and Fried, 1986). Furthermore, an area ratio of 1:9 (area of the throat versus exit area) is chosen. A schematic overview of the experimental setup

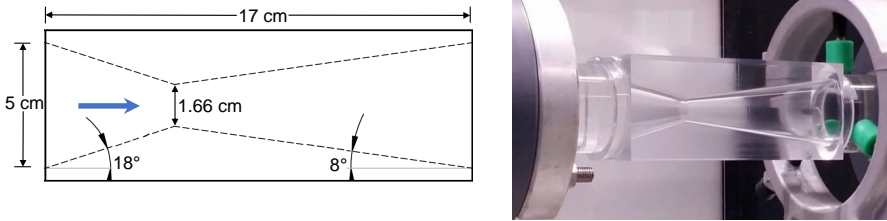


Figure 2.1: (Left) The geometry and relevant dimensions of the converging-diverging section. (Right) Photograph of the venturi in the experimental setup.

is given in Fig. 2.2. The flow in the closed loop system is driven by a centrifugal pump, which is installed 2 m below the measurement section to avoid cavitation in the pump. The volumetric flow rate is measured with a KROHNE flowmeter (type: IFS 4000F/6).

The length available for development is $40D$, in order to have a fully-developed turbulent flow entering the test section (Nikuradse, 1932). The upstream pressure transducer is located 0.31 m before the venturi throat and the downstream pressure transducer is located 0.73 m after the venturi throat. The tube after the venturi has a length of 1.4 m. There is a gradual transition from this tube to the pressure recovery section, with an angle of 5.7° , in order to avoid flow separation and minimize flow losses (White, 2003). After this transition, the pressure in the flow is recovered in a pressure recovery section, with an overall length of 1.92 m. Furthermore, temperature measurements are performed in the pressure recovery section.

At the end of the pressure recovery section, a vertical water column is present, to collect the air bubbles entrained in the flow during degasification and to vary the global static pressure of the system. A vacuum pump is used to control the global static pressure below ambient pressure down to 20 kPa absolute.

2.2.2. EXPERIMENTAL PROCEDURE

Before the measurements, the water is degasified using the vacuum pump and a water sample is taken for the determination of the gas content in the system using an oxygen sensor (RDO PRO-X Probe). The setup is operated for a few minutes before the measurement series is started, in order to mix the water in the system to obtain a uniform water temperature. The global static pressure (8 in Fig. 2.2) of the system is set to a fixed, prescribed value and the measurements are started when the pressure measurements are constant. For the fixed, prescribed global static pressure, measurements are performed at different flow velocities. By means of a data acquisition system, all the sensor values

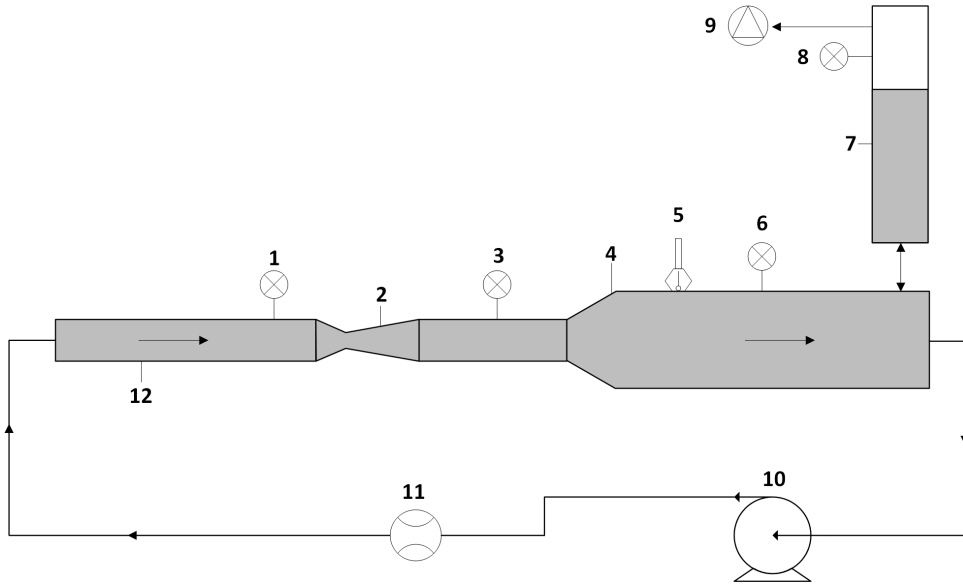


Figure 2.2: Schematic overview of the experimental facility. 1,3,6,8-pressure transducers, 2-venturi, 4-pressure recovery section, 5-temperature sensor, 7-water column, 9-vacuum pump, 10-centrifugal pump, 11-electromagnetic flowmeter, 12-inlet pipe.

(pressure, flow rate, and temperature) and high-speed images (explained in more detail in the later paragraph) are stored simultaneously. After performing a measurement, the flow velocity is decreased in such a way that cavitation in the venturi is avoided, in order to prevent heating of the system. In the end, the oxygen content is measured again by taking a water sample from the setup. Throughout the chapter, the flow conditions will be reported as the cavitation number (σ):

$$\sigma = \frac{p - p_v}{\frac{1}{2} \rho u_0^2}, \quad (2.3)$$

where p is the downstream pressure (6 in Fig. 2.2), p_v is the vapor pressure² of the liquid at the temperature of the setup, ρ is the density of the fluid and u_0 is the free stream velocity of the flow at the venturi throat. Furthermore, the pressure loss coefficient K is given by:

$$K = \frac{\Delta p}{\frac{1}{2} \rho u_0^2}, \quad (2.4)$$

where Δp is the pressure loss over the venturi (calculated from 1 and 3 in Fig. 2.2).

2.2.3. SHADOWGRAPHY

The cavity dynamics are captured using shadowgraphy. A schematic overview of this method is shown in Fig. 2.3. In this method, the measurement target is placed in between

²The vapor pressure is calculated using the Antoine equation at the temperature measured during the experiments (14 °C - 22.4 °C).

a light source and a high-speed camera. The light source illuminates the target from the back side in the direction of the CMOS camera sensor. Preferably a homogeneous light source is used, such as the LED panel used here. Every object that appears in the target blocks the light from the source behind. This results in a dark spot in the camera images. In this way the presence and position of vapor cavities can be determined. As the refractive index of PMMA is relatively close to water the curved inner surface of the venturi did not result in considerable image distortion due to refraction. This was confirmed by placing a calibration target with a regular pattern of markers at the midplane of the venturi. After the calibration an overall uncertainty of less than 1 pixel is found. Please see Hogendoorn (2017) for further explanation.

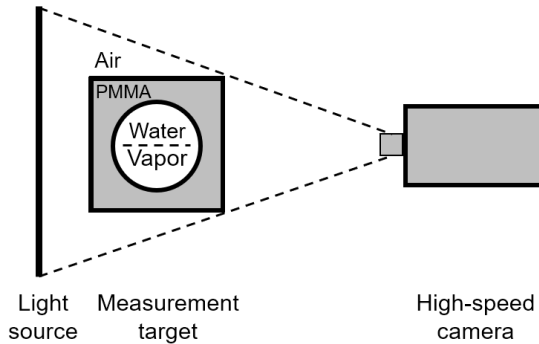


Figure 2.3: Sketch of the image capturing technique. The viewing angle in the experiments is smaller than the sketched angle.

A high-speed camera (Photron Fastcam APX RS) in combination with a 105mm/2.8 FX AF MICRO-NIKKOR object-glass is used for recording. For the experiments two different acquisition settings are used, in both cases an aperture $f^{\#}=2.8$ is used as well as a field of view of 1024×336 pixels. In the first case, an exposure time of $1/9000$ Hz is used in combination with a framerate of 800 Hz and a recording time of 4 seconds. This video is used for the determination of the cavity shedding frequency. The sample frequency of 800 Hz is selected to meet the Nyquist criterion, because a maximum shedding frequency of 300 Hz is expected.

In the second case a framerate of 9000 Hz is used in combination with an exposure time of $1/9000$ Hz and a recording time of 0.1-0.15 seconds due to practical limitations on the amount of data. This video is used for the cavity length determination and to generate x-t diagrams.

2.3. DATA PROCESSING

2.3.1. IMAGE PROCESSING

Fig. 2.4(a) shows a typical snapshot from a high-speed image sequence. Black indicates the presence of a vapor cavity and the light gray region indicates a liquid phase with some amount of bubbles. It also shows the coordinate system used. As the vertical axis is not used (as will be discussed later), its origin is set arbitrarily. The origin of the

horizontal axis, coinciding with the axial/streamwise direction, is set at the throat of the venturi. The axial location (X) is made dimensionless using the length of the diverging section ($L = 11.87$ cm). A qualitative comparison of the cavitation dynamics between the horizontal and the vertical plane of the venturi has been performed by placing a mirror at an angle of 45° below the venturi. The side-view and the bottom-view were visualized simultaneously, in order to verify whether the cavitation dynamics are axisymmetric. No significant difference was found, therefore gravity can be neglected. The cavity length at moment of detachment (l) is determined from the average grayscale (β), which can be seen in Fig. 2.4(b). This average intensity is obtained by averaging the dashed rectangle in Fig. 2.4(a), along the Y -axis. A threshold value of 0.2 is selected to obtain a representative cavity length. The moment of detachment is determined by the gray value at the throat position. When this gray value drops below the threshold value, the cavity is detached. The corresponding length (l) is determined using the preceding frame (i.e. showing the attached state). Since there is a steep gradient in β at the locations of the cavity boundary, the exact details of the threshold method are of minor importance. The lengths determined using this (automated) method also matched visual observations. In order to increase the accuracy of the cavity length determination, an average of five l values is used. An uncertainty analysis points out that the error due to the finite temporal resolution is proportional to $e \propto u_0/F_s$ where F_s is the frame rate, which results in an error of less than 4% of the cavity length.

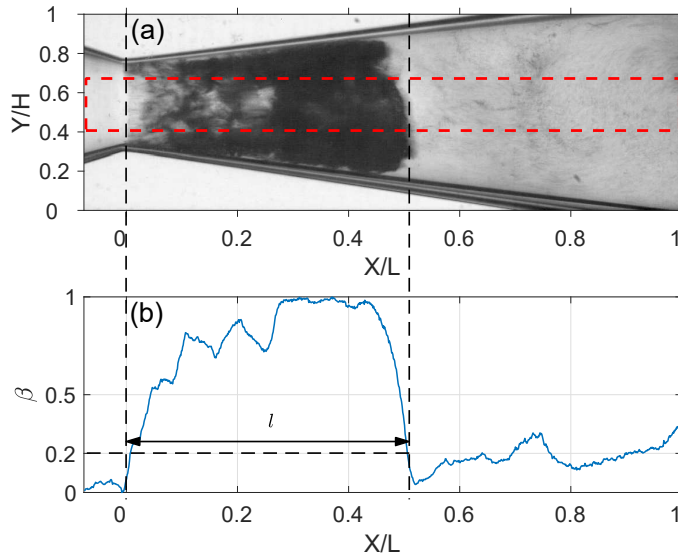


Figure 2.4: A typical snapshot showing cavitation in the venturi. The dashed rectangle indicates the region that is used to calculate the average intensity (β). The corresponding result for β as a function of the axial distance is given in the bottom figure, which also shows the method to determine the cavity length. See text for further details on this procedure.

2.3.2. X-T DIAGRAMS

At each time step, the image data is averaged along the Y-axis over a range spanning $Y/H = 0.4$ to 0.68 , corresponding with 100 pixels, as shown in Fig. 2.4(a). Rectangular averaging is chosen instead of a wedge shape, because variations along the curvature have a small effect. The focus of this research is on global cavitation characteristics, therefore we remove small local variations using this averaging process. This results in a single line of data, representing the instantaneous overall shape of the cavitation cloud. By stacking these lines of data, an x-t diagram is obtained, which will be useful to describe the dynamics of the cavitation process. The x-t diagram is useful for the determination of unsteady cavitation behavior and it is a common data processing method in the field of cavitation (Budich et al., 2018; Charrière and Goncalves, 2017; Saito and Sato, 2007). An example of a typical x-t diagram is shown in Fig. 2.5. Note that the color-coding is inverted: black represents the liquid phase, while light gray represents the vapor phase.

The frequency of the shedding cycle is determined by performing a Fast Fourier Transform (FFT) in temporal direction (i.e. 'vertical' in an x-t diagram as indicated with arrow 1 in Fig. 2.5). Different X/L positions can be selected for the FFT. In order to improve the estimate of the frequency, m positions are selected at which the frequency is determined. In the end the frequency is averaged over these m positions. The procedure for $m = 1$ is explained in more detail. A number of signal processing approaches are used for a better frequency determination from this signal. In the first place, this signal is divided into n parts. Subsequently, these parts are multiplied with a hamming window, in order to account for edge effects. From each individual signal the power spectrum is determined by means of an FFT. All n powerspectra are averaged in order to reduce the noise that is present in one spectrum. From this averaged power spectrum the frequency which contains the most power is selected with two neighboring points on both sides. By means of a Gaussian curve fit through these five points, the resolution of the power signal is increased. The frequency corresponding to the maximum point of this Gaussian is determined in order to obtain the final shedding frequency. In case of $m > 1$ positions, the frequencies are averaged along the X dimension as well.

For high shedding frequencies (≈ 200 Hz) a maximum uncertainty of 5% is found (based on the 95% probability interval), because of the rapid motion. For low shedding frequencies, the dynamics are captured much better, which results in an uncertainty of 1%.

The cavity growth rate and advection velocity are represented by the inverse of the slopes of dashed lines indicated by 2 and 3, respectively. From the shedding frequency and the cavity length at moment of detachment (4), the cavity growth velocity is determined, which is calculated as $u_c = l/t = lf$.

An uncertainty analysis for the shedding frequency determination is performed. To this end, a series with nearly 30,000 shedding cycles is measured and divided into eight parts, where it is assumed that these parts are independent of each other since they contain enough shedding cycles. An uncertainty of less than 5% is found, based on the 95% probability interval. This was also the case for a division of 72 parts, for an entire length of the high-speed image sequence. We conclude that a recording time of 4 seconds is sufficiently long for frequency determination.

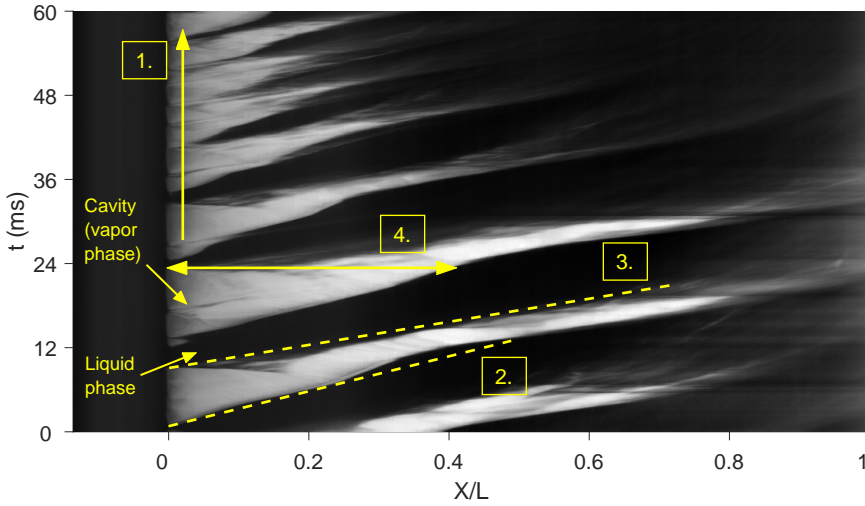


Figure 2.5: An x-t diagram at $\sigma = 0.88$, showing the cavitation dynamics. Note that the colors are inverted with respect to the original image (vapor is light gray, liquid is black). The labels are discussed in the text.

2.4. RESULTS

2.4.1. PRESSURE LOSS AND CAVITY LENGTH

The intensity of cavitation can be described using the cavitation number. With an increase in flow velocity, the cavitation number decreases, suggesting more intense cavitation. For a decreasing cavitation number, we observe that the cavity length increases at the time of detachment. This is schematically visualized for four different cavity lengths in Fig. 2.6(inset). This figure is an approximation of the cavity behavior observed in the images. It can be seen that the effective throat diameter is narrowed by the presence of the growing cavity, hence the effective throat diameter is a function of σ .

Because of the narrowed throat diameter for decreasing cavitation number, the pressure loss over the venturi will be higher. This is evident from measurement results, shown in Fig. 2.6. Here the cavitation number is varied by changing the flow velocity at different static pressures, and the pressure loss coefficient K is reported. It can be seen that all points collapse on one line. This implies that flow blockage is a function of cavitation number only (i.e. not of pressure or flow velocity independently). The points corresponding to the global static pressure of 30 kPa are deviating from the global trend because air bubbles are entrained in the circuit due to tiny leakages during the measurements at this relatively low pressure. A linear relation between the pressure loss coefficient and cavitation number was also found by Rudolf et al. (2014).

Fig. 2.7 schematically shows the pressure and velocity profiles along the throat. The top half shows the velocity profile (solid blue line) based on mass conservation and the bottom half shows the corresponding pressure profile (solid blue line) estimated using the 1D Euler equation. For the cases with a significant cavity, we can no longer predict the pressure using this method. Using the inset of Fig. 2.6, however, we can predict it

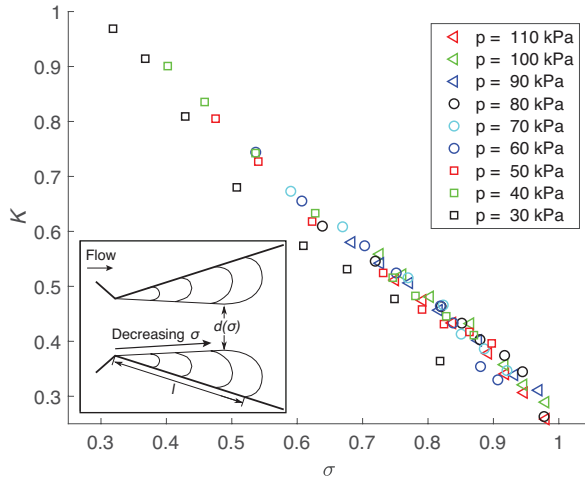


Figure 2.6: Pressure loss coefficient (K) as a function of the cavitation number (σ). Only cases with cavitation are shown. The inset shows how the cavitation regions restrict the effective throat area more and more as the cavitation number is lowered.

qualitatively: for a very low σ we have a very large cavity which extends the effective throat diameter, which leads to a larger high-velocity region. For low σ pressure recovery is thus slower and not complete, as shown by dashed lines (Fig. 2.7). This is in agreement with the K values reported in Fig. 2.6. The role of pressure ratio to the cavity length is explained in detail recently by Long et al. (2017). Fig. 2.7 will be helpful for the interpretation and discussion of the results in Section 2.5.

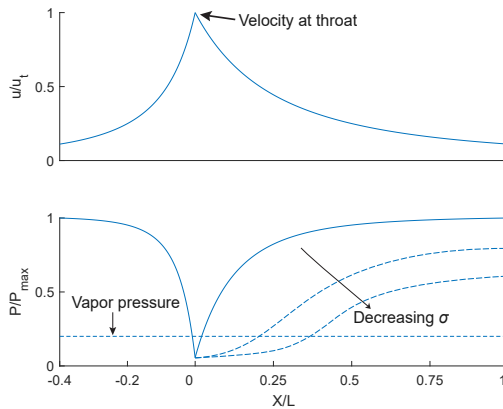


Figure 2.7: Schematic representation of the dimensionless velocity and pressure profiles along the throat. The velocity is normalized with the maximum velocity at the throat and pressure with the upstream maximum pressure.

The averaged cavity lengths at the time of detachment are also measured as a function of cavitation number and are presented in Fig. 2.8. The cavity lengths are non-dimensionalized with the throat diameter (d) of the venturi. All measurement points collapse on one curve for the cavitation number based on the global static pressure. For starting cloud cavitation shedding, the dimensionless cavity lengths are of order unity. For decreasing cavitation number, cavities grow longer before detachment, up to 12d in the most extreme case.

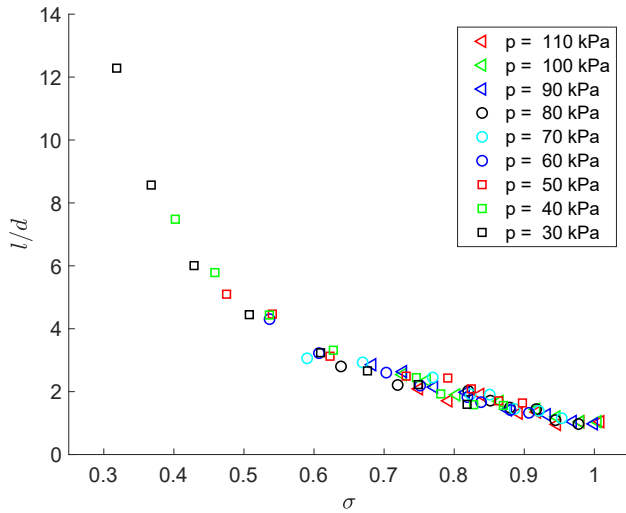


Figure 2.8: The average length of the cavity at the time of detachment (scaled with the throat of the venturi) as a function of the cavitation number.

2.4.2. SHEDDING FREQUENCY AND TEMPORAL DEVELOPMENT OF CAVITY CLOUD

The shedding frequency is determined from the x - t diagram as discussed in the previous section. This can be presented in a non-dimensional form with the Strouhal number St_d . The Strouhal number is also a function of cavitation number as can be seen in Fig. 2.9. It follows that all points collapse on one curve again and the shedding frequency is a function of cavitation number. The inverse of the shedding frequency gives the integral time scale, which corresponds to the process of cavity development to the time of detachment. Multiplication of the shedding frequency with the cavity length scale at the time of detachment gives the global growth rate of the cavity front: $St_l \sim fl/u_0 \sim u_c/u_0$, where u_c is the cavity front velocity. This Strouhal number (St_l) is presented as a function of cavitation number in Fig. 2.10. It can be seen that not all the points are collapsing on one curve, as in the case of the cavity length and time scales, but nevertheless, a global trend can be observed. A minimum, as well as the highest spread, can be observed for $0.75 < \sigma < 0.95$. Change is more apparent in frequency/time scales, so we use St_d for further analysis.

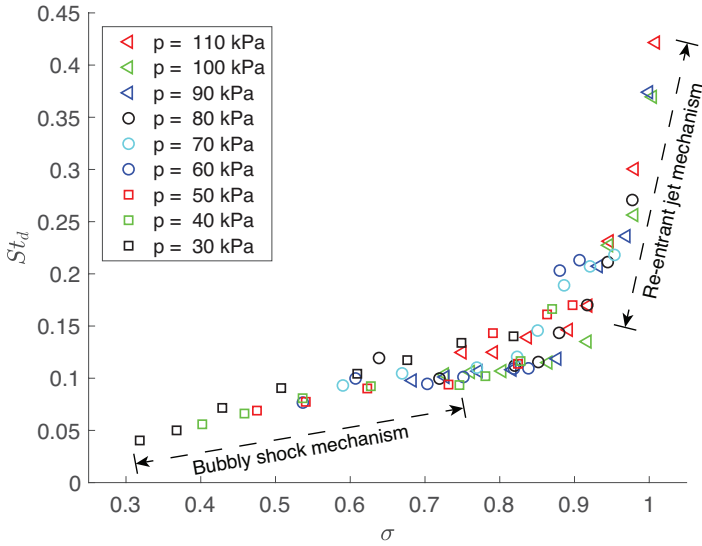


Figure 2.9: Dimensionless frequency of the cavitation shedding cycle as a function of the cavitation number.

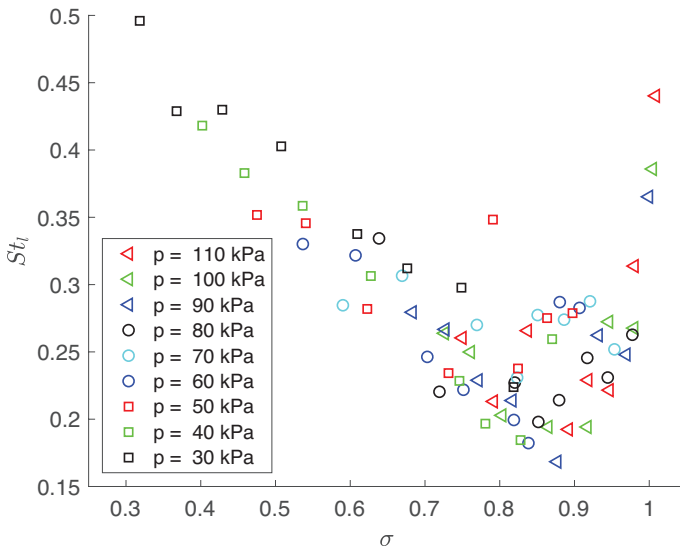


Figure 2.10: Cavitation shedding cycle as a function of the cavitation number; the dimensionless frequency is here obtained using the cavity length.

From Fig. 2.9, visual inspection of the video data, and the x-t diagrams (shown and discussed in detail in the next section), two different cavitation mechanisms can be

identified as a function of cavitation number. For $\sigma > 0.95$ cloud cavitation shedding is governed by the re-entrant jet mechanism. For $\sigma < 0.75$ cloud cavitation shedding is governed by the bubbly shock mechanism. The cavitation region in between is governed by both mechanisms, so we call it the transition region³. For $\sigma < 0.1$, we do not see periodic cavitation: there is strong jet cavitation in this case. The downstream vapor cloud collapse is not strong enough to cause shedding. As the focus of this study is on the dynamics of cavitation, we omit this steady jet cavitation from our analysis.

2.4.3. RE-ENTRANT JET MECHANISM AND BUBBLY SHOCK MECHANISM

From Section 2.1, it followed that the re-entrant jet mechanism is pressure gradient driven, whereas the bubbly shock mechanism is shock wave driven. To investigate these mechanisms, cavitation characteristics must be examined in more detail. The cavitation essence is well presented in an x-t diagram, because in this diagram the cavity time and length scales are visualized in a clear way. In supplementary data of Jahangir et al. (2018), three movies can be found that further illustrate the findings from the x-t diagrams.

First an x-t diagram for $\sigma > 0.95$ is examined in more detail. From preliminary visual inspection, the re-entrant jet mechanism is expected as a prevalent mechanism for cavity shedding at high σ . To that end the x-t diagram corresponding to a cavitation number of $\sigma = 1$ ($u_0 = 13.5$ m/s, $f = 188.6$ Hz and $p = 90$ kPa) is selected. This diagram is shown in Fig. 2.11.

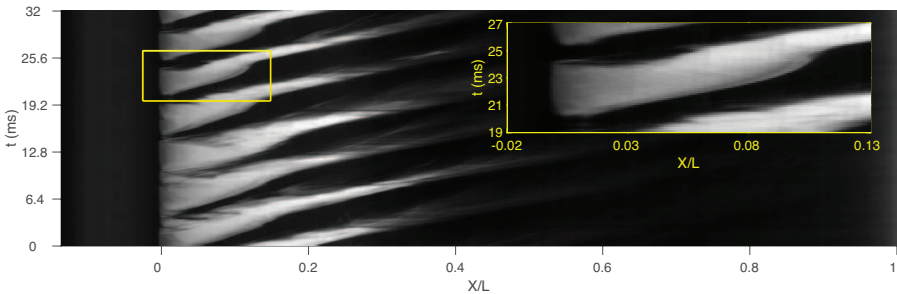


Figure 2.11: X-t diagram of an experiment in the re-entrant jet regime. The light gray regions indicate the presence of vapor and the black regions indicate the presence of liquid. An enlargement of a typical shedding cycle is presented in the (yellow) box in the figure. For this case $\sigma = 1$ (corresponding to: $u_0 = 13.5$ m/s, $f = 188.6$ Hz and $p = 90$ kPa).

The light gray regions indicate the presence of a cavity (vapor) and the black regions indicate the presence of liquid. A typical shedding cycle is captured with a rectangular box and enlarged on the right side of the diagram. It can be seen that this cavity starts to grow at $t \approx 20$ ms and grows linearly until a certain point. After that point the slope becomes steeper, indicating that the cavity front growth rate decreases. During this front velocity decrease, cavity detachment can be observed at $t \approx 24$ ms. The back side of the cavity moves near-instantaneously from $X/L = 0$ to $X/L = 0.04$. This sudden detachment is

³We see the transition at $\sigma/2\alpha \approx 3$ (where α is the divergence angle) as compared to 4 reported by Arndt et al. (2000). This is likely due to the difference in geometry (venturi versus hydrofoil).

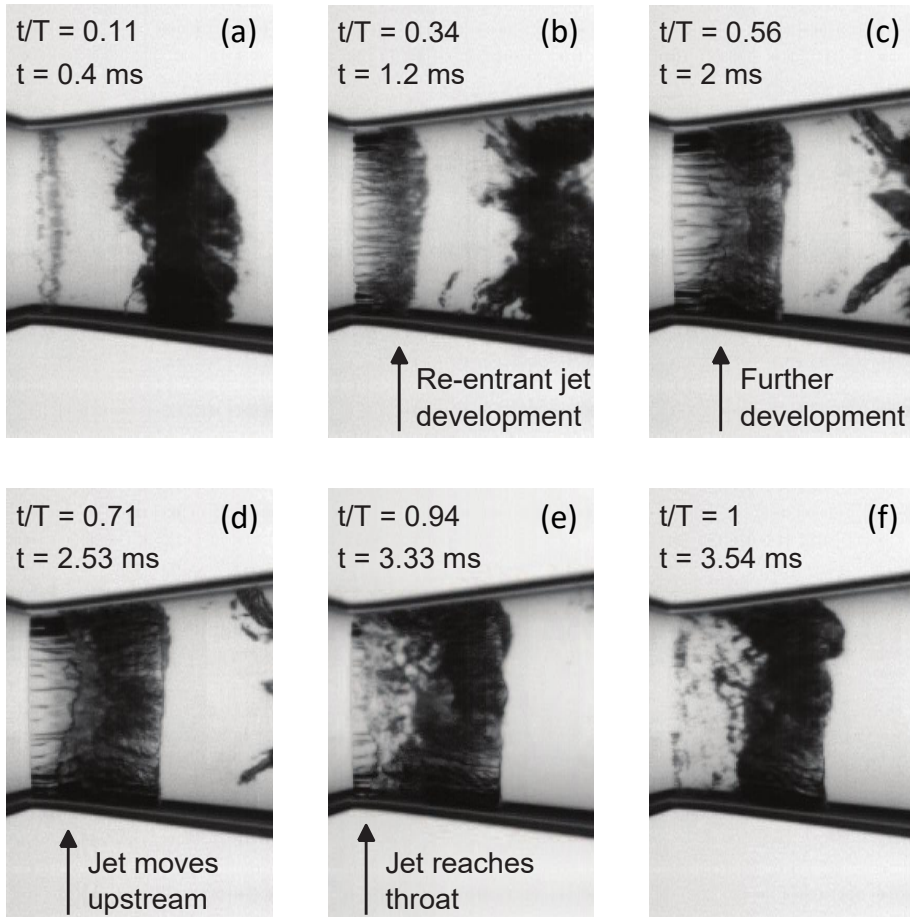


Figure 2.12: Video frames of re-entrant jet development at $\sigma = 1$. In (a) and (b), cavity development can be seen. In (c) the re-entrant jet starts to develop. In (d) the jet front can be recognized by the chaotic interface, which can be seen above the arrow. The propagation of the jet front towards the venturi throat can be seen in (e). In the end, cavity detachment is caused by the re-entrant jet as can be observed in (f).

possibly caused by a pressure gradient. After this sudden detachment, the vapor cloud is advected with a positive velocity. Furthermore, after detachment and partial advection, the cavity front velocity increases to a constant velocity (constant slope). This "stick-slip" behavior is typical for the examined regime. In the stick-slip behavior, the backside (upstream part) of the cavity sticks to the venturi throat and at a certain point this backside suddenly detaches, which is associated with slip. The stick-slip behavior of the re-entrant jet mechanism is also evident in the simulations of Frikha et al. (2008). The re-entrant jet can be observed more clearly by particle/bubble tracking in individual video frames as shown in Fig. 2.12.

The video frames are chosen for $\sigma = 1$. One complete cycle of the re-entrant jet mechanism and shedding can be seen. The Fig. 2.12(a) starts at $t/T=0.11$, where T is the total time of one shedding cycle. It can be seen that the cavitation bubbles start to appear. The re-entrant jet starts to develop (Fig. 2.12(b)) and this development proceeds to $t/T=0.56$ (Fig. 2.12(c)), after which the jet front starts to propagate in the venturi throat direction (Fig. 2.12(d)). The re-entrant jet front can be recognized by the chaotic interface, which can be seen above the arrow. The propagation of the jet can be seen in Fig. 2.12(e) and the re-entrant jet reaches the throat and the entire cavity detaches from the throat, as shown in Fig. 2.12(f).

From the high-speed images, the mechanism, which causes cavity detachment becomes also clear. In combination with an adverse pressure gradient (the pressure downstream is relatively high and the pressure in the cavity is approximated by the vapor pressure), a re-entrant jet starts to develop. This re-entrant jet disconnects the cavity from the venturi throat, whereafter the cavity is advected with the flow and a new cavity starts to grow.

Re-entrant jet front tracking analysis is performed in order to estimate the re-entrant jet velocity. Typical velocities of 1.1 - 3.4 m/s are found for mean flow velocities of 14.4 - 14.8 m/s at the venturi throat (Hogendoorn, 2017).

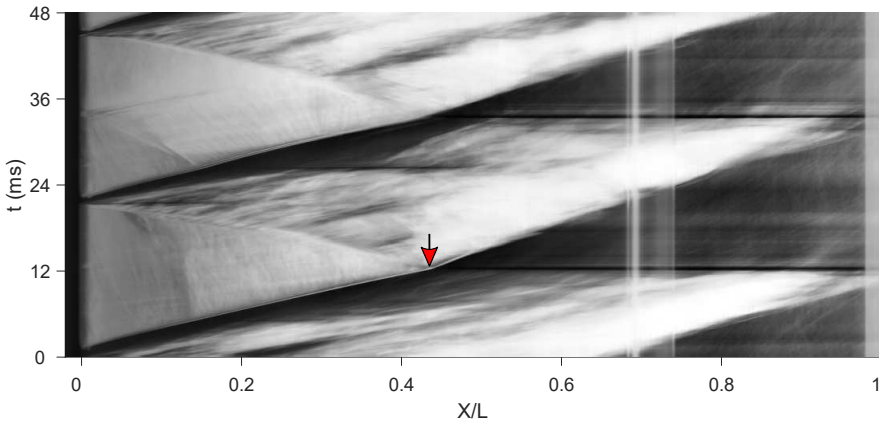


Figure 2.13: X-t diagram of an experiment in the bubbly shock regime. The light gray regions indicate the presence of vapor and the black regions indicate the presence of liquid. The cavitation number is $\sigma = 0.40$ ($u_0 = 13.7$ m/s, $f = 46.1$ Hz and $p = 40$ kPa).

In Fig. 2.13, the bubbly shock dynamics are presented in the form of an x - t diagram. A case with a cavitation number of $\sigma = 0.40$ ($u_0 = 13.7$ m/s, $f = 46.1$ Hz and $p = 40$ kPa) is shown. It can be seen that a cavity starts to grow at $t \approx 0$ ms, with a constant growth rate (linear slope of the black-white interface). At $t \approx 12$ ms a change in growth rate can be observed (red marker), this is exactly at the point where a nearly horizontal black line (coming from the right) hits the cavity. This black line indicates that there is a liquid phase present in the venturi at this time. It can also be observed that above this black line, at $X/L \approx 0.8$, the previously shed cavity cloud vanishes. It follows that, at the time of cavity collapse, a pressure wave is emitted in both directions. The emitted pressure wave is propagating upstream through the growing cavity, as can be seen from the density change in the growing cavity (light gray region). When the pressure wave reaches the venturi throat, the cavity detaches and is thereafter advected with the flow. This shedded cavity also collapses further downstream, again emitting a pressure wave, which is the trigger mechanism for the next cavity detachment.

The corresponding video frames are shown in Fig. 2.14[†]. Fig. 2.14(b) and (c) are just before the time of complete cavity collapse. The complete collapse can be seen in Fig. 2.14(d). The vapor cloud collapses at approximately 10d downstream of the throat. The collapse causes a pressure wave, which is emitted in both directions. In Fig. 2.14(e)-(g), the position of this (left running) pressure wave is indicated with an arrow. After the passage of the pressure wavefront, a new equilibrium state between the vapor and liquid phase must be formed. Due to the pressure rise after the pressure wavefront, the void fraction in the (growing) cavity decreases by partial condensation. This was also observed in Fig. 2.13, where a jump in grayscale over the pressure wave was mentioned. When the pressure wave reaches the venturi throat, the cavity detaches, as follows from Fig. 2.14(h). Wu et al. (2017) also observed a similar pressure wave in a 2D convergent-divergent test section.

The velocity of the pressure wave can be calculated from the inverse of the slope in the x - t diagram. First, the pressure wave velocity in the growing cavitation cloud is determined, because this gives important insights about the physics of cavity detachment. The pressure wave path is well described with a second-order polynomial, as can be seen in Fig. 2.15(a) with a red dashed curve. The velocity of the pressure wave is given by the inverse of the derivative of this path. The pressure wave velocity in the laboratory frame of reference is given by the blue, dashed line in Fig. 2.15(b). Because the pressure wave travels through the cavity, the absolute velocity of the pressure wave can be best represented by adding the cavity growth rate to the relative pressure wave velocity. This velocity profile is given by the blue, continuous line in Fig. 2.15(b). It should be remarked that after pressure wave impact (red marker), this cavity growth rate changes, as can be seen from the change in slope, in Fig. 2.15(a). This change in cavity growth velocity is probably caused by a higher downstream pressure, resulting in a decreasing growth velocity with a factor 1.19 with respect to the growth velocity before impact.

Thus far two typical cases are considered, where either the re-entrant jet mechanism or the bubbly shock mechanism is the prevalent mechanism for cavity shedding. Both mechanisms are observed in the transition region where $0.75 < \sigma < 0.95$. To this end an

[†]The exit of the venturi and the start of the circular tube have the same diameter (5 cm). The difference in the figure is caused by the optical distortion due to the connection of the PMMA block with the tube.

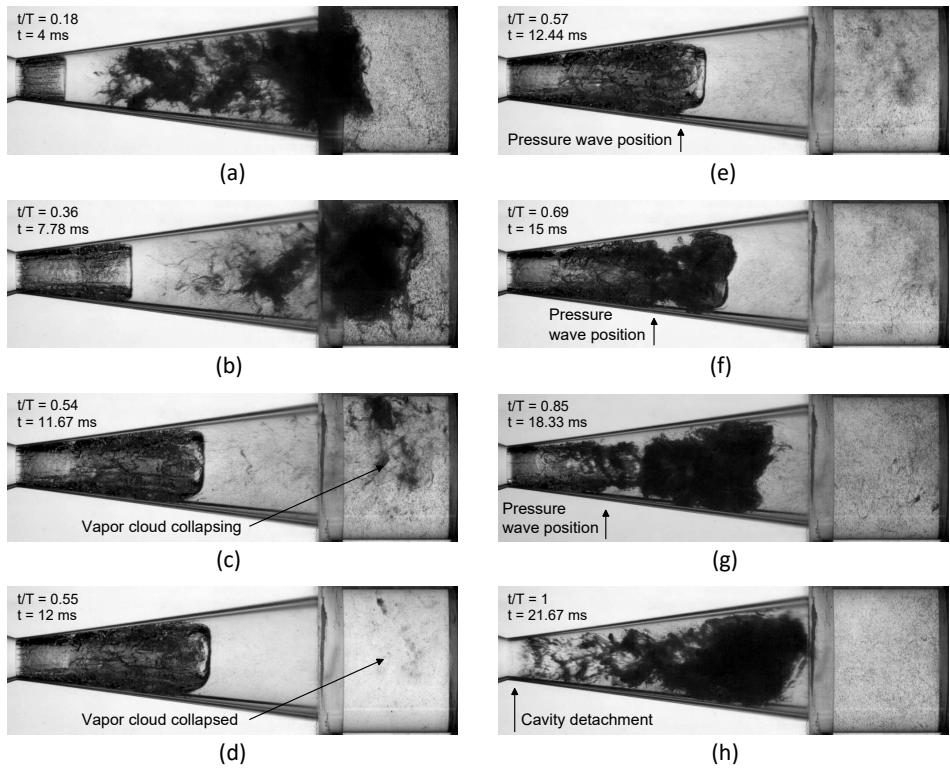


Figure 2.14: Video frames of bubbly shock development. In (a) and (b) a growing cavity can be seen (left side of sub-panels) and previously shed cavity (right side of sub-panels). In the subsequent (c) and (d) the cavity collapses completely and a pressure wave is emitted. The position of this pressure wave is tracked and indicated in (e)-(g). Condensation of the cavity beyond the pressure wave can be seen due to the higher pressure there. Cavity detachment can be observed when the pressure wave reaches the throat (h). The cavitation number is $\sigma = 0.40$ ($u_0 = 13.7$ m/s, $f = 46.1$ Hz and $p = 40$ kPa).

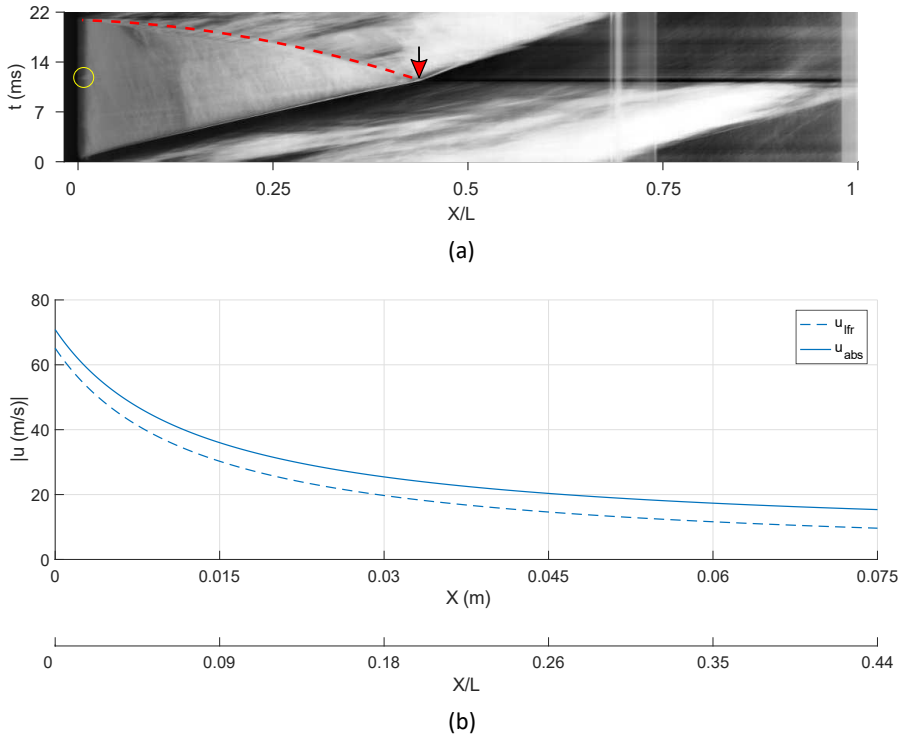


Figure 2.15: Pressure wave path with corresponding velocities. In (a) an x-t diagram of the shedding cycle from Fig. 2.14 is shown. The velocity profiles of the pressure wave as the function of position are shown in (b). The blue dashed line is the velocity in the laboratory frame of reference. The blue continuous line gives the absolute velocity based on the cavity growth rate. Note the difference in horizontal axis scale between the top and bottom figure.

x-t diagram is shown for an experiment with $\sigma = 0.88$ ($u_0 = 14.2$ m/s, $f = 101.1$ Hz and $p = 90$ kPa), and is presented in Fig. 2.16. In this x-t diagram two different regimes can be identified, with a transition at $t \approx 34$ and $t \approx 66$ ms. For $0 < t < 34$ ms and $66 < t < 87.5$ ms emitted pressure waves can be observed, emanating from collapsing cavities. Although the pressure waves are not so evident as in the case of Fig. 2.13, they can still be identified as the trigger mechanism of (growing) cavity detachment. For $34 < t < 66$ ms, the pattern changes and the characteristics of stick-slip behavior can be observed. This analysis shows that in the intermediate region indeed two alternating mechanisms can be observed.

2.5. DISCUSSION

This study has analyzed the mechanisms responsible for partial cavitation in a venturi based on the cavitation number. The cavity lengths and time scales of the re-entrant jet mechanism are smaller than the bubbly shock mechanism, as shown in Fig. 2.8 and Fig. 2.9, respectively. The x-t diagram of an intermediate region (Fig. 2.16) clearly dis-

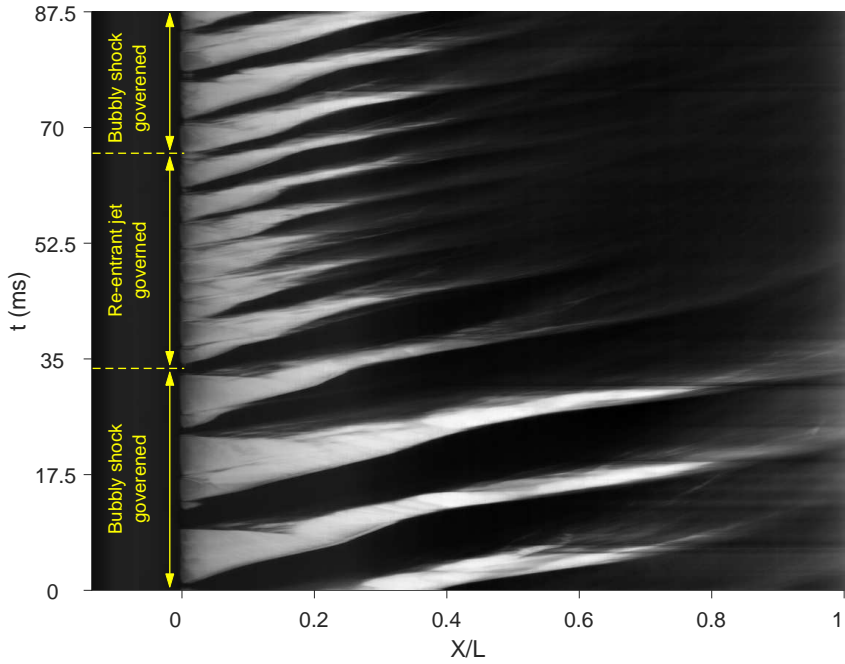


Figure 2.16: X-t diagram of an experiment in the intermediate region. The light gray regions indicate the presence of vapor and the black regions indicate the presence of liquid. Bubbly shock induced shedding can be observed for $0 < t < 34$ ms and $66 < t < 87.5$ ms. Re-entrant jet governed shedding can be observed for $34 < t < 66$ ms. For this case, $\sigma = 0.88$ ($u_0 = 14.2$ m/s, $f = 101.1$ Hz and $p = 90$ kPa).

tinguishes between both mechanisms based on the above-mentioned parameters. This implies that there is a critical point when the bubbly shock mechanism takes over the re-entrant jet mechanism. From a close investigation of high-speed movies, we found that the bubbly shock mechanism takes over when a certain minimum amount of vapor cloud collapses downstream of venturi to emit a pressure wave strong enough to detach the growing cavity. Large vapor clouds are formed in the bubbly shock mechanism, because of larger cavity lengths at lower cavitation numbers (see Fig. 2.7), as a result they emit stronger pressure waves. Several vapor cloud collapses (horizontal black lines) can be seen in a shedding cycle in the bubbly shock mechanism as shown in Fig. 2.13, the pressure wave emitted from the largest vapor cloud collapse causes the shedding (detachment of the growing cavity). This strong pressure wave causes a jump in the density due to condensation while it propagates through the bubbly water and the cavity, so it can be described as a shock wave. The collapses of individual bubbles and small groups initiate further collapses, and this cascade process results in the shock wave. Smaller vapor cloud collapses are also evident in the re-entrant jet mechanism (Fig. 2.11) but when the pressure waves are extrapolated upstream of the venturi in the x-t diagrams, it is found that they do not cause the detachment of the growing cavity.

Neither the re-entrant jet mechanism, nor the bubbly shock mechanisms was found to be dominant in the transition region. However, a low-frequency component was found in a spectral analysis (at around 10 Hz). This frequency is caused by switching between both the modes i.e. from the re-entrant jet mechanism to the bubbly shock mechanism and vice versa. This frequency is found to be a function of the static pressure of the system, as it decreases with a decrease in static pressure of the system. In order to ensure that it was not due to the pump, a system frequency analysis was performed. The system was operated for 6 minutes and it was concluded that no frequency component was captured in the frequency range which was in the region of interest. The decrease in this frequency causes spreading in the transition region as shown in Fig. 2.9 and Fig. 2.10.

The dissolved gas concentration can affect the inception of cavitation and mean cavity length, which in turn changes the parameters for the dynamics of cavity deformation. Although the water was degassed before the experiments to approximately 40% oxygen content, still the experiments performed below the ambient pressure at 0.5 bar absolute had an oxygen content of 32% due to unavoidable degassing during experiments.

The shock wave path was tracked through the *cavity*, but there is also a *core* that consists of liquid. Our analysis is based on a single shock wave velocity. The radial variation in vapor fraction will result in different local pressure wave velocities. The speed of sound in the liquid core is of the same order of magnitude as in the liquid region downstream. If the black shock wave path in Fig. 2.15(a) is extrapolated through the cavity, a white plume (encircled with yellow color) is observed at the throat of venturi ($t \approx 11$ ms). This plume is possibly caused by the shock wave, which traveled through the liquid core region instead of traveling through the cavity.

Accurate determination of the velocity of the shock wave in the liquid region (right side of sub-panels in Fig. 2.14) was more difficult due to its high velocity. A video was recorded at 125 kHz[‡] at $\sigma = 0.4$, the best-approximated shock wave velocity in the liquid phase was found to be 900 m/s by using an x-t diagram (Fig. 2.17). The shock wave propagation speed is not the expected 1450 m/s in the liquid phase, because it is not a pure liquid (water). Vapor left from the shedded cavity (Fig. 2.14(d)) and the presence of non-condensable gas, even a small amount, significantly lowers the speed of sound. A speed of sound of 900 m/s would correspond to a gas fraction of approximately 0.004% (calculated using the model of Minnaert (1933)). In contrast, a velocity of 15 m/s was found in the cavity region. This decrease in velocity can be explained by the difference in the speed of sound in both phases. With a static pressure of 40 kPa and the estimated velocity, an approximate void fraction of 35% was found at the cavity front. With the increase of velocity in the cavity (Fig. 2.15(b)) towards the venturi throat, the vapor fraction also increases. The quantitative usefulness of the experiments for the shock wave velocity, including the change in shock wave velocity, should be further evaluated against quantitative void fractions to compare the speed of sound both in the liquid phase and the vapor phase.

2.6. CONCLUSIONS AND OUTLOOK

The purpose of the current study was to investigate the different cavitation regimes in a converging-diverging axisymmetric nozzle. The different cavitation regimes are generated

[‡]The high-speed video has an exposure time of 1/125 kHz.

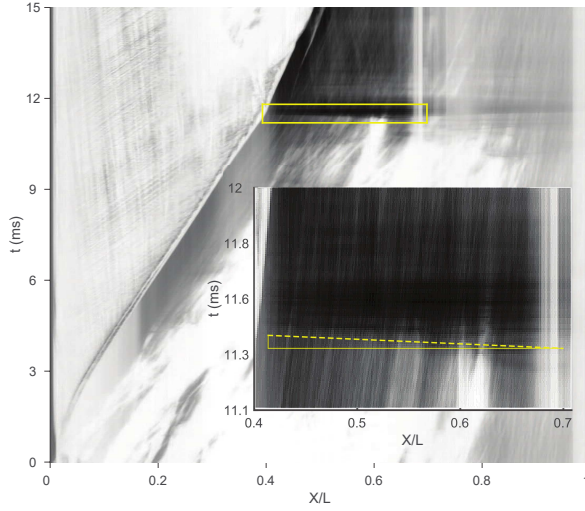


Figure 2.17: X-t diagram with an enlarged shock wave path in the liquid phase. The yellow dashed line in the inset gives the best approximation of the shock wave path, corresponding to a velocity of 900 m/s. For this case, $\sigma = 0.40$ ($u_0 = 13.7$ m/s, $f = 46.1$ Hz and $p = 40$ kPa) and $F_s = 125$ kHz.

by systematically changing the global static pressure and flow velocity. From this study, the following conclusions are formulated:

For a cavitation number based on global static pressure, the pressure loss coefficient is found to be a function of cavitation number only. Flow blockage is increasing for decreasing cavitation number. For the same definition of the cavitation number, cavity length and time scales are also a function of cavitation number. Both scales are combined in the Strouhal number, based on the cavity lengths at the time instant of detachment. This St_l is the dimensionless form of the integral cavity growth velocity. It follows that for this Strouhal number, as a function of cavitation number, a minimum is found for a cavitation number $\sigma = 0.88$.

Based on the result, and the cavitation dynamics in the x-t diagrams, three different cloud cavitation shedding regimes can be identified. It is found that for $\sigma > 0.95$, the periodic cavity shedding is caused by the re-entrant jet mechanism. The shedding caused by re-entrant jet mechanism is characterized by stick-slip behavior in the x-t diagram. For $\sigma < 0.75$, the prevalent mechanism for periodic cavity shedding is found to be the bubbly shock mechanism. Both mechanisms are encountered in the intermediate region, $0.75 < \sigma < 0.95$. From a physical point of view, both mechanisms are very different. The re-entrant jet mechanism is caused by an adverse pressure gradient and a stagnation point at the closure of the cavity. The bubbly shock in the growing cavity is caused by a shock wave, which is emitted from the previously detached, advected and collapsing cavity. This makes this mechanism a shock-wave driven phenomenon. The shock wave velocity, as a function of position, is determined from the shock wave path in the x-t diagram. The shock wave velocity in the liquid phase was found to be 900 m/s and around 15 m/s in the cavity region.

The collected data is currently being used for validation of numerical codes. X-ray densitometry experiments are also being performed to extract quantitative information regarding the local void fractions. X-ray experiments will also help us in reconstructing the 3D shape of the cavity.

REFERENCES

- Arndt, R. E., Song, C., Kjeldsen, M., He, J., and Keller, A. (2000). Instability of partial cavitation: a numerical/experimental approach. In *Proceedings of 23rd Symposium on Naval Hydrodynamics, Val deReuil, France, 17–22 Sept.*
- Avellan, F., Dupont, P., and Farhat, M. (1991). Cavitation erosion power. In *1st ASME-JSME Fluids Engineering Conference, Portland, OR, 23-27 June.*
- Balas, G. J., Bokor, J., Vanek, B., and Arndt, R. E. (2006). Control of High-Speed Underwater Vehicles. In *Control of Uncertain Systems: Modelling, Approximation, and Design*, pages 25–44. Springer.
- Bensow, R. E. (2011). Simulation of the unsteady cavitation on the Delft Twist11 foil using RANS, DES and LES. In *Proceedings of the 2nd International Symposium on Marine Propulsors, Hamburg, Germany.*
- Budich, B., Schmidt, S., and Adams, N. (2018). Numerical simulation and analysis of condensation shocks in cavitating flow. *Journal of Fluid Mechanics*, 838:759–813.
- Callenaere, M., Franc, J.-P., Michel, J.-M., and Riondet, M. (2001). The cavitation instability induced by the development of a re-entrant jet. *Journal of Fluid Mechanics*, 444:223–256.
- Charrière, B. and Goncalves, E. (2017). Numerical investigation of periodic cavitation shedding in a venturi. *International Journal of Heat and Fluid Flow*, 64:41–54.
- Chen, G., Wang, G., Hu, C., Huang, B., Gao, Y., and Zhang, M. (2015). Combined experimental and computational investigation of cavitation evolution and excited pressure fluctuation in a convergent-divergent channel. *International Journal of Multiphase Flow*, 72:133–140.
- Croci, K., Tomov, P., Ravelet, F., Danlos, A., Khelladi, S., and Robinet, J.-C. (2016). Investigation of Two Mechanisms Governing Cloud Cavitation Shedding: Experimental Study and Numerical Highlight. In *ASME 2016 International Mechanical Engineering Congress & Exposition IMECE 2016.*
- Danlos, A., Ravelet, F., Coutier-Delgosha, O., and Bakir, F. (2014). Cavitation regime detection through Proper Orthogonal Decomposition: Dynamics analysis of the sheet cavity on a grooved convergent–divergent nozzle. *International Journal of Heat and Fluid Flow*, 47:9–20.
- De Lange, D. and De Bruin, G. (1997). Sheet Cavitation and Cloud Cavitation, Re-Entrant Jet and Three-Dimensionality. *Applied Scientific Research*, 58(1):91–114.

- 2
- Decaix, J. and Goncalves, E. (2013). Investigation of three-dimensional effects on a cavitating venturi flow. *International Journal of Heat and Fluid Flow*, 44:576–595.
- Dular, M., Khelifa, I., Fuzier, S., Maiga, M. A., and Coutier-Delgosha, O. (2012). Scale effect on unsteady cloud cavitation. *Experiments in Fluids*, 53(5):1233–1250.
- Foeth, E.-J., van Terwisga, T., and van Doorne, C. (2008). On the collapse structure of an attached cavity on a three-dimensional hydrofoil. *Journal of Fluids Engineering*, 130(7):071303.
- Frikha, S., Coutier-Delgosha, O., and Astolfi, J. A. (2008). Influence of the Cavitation Model on the Simulation of Cloud Cavitation on 2D Foil Section. *International Journal of Rotating Machinery*, vol.2008.
- Ganesh, H. (2015). Bubbly Shock Propagation as a Cause of Sheet to Cloud Transition of Partial Cavitation and Stationary Cavitation Bubbles Forming on a Delta Wing Vortex. PhD thesis, The University of Michigan.
- Ganesh, H., Mäkiharju, S. A., and Ceccio, S. L. (2016). Bubbly shock propagation as a mechanism for sheet-to-cloud transition of partial cavities. *Journal of Fluid Mechanics*, 802:37–78.
- Gnanaskandan, A. and Mahesh, K. (2016). Large Eddy Simulation of the transition from sheet to cloud cavitation over a wedge. *International Journal of Multiphase Flow*, 83:86–102.
- Habchi, C., Gillet, N., Velghe, A., Bohbot, J., Schmid, A., Von Rotz, B., and Herrmann, K. (2014). On the role of cavitation in marine large diesel injector: numerical investigation of nozzle orifices eccentricity. In *Annual Conference on Liquid Atomization and Spray Systems, Bremen, Germany*.
- Hayashi, S. and Sato, K. (2014). Unsteady Behavior of Cavitating Waterjet in an Axisymmetric Convergent-Divergent Nozzle: High Speed Observation and Image Analysis Based on Frame Difference Method. *Journal of Flow Control, Measurement & Visualization*, 2:94–104.
- Hogendoorn, W. (2017). Cavitation: Experimental investigation of cavitation regimes in a converging-diverging nozzle. *Master's thesis, Delft University of Technology*.
- Idelchik, I. E. and Fried, E. (1986). *Handbook of hydraulic resistance: Second edition*. Hemisphere Publishing, New York, NY, 2nd edition.
- Jahangir, S., Hogendoorn, W., and Poelma, C. (2018). Dynamics of partial cavitation in an axisymmetric converging-diverging nozzle. *International Journal of Multiphase Flow*, 106:34 – 45.
- Jakobsen, J. (1964). On the Mechanism of Head Breakdown in Cavitating Inducers. *Journal of Basic Engineering*, 86(2):291–305.

- Jana, J., Milada, K., Daniel, H., and Michal, W. (2016). Methods of experimental investigation of cavitation in a convergent-divergent nozzle of rectangular cross section. *Measurement Science Review*, 16(4):197–204.
- Ji, B., Luo, X., Wu, Y., Peng, X., and Duan, Y. (2013). Numerical analysis of unsteady cavitating turbulent flow and shedding horse-shoe vortex structure around a twisted hydrofoil. *International Journal of Multiphase Flow*, 51:33–43.
- Kawanami, Y., Kato, H., Yamaguchi, H., Tanimura, M., and Tagaya, Y. (1997). Mechanism and control of cloud cavitation. *Journal of Fluids Engineering*, 119(4):788–794.
- Knapp, R. T. (1955). Recent investigations of the mechanics of cavitation and cavitation damage. *Transactions of the ASME*, 77:1045–1054.
- Kubota, A., Kato, H., Yamaguchi, H., and Maeda, M. (1989). Unsteady Structure Measurement of Cloud Cavitation on a Foil Section Using Conditional Sampling Technique. *Journal of Fluids Engineering*, 111(2):204–210.
- Long, X., Cheng, H., Ji, B., Arndt, R. E., and Peng, X. (2018). Large eddy simulation and Euler–Lagrangian coupling investigation of the transient cavitating turbulent flow around a twisted hydrofoil. *International Journal of Multiphase Flow*, 100:41–56.
- Long, X., Zhang, J., Wang, J., Xu, M., Lyu, Q., and Ji, B. (2017). Experimental investigation of the global cavitation dynamic behavior in a venturi tube with special emphasis on the cavity length variation. *International Journal of Multiphase Flow*, 89:290–298.
- Minnaert, M. (1933). On musical air-bubbles and the sounds of running water. *The London, Edinburgh, and Dublin Philosophical Magazine and Journal of Science*, 16(104):235–248.
- Nikuradse, J. (1932). Gesetzmäßigkeiten der turbulenten Strömung in glatten Röhren. *Forschungsheft 356. Beilage zu, Ausgabe B, Bd. 3, Berlin*, page 1.
- Peng, X., Ji, B., Cao, Y., Xu, L., Zhang, G., Luo, X., and Long, X. (2016). Combined experimental observation and numerical simulation of the cloud cavitation with U-type flow structures on hydrofoils. *International Journal of Multiphase Flow*, 79:10–22.
- Pham, T., Larrarte, F., and Fruman, D. (1999). Investigation of Unsteady Sheet Cavitation and Cloud Cavitation Mechanisms. *Journal of Fluids Engineering*, 121(2):289–296.
- Reisman, G., Wang, Y.-C., and Brennen, C. E. (1998). Observations of shock waves in cloud cavitation. *Journal of Fluid Mechanics*, 355:255–283.
- Rudolf, P., Hudec, M., Gríger, M., and Štefan, D. (2014). Characterization of the cavitating flow in converging-diverging nozzle based on experimental investigations. In *EPJ Web of Conferences*, volume 67. EDP Sciences.
- Saito, Y. and Sato, K. (2007). Bubble collapse propagation and pressure wave at periodic cloud cavitation. In *Proceedings of 6th International Conference on Multiphase Flow, ICMF 2007*.

- Stanley, C., Barber, T., and Rosengarten, G. (2014). Re-entrant jet mechanism for periodic cavitation shedding in a cylindrical orifice. *International Journal of Heat and Fluid Flow*, 50:169–176.
- Stutz, B. and Reboud, J. (1997). Experiments on unsteady cavitation. *Experiments in Fluids*, 22(3):191–198.
- Timoshevskiy, M. V., Churkin, S. A., Kravtsova, A. Y., Pervunin, K. S., Markovich, D. M., and Hanjalić, K. (2016). Cavitating flow around a scaled-down model of guide vanes of a high-pressure turbine. *International Journal of Multiphase Flow*, 78:75–87.
- Tomov, P., Khelladi, S., Ravelet, F., Sarraf, C., Bakir, F., and Vertenoeuil, P. (2016). Experimental study of aerated cavitation in a horizontal venturi nozzle. *Experimental Thermal and Fluid Science*, 70:85–95.
- Van Terwisga, T., Fitzsimmons, P., Li, Z.-r., and Foeth, E. J. (2009). Cavitation erosion—a review of physical mechanisms and erosion risk models. *Proc. 7th Int. Sym. Cavitation, CAV2009, Ann Arbor, MI*.
- Wang, C., Huang, B., Wang, G., Zhang, M., and Ding, N. (2017). Unsteady pressure fluctuation characteristics in the process of breakup and shedding of sheet/cloud cavitation. *International Journal of Heat and Mass Transfer*, 114:769–785.
- White, F. M. (2003). *Fluid Mechanics*. McGraw-hill, 7th edition.
- Wu, X., Maheux, E., and Chahine, G. L. (2017). An experimental study of sheet to cloud cavitation. *Experimental Thermal and Fluid Science*, 83:129–140.

3

DIRECT COMPARISON OF SHADOWGRAPHY AND X-RAY IMAGING FOR VOID FRACTION DETERMINATION

This chapter is adopted from: A. Dash, S. Jahangir, C. Poelma, *Direct comparison of shadowgraphy and x-ray imaging for void fraction determination*, Measurement Science and Technology **29**(12), 125303 (2018).

3.1. INTRODUCTION

There are many industrial applications involving multiphase flows, including sprays, fluidized beds, bubbly flows and cavitating flows. A common characteristic of these flows is that they are often optically opaque. This is due to multiple scattering of visible light by particles/bubbles in its path. More often than not, simple optical techniques are limited to analyzing phenomena occurring close to the wall region. Owing to the lack of penetrability of visible light in such optically opaque flows, alternative techniques have been developed to quantitatively characterize the phenomena occurring in the interior of the flow (Nadeem and Heindel, 2018; Van Ommen and Mudde, 2008). X-ray computed tomography (CT) is an appropriate choice for an accurate analysis of the internal structure of the flow, as it is able to provide detailed information on the spatial distribution of void fractions (Khlifa et al., 2017; Wang et al., 2018b). However, a major disadvantage of this technique is the high barrier to entry. Of the multiphase flows introduced earlier, cavitating flows are slightly different, as a predetermined global void fraction of a certain phase cannot be introduced into the flow. This is due to the phenomenon of cavitation, where liquid vaporizes upon reaching a pressure below its vapor pressure. Void fraction is a major quantity of interest in cavitating flows as it can be used to demarcate the distinct shedding mechanisms (Ganesh et al., 2016; Gnanaskandan and Mahesh, 2016).

For certain regimes of multiphase flows, such as stratified flows or slug flows, void fractions can be determined by applying a simple pixel counting or grayscale intensity based technique onto shadowgraphy images. For instance, in some studies (Ursenbacher et al., 2004; Wojtan et al., 2004, 2005), a plane perpendicular to the flow direction (i.e. a cross-section of the pipe) was illuminated and imaged. The void fractions were then evaluated based on a pixel counting technique. Alternatively, the center-plane could be used. However, this would rely on an assumption about the three-dimensional structure of the flow (for example an axisymmetric structure of the slug). Such grayscale intensity based techniques may not always be appropriate to other regimes such as dispersed flows or annular flows. Nevertheless, various studies exist where the above pixel counting and/or grayscale intensity based techniques have been employed to determine void fractions, in flow regimes where it may not be perfectly applicable (Dunn et al., 2010; Kowalski et al., 2018; Leandro et al., 2014, 2012; Perpar et al., 2014; Puli and Rajvanshi, 2012; Rana et al., 2014; Wang et al., 2018a; Wosnik and Arndt, 2013). In the above cases, the flow characteristics are often assumed to be two-dimensional or the void fractions are estimated from instantaneous images. This approach is understandable, due to the limited access to more advanced measurement facilities like X-ray CT.

Due to the continued usage of shadowgraphy for optically dense systems, even for void fraction estimation, questions persist over its applicability to such systems. The lack of applicability of shadowgraphy for cavitating flows has been qualitatively demonstrated by comparing images obtained by simple shadowgraphy/photography and CT (Bauer et al., 2012; Lorenzi et al., 2017; Mitroglou et al., 2016). Mitroglou et al. (2016) have reported a good qualitative correspondence between the vapor cloud *shapes* identified via time-averaged intensities of shadowgraphy images and line-integrated projections of three-dimensional CT data. Lorenzi et al. (2017) too have compared time-averaged results obtained via the two imaging modalities and have concluded that planar shadowgraphy can create a false impression of the cavitation structures in the third dimension. These

qualitative results Lorenzi et al. (2017); Mitroglou et al. (2016) already act as a deterrent for researchers aiming to extract void fractions through shadowgraphy like techniques. However, there has not been a *quantitative* comparison between images obtained by these two modalities (shadowgraphy and X-ray imaging), to the best of the authors' knowledge. A quantitative analysis could shed further light onto this matter.

The current study is thus concerned with a quantitative comparison between the time-averaged images of a three-dimensional cavitating flow in an axisymmetric converging-diverging nozzle ('venturi'), recorded by two different imaging modalities: Shadowgraphy and X-ray imaging. A venturi has been selected as a test case for the present study, owing to the complex nature of the flow through it. Thus, distinct flow regimes suitable for the current comparative analysis are present. The grayscale intensities in these images are a function of the void fractions occurring in the flow as well as the working mechanisms of the techniques. X-ray imaging, being the more reliable technique for void fraction estimation (owing to its penetrability in optically dense media), is then used to adjudge the fidelity of void fraction estimation (either qualitative or quantitative) via shadowgraphy in three-dimensional cavitating flows. Regimes where (qualitative) void fraction estimation from shadowgraphy may still be applicable are also identified.

The remainder of the chapter is structured as follows: Details of the experimental setups as well as the image processing steps to make images from the two modalities comparable are available in Section 3.2. In Section 3.3, a quantitative comparison between the grayscale intensities, obtained from the two measurement techniques is performed. The results are discussed in further depth in Section 3.4, which includes the delimitation of regimes where shadowgraphy may still provide a legitimate interpretation of void fractions in three-dimensional cavitating flows. Finally, the major findings of this study are summarized in Section 3.5.

3.2. METHODOLOGY

Details of the experimental setups for both techniques, image acquisition and image processing are described in this section. The quality of the imaging techniques is also evaluated. This is especially necessary for the X-ray images as they are later used as the yardstick while judging the shadowgraphs.

3.2.1. SETUP

The schematic of the flow setup utilized for the experiments is illustrated in Fig. 3.1. The flow is driven by a centrifugal pump, while a combination of a water column and a vacuum pump is used to control the global static pressure of the flow loop. Further details are available in Jahangir et al. (2018). The venturi, with a throat diameter (D_0) of 16.67 mm, is milled out from a rectangular block of polymethylmethacrylate (PMMA) and polished. This is done to minimize image distortion inside the venturi. A schematic of the venturi cross-section is shown in Fig. 3.1 (inset).

The intensity of cavitation is often described by the 'Cavitation number' ($\sigma = \frac{p - p_v}{\frac{1}{2} \rho u_0^2}$). Here, p is the pressure at a reference position (the pressure recovery section in the current study), p_v is the vapor pressure of the fluid (calculated at the measured temperature), ρ is the density of the fluid, and u_0 is the reference velocity (the velocity at the venturi

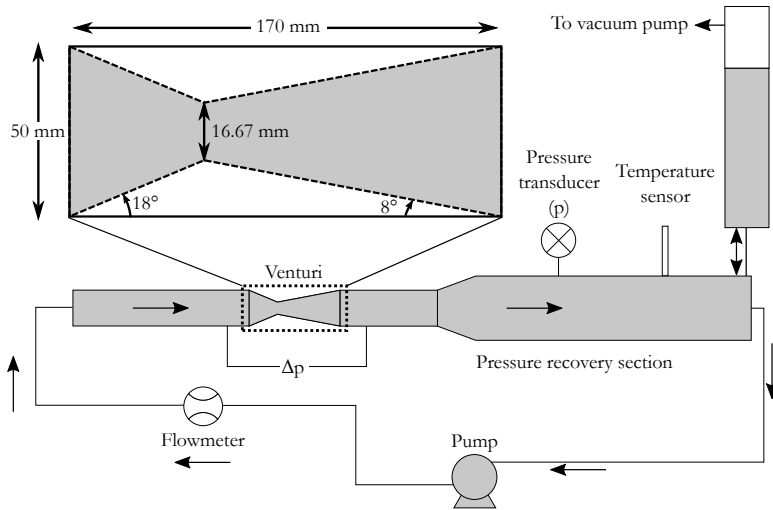


Figure 3.1: The flow setup deployed for the shadowgraphy measurements. Shown in the inset is a detailed version of the venturi. For the X-ray measurements, the major components of the setup were turned 90° in the counter-clockwise direction due to space limitations. Objects in this schematic are not drawn to scale.

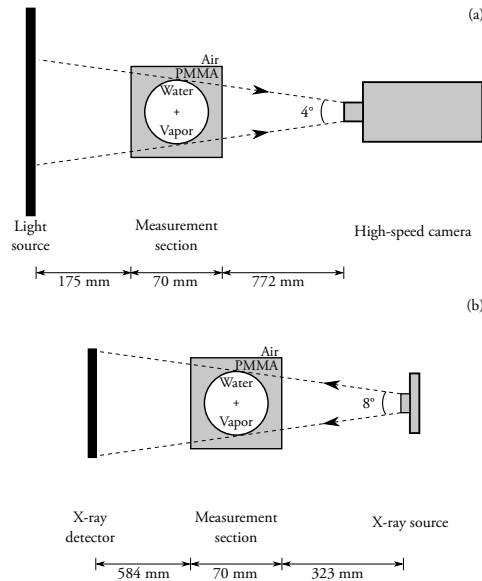


Figure 3.2: Imaging of the flow was done via two imaging modalities. Shown here are their respective schematics. (a) Shadowgraphy (b) X-ray imaging. Objects and viewing angles are not drawn to scale. The angles approximate the span covered by the venturi.

throat in the current study). In the current study, cavitation occurs only when the cavitation number is below unity. Moreover, the lower the cavitation number, the higher the

cavitation intensity.

Shadowgraphs were recorded at 800 Hz for 4 seconds by a Photron Fastcam APX RS, in combination with a 105mm/2.8 FX AF MICRO-NIKKOR object-glass. The CMOS sensor had a bit depth of 10. The camera was operated at a $f_{\#}$ of 2.8 with an exposure time of 111 μ s. Images with a resolution of 1024×336 pixels were recorded, resulting in a spatial resolution of approximately 0.15 mm. A LED panel was used for a uniform back-illumination. For the X-ray measurements, a source-detector pair was used to measure the attenuation of the X-rays passing through the cavitating flow. The source, Yxlon Y.TU 160-D06, was operated at 120 keV and 5 mA in order to achieve a high contrast between the cavities and the liquid. The flat detector, Xineos-3131 CMOS model, consists of a 307 mm \times 302 mm sensitive area with a 1548×660 pixel array. Each pixel has a size of $198 \mu\text{m} \times 198 \mu\text{m}$ with 14 bits of pixel depth, resulting in a spatial resolution of about 0.07 mm in the imaging plane. Images were recorded at 60 Hz over 60 seconds. Schematics of the measurement setup are illustrated in Fig. 3.2.

The experimental setup shown in Fig. 3.1 was reoriented for the X-ray imaging measurements due to space constraints. Nevertheless, the flows from the two experiments at the same cavitation number were confirmed to be equivalent, as the pressure drops across the venturi (Δp) were nearly identical for both cases. Visual inspection also confirmed symmetry of the top and bottom halves of the time-averaged shadowgraphs (for example, see Fig. 3.5(d)), suggesting little influence of gravity.

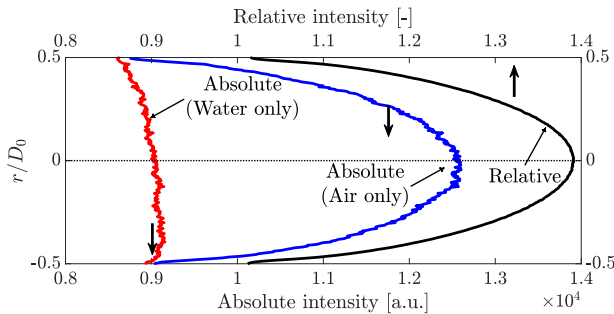


Figure 3.3: Profiles of the absolute and relative intensities recorded on the X-ray detectors at the streamwise location of the venturi throat. The two cases considered are when the venturi contains solely air and solely water.

3.2.2. QUALITY OF THE IMAGING MODALITIES

Firstly, the intensities were measured by the X-ray detector when the venturi contained only air and only water. Air is a suitable alternative for water vapor as they have similar mass densities, and thus similar absorption coefficients. Fig. 3.3 shows the absolute intensities of air and water. The venturi was left empty for air while it was completely filled with filtered water for the latter. At the streamwise plane of the throat, the maximum intensity was recorded as 12580 for air while it was 9045 for water, as can be seen in Fig. 3.3. Thus, approximately 21% of the total capacity of the 14-bit detector was utilized

here. However, this range would increase in the downstream direction with the increasing diameter of the venturi cross-section. A relative intensity profile is obtained by dividing the absolute intensities of air and water, shown in Fig. 3.3, which is in accordance with the shape of the venturi (air occupies a higher fraction of the X-ray path length closer to the center of the venturi). Moreover, the wiggles visible prominently in the absolute intensity curves are drastically compressed in the relative intensity curves. This confirms that the wiggles in the absolute intensities are a result of the differences in individual X-ray detector element sensitivities and not random noise.

3

3700 X-ray images were utilized for the cavitating flow measurements. In order to ensure that the quantity of images was sufficient, a convergence study was performed on the images of the cavitating flow whose results are shown in Fig. 3.4. The term on the y-axis is computed as follows. After each 100 images, a new time-averaged image is computed, say I_{new} , is then compared with the old time-averaged image (i.e. without the new 100 images), say I_{old} . The term on the y-axis is then mean of all values in the matrix $|(I_{new} - I_{old})/I_{old}|$. It is seen that after 3700 images, the relative error reduces to less than 3%, implying sufficient convergence. A similar analysis for the shadowgraphy images is performed, which too shows a satisfactory convergence behaviour. The quicker convergence of the shadowgraphy images may be attributed to the better signal to noise ratio.

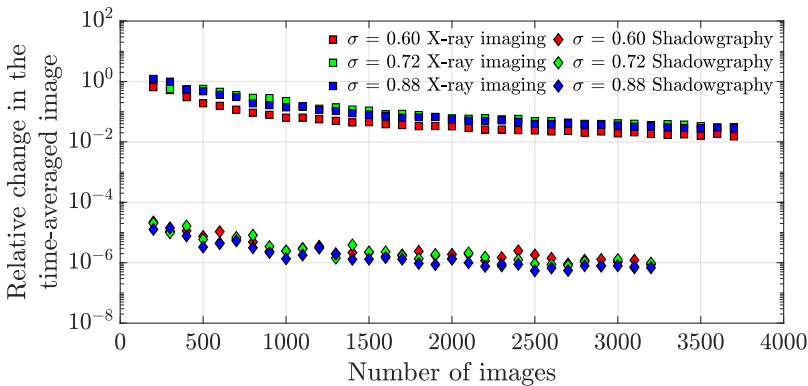


Figure 3.4: Sufficient convergence is obtained for the time-averaged grayscale images via X-ray imaging as well as shadowgraphy.

3.2.3. DATA PROCESSING

Images acquired by the two techniques have several differences, including the aspect ratio, spatial resolution, field of view, lines-of-sight and grayscale intensities. Therefore, a few preprocessing steps were needed before comparing the two types of images. All of the following steps were performed using Matlab R2016b (The Mathworks Inc., Natick, USA). The process is illustrated in Fig. 3.5, and the bulk flow is from left to right in each of these images.

In order to reduce the effect of the system on the image analysis, a background sub-

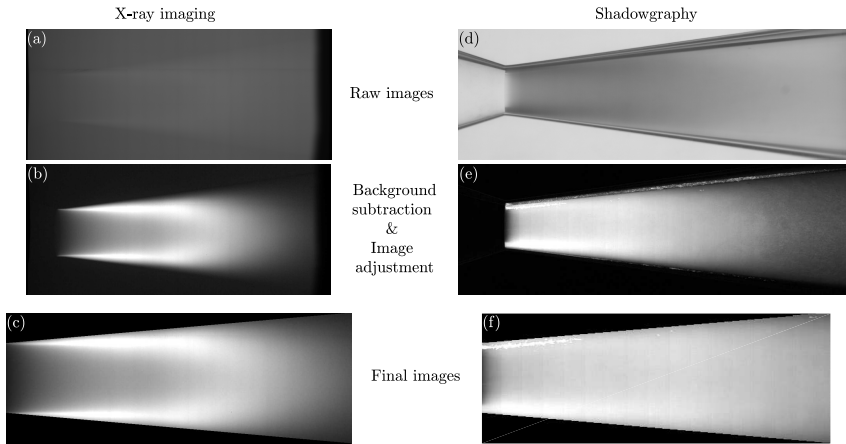


Figure 3.5: Images from the two measurement techniques were preprocessed in order to make them comparable. (a)-(c) correspond to images from the X-ray imaging technique while (d)-(f) are the corresponding steps for shadowgraphy images. (a),(d) are the raw time-averaged images. (b),(e) are the images obtained following a background subtraction as well as being adjusted to improve contrast. (c),(f) are the images obtained after the region of interest is cropped out. Images (c) and (f) are then mapped onto an identical coordinate space in order to compare the grayscale intensities from the two techniques. In all these images, the bulk flow occurs from the left to the right.

traction was performed first. For the X-ray technique, images of the non-cavitating flows (i.e. vapor absent) were available. However, no such images were available for the shadowgraphy experiments. Thus, artificial background images were generated for the shadowgraphy technique as follows. Each pixel in the background image is assigned with the maximum grayscale value (in shadowgraphy, the liquid phase appeared white) measured at that pixel location over the course of the entire measurement (multiple cavitation cycles). This method also leads to the generation of a few thin artifacts (for example, near the top wall in Fig. 3.5(e)-(f)). However, these are not expected to significantly affect the results and conclusions of this study.

In the X-ray images, the vapor phase has higher grayscale intensities while the liquid phase had lower ones. This happens because the presence of vapor leads to lower attenuation of the X-rays along its path length. On the other hand, the shadowgraphy images have lower grayscale intensities for the vapor phase and vice versa. This occurs as the bubbles generated by cavitation block the visible light emanating from the LED panel. Thus, for the X-ray images, the background is subtracted from the raw time-averaged images while for the shadowgraphy images, the raw time-averaged image is subtracted from the background. This way, the lower grayscale intensities represent the liquid phase in both sets of background-subtracted images.

While the shadowgraphs display a clear contrast between the two phases (via the grayscale intensities), the contrast is visibly reduced for the X-ray images (Fig. 3.5(a)), due to the higher background grayscale intensities. For example, in Fig. 3.3, the background has approximately 9000 counts. When the venturi is emptied, the measured intensity is approximately 12500 counts. The maximum contrast at the throat is thus approximately

40% of the background signal. However, in the actual experiments, the void fractions seldom reach close to 100%, and the recorded signals are closer to the bottom portion of the 40% range. While this range may be improved by operating the X-ray source at a higher power, it would lead to saturation of the CMOS sensor. Thus, an image adjustment operation (i.e. rescaling the grayscale intensities in order to have 1% of the values being saturated at low and high intensities) is performed on both sets of images, which effectively normalizes the grayscale intensities. With this operation, the values of the grayscale intensities then vary between 0 and 1 in both cases.

The next step involves the cropping of images to restrict the analysis to a certain region of interest. The center of the venturi throat is selected as the origin for the current analysis with a length of five throat diameters ($5D_0$, where D_0 is the throat diameter) used in the streamwise direction. Furthermore, the diameter of the region of interest in the radial direction increased with respect to the throat diameter with a divergence angle of 5° along the downstream direction, which is lower than the venturi divergence angle of 8° . This is done so in order to avoid analysis in the upper and lower wall regions, which might be susceptible to errors via optical distortion, especially in shadowgraphy, despite a close match in refractive indices.

Since the images from the two experiments possess different resolutions, it is desirable to ultimately map the grayscale intensities from the two measurement techniques onto the same pixel coordinates. The throat diameter is used as a reference length scale to adjudge the goodness of the overlap between the coordinate systems. In the current analysis, information from the shadowgraphy images (lower spatial resolution) is interpolated onto pixel coordinates of the X-ray images (higher spatial resolution) via linear interpolation. The original disparity between the image resolutions (Fig. 3.5(a)-(b)) is dispensed with (Fig. 3.5(e)-(f)). Thus, images from the two techniques can now be compared on a pixel-by-pixel basis.

3.3. RESULTS

Grayscale intensities from both techniques are rendered comparable after the processing of images per the procedure in Section 3.2.3. The comparison here is primarily restricted only to the regions located near the line of symmetry, along the streamwise direction. This is done so in order to avoid artifacts that may arise due to the stronger curvature of the pipe away from the line of symmetry, especially in the shadowgraphy images. Moreover, this minimizes any effects that may arise due to the minor difference in the viewing angles between the two methods.

Three different cavitation numbers are considered for comparison in the current study: 0.60, 0.72 and 0.88, whose results are illustrated in Fig. 3.6, Fig. 3.7 and Fig. 3.8, respectively. This was done as each cavitation number had different vapor distributions (Jahangir et al., 2018). For each case, the time-averaged grayscale intensity image from both the techniques are shown, with the regions of interest overlaid on them. It can be seen that there is a similarity in a qualitative sense (for example, the streamwise location beyond which the grayscale intensity is monotonically decreasing). However, there are much sharper structures visible in the X-ray images as compared to the shadowgraphy ones, owing to the former's ability in penetrating the multiple media. Thus, it is expected that the grayscale intensities from the two modalities will not behave in a coherent

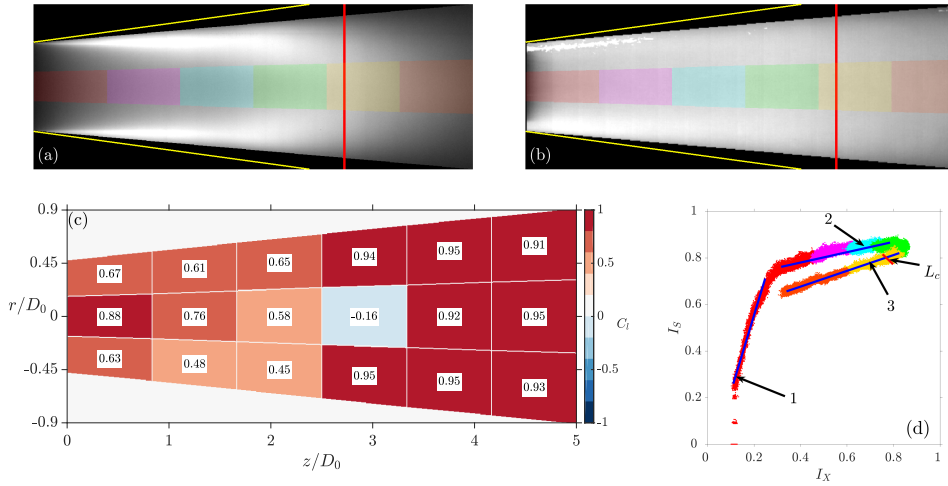


Figure 3.6: A comparison of the grayscale intensities at identical coordinates along the streamwise direction, from the two measurement techniques. Here, $\sigma = 0.60$. (a) Time averaged X-ray image with the regions of interest superimposed in different colours, (b) Time averaged shadowgraphy image with the regions of interest superimosed in different colours, (c) Local correlation coefficients at the different zones, (d) The colour-coded zonal scatter plots. The colours in this scatter plot correspond with the respective coloured regions of interest demarcated in (a) and (b). The vertical red lines in (a) and (b) denote the streamwise location of the estimated cavity length. The red line in (d) is the approximate location of the estimated cavity length along the loop-like trajectory in the scatter plot, while the blue lines in (d), labeled from 1-3, identify the different regimes. In (a) and (b), darker regions represent the liquid phase while the lighter regions represent the vapor phase. The yellow lines in (a) and (b) denote the venturi walls.

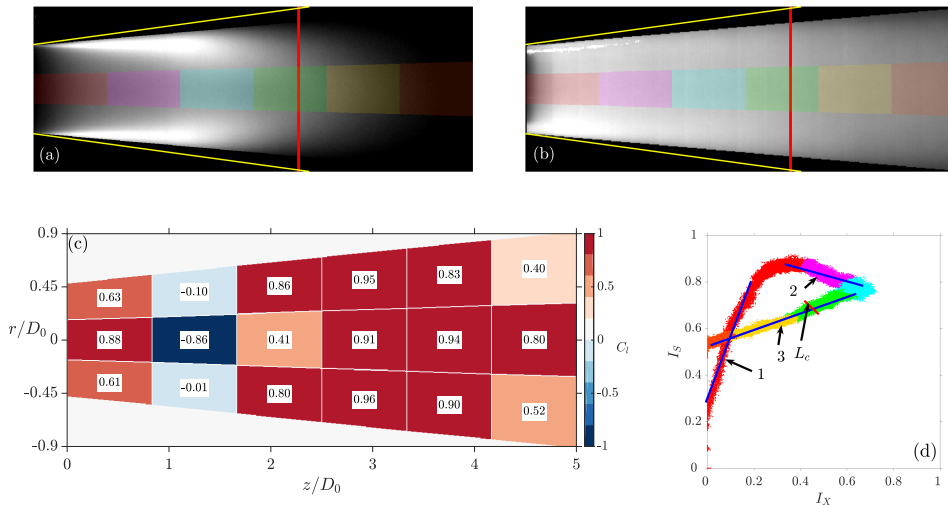


Figure 3.7: A comparison similar to that shown in Fig. 3.6 was also performed for $\sigma = 0.72$.

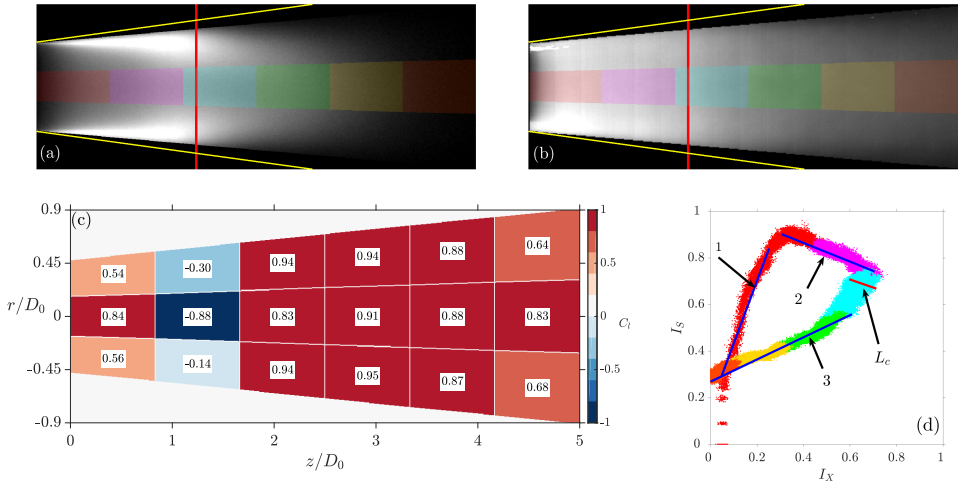


Figure 3.8: A comparison similar to that shown in Fig. 3.6 was also performed for $\sigma = 0.88$.

manner, quantitatively.

To this end, a quantitative comparison of the grayscale intensities from the two techniques is performed. This is done so by dividing the entire domain into smaller regions of interest or zones. Points (or pixels) from each zone can then be placed onto a coordinate space, formed by the grayscale intensities in X-ray images (I_X) and shadowgraphy images (I_S). Using these scattered points, a local correlation coefficient, C_l^S , can be defined for each zone. The division of the entire domain into zones is performed with two considerations. Firstly, these zones should be small enough to allow for a good spatial resolution of these local correlation coefficients. Secondly, these zones should be large enough to contain sufficient scatter points. Decreasing the size of the zone will lead to having fewer scatter points, which may even collapse around the same point. This might lead to an incorrect interpretation of the local correlation coefficient. Thus, the domain was divided into three zones along the radial direction and into six along the streamwise direction. The number of sampling points increases from about 15000, in the zones nearest to the throat, to 25000, in the zones furthest from the throat, due to the diverging nature of the test section.

The local correlation coefficients are then shown in Figs. 3.6 to 3.8(c), for the three cavitation numbers. In each case, it is seen that there is an initial short region with acceptable positive correlation coefficients which quickly begin to deteriorate along the downstream direction, even reaching negative values (for the higher cavitation numbers). This region is then followed by a region of recovery in the correlation coefficients back to a stable, high, positive value. However, these deterioration and recovery lengths are clearly dependent on the cavitation number.

The above behavior of the correlation coefficients can also be seen in the colour-coded scatter points shown in Figs. 3.6 to 3.8(d). The colour-coded scatter points correspond to

^S C_l quantifies the statistical relationship between the grayscale intensities obtained by the two techniques.

locations in the local zones of the same colour shown in Figs. 3.6 to 3.8(a)-(b). It is seen that the scatter points in the zones follow a loop-like trajectory along the downstream direction. The trajectories in each of the three cases have three distinct linear regions. The first line corresponds to the aforementioned region with an acceptable positive correlation coefficient, while the second and third lines are related to the regions of deteriorating and recovering correlation coefficients, respectively. For the cavitation numbers of 0.72 and 0.88, the second line even has a negative slope.

Table 3.1: Slopes of the approximate linear fits as well as non-dimensional cavity lengths in Figs. 3.6 to 3.8. m_n denotes the slope of the line n while the cavity length (L_c) is normalized by the throat diameter (D_0). C_g is the global correlation coefficient.

σ	m_1	m_2	m_3	$\frac{L_c}{D_0}$	C_g
0.60	3.49	0.18	0.34	3.54	0.77
0.72	2.90	-0.45	0.36	3.02	0.80
0.88	4.33	-2.05	0.55	1.82	0.81

Another quantity of interest here is the cavity length (L_c), or the streamwise length of the cavity along the venturi walls, immediately before it detaches and vortices are shed. Cavity lengths are derived using the shadowgraphy images, based on the formulation used by Long et al. (2017). It is expressed as $L_c = D_0 \cdot (L_{c,pix}/D_{0,pix})$. Here, $L_{c,pix}$ and $D_{0,pix}$ are the cavity length and throat diameter, respectively, in number of pixels. The same procedure is not applicable to the X-ray data due to a poor signal-to-noise ratio in the instantaneous X-ray images. The cavity length for all the three cavitation numbers is located near the onset of the third ‘correlation regime’ (or Line 3).

Slopes of these three lines along with the cavity length and the global correlation coefficient (C_g , correlation coefficient obtained by considering the entire venturi) are summarized in Table 3.1. The relatively high global correlation coefficient underlines that the two images provide a similar information qualitatively.

3.4. DISCUSSION

The results demonstrate the absence of universal quantitative congruity between grayscale intensities obtained via shadowgraphy and X-ray imaging. This result is not very surprising given that shadowgraphy would not be expected to successfully tackle opaque media. These observations are also in line with the qualitative results of Mitroglou et al. (2016) and Lorenzi et al. (2017). What distinguishes the images from the two techniques is the amount of recognizable information about the flow structures, as stated previously. In the following discussion, it is assumed that the X-ray intensities (I_X) represent the ground truth.

The presence of an initial positive correlation (denoted as Line 1 in Figs. 3.6 to 3.8(d)) immediately downstream of the venturi throat is common to all the cavitation numbers. This arrives from the fact that there is a gradual rise in the grayscale intensities in both sets of images. In the region furthest downstream from the throat, both sets of images are characterized by gradually decreasing grayscale intensities, which leads to the formation of a second positively correlated region (denoted as Line 3 in Figs. 3.6 to 3.8(d)). As

shown in Table 3.1, the slopes of these two regions (Line 1 and Line 3) are not equal. The region in between the aforementioned two regions (denoted as Line 2 in Figs. 3.6 to 3.8(d)) displays contrasting correlation behaviour. The central regions of the X-ray images, like the shadowgraphy ones, are characterized by an initial rise in grayscale intensities followed by a region of continuous decline. However, the streamwise length over which this increase happens is considerably larger for the X-ray images than in the shadowgraphy images (at least for σ of 0.72 and 0.88), which leads to a region of negative correlations in these two cases.

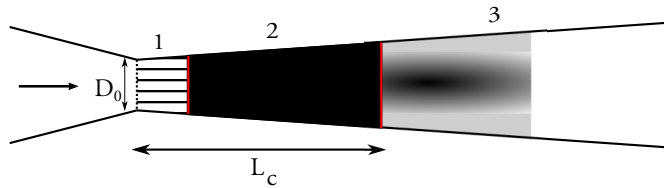


Figure 3.9: Three different regimes are observed in the shadowgraphy images pertaining to the current geometry. In this schematic, the darker the shade, the higher the vapor phase visualized. Regime 1: Streaks of tiny vapor bubbles. Regime 2: Cavity grows in size near the venturi walls, acting as a specular reflector to visible light. Regime 3: Cavity moves away from the walls, and collapses. The flow is from left to right.

A hypothesis for the above observations is postulated, and illustrated through a simplified schematic in Fig. 3.9. Three regimes have been demarcated. The initial region immediately downstream of the throat is occupied by a swarm of tiny bubbles, forming streaks. In this region, the density of the bubbles is low enough for shadowgraphy to return a reliable impression of the void fractions. Since visible light still has good penetrability, a modified Beer-Lambert law Wind and Szymanski (2002) for the transmittance of light may still be applicable. The second region is characterized by the bubbles having coalesced into a thicker film which exists very close to the venturi walls. This is a problem for the shadowgraphy technique, as the camera is unable to capture information from any depth beyond the cavities near the wall. The cavity basically acts as a specular reflector for light. The third region, usually downstream from the cavity length location, is characterized by detached cavities that have drifted away from the wall, and towards the center, followed by a collapse of the cavitation cloud into smaller bubbles. Further downstream, a fully liquid phase is recovered.

The presence of distinct regimes can be confirmed via the tomographic reconstruction of the vapor content at multiple cross-sections, illustrated in Fig. 3.10. This tomographic reconstruction has been done via the X-ray images. Filtered back projection is applied to the cone-beam 2D time-averaged X-ray image using the ASTRA Toolbox van Aarle et al. (2016). Detailed explanation of the reconstruction and the calibration procedure are given in chapter 4. One disadvantage of these time-averaged reconstructions is its inability to distinguish a coalesced cavity film from a swarm of tiny bubbles, occupying the same volume.

Four cross-sections have been considered here. It is clear that there is a development of a cavity film-like structure near the circumference of the cavity, whose thickness increases in the streamwise direction (for example, consider Sections A and B in Fig. 3.10). When sufficiently thick, this film would be obstructive for the shadowgraphy technique.

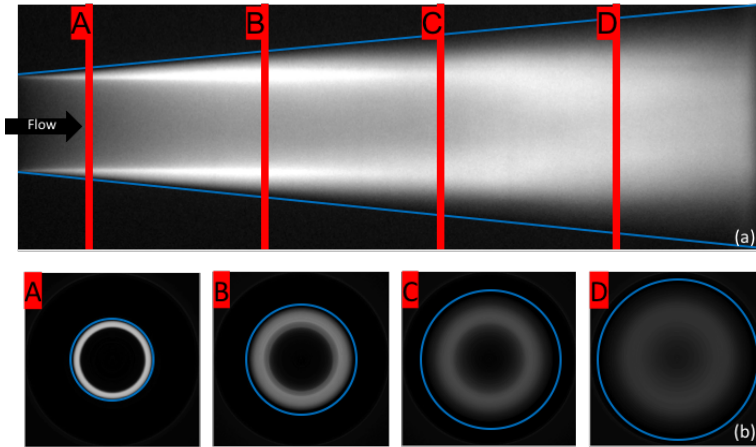


Figure 3.10: Tomographic reconstruction of the void fractions. Sections A and B illustrate the presence and development of a cavity film near the wall circumference while Sections C and D exemplify the detachment, drifting towards the centerline and subsequent collapse of the cavity film. (a) The streamwise locations of the four different planes considered. The venturi walls are shown in blue. (b) Tomographic reconstruction of the void fractions in the above four cross-sections. Lighter grayscale values indicate higher presence of vapor and vice versa. Here, $\sigma = 0.47$.

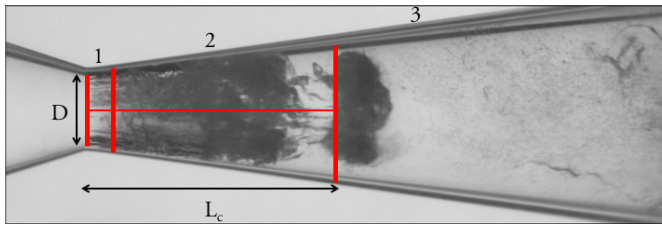


Figure 3.11: An instantaneous snapshot from the shadowgraphy experiment for $\sigma = 0.60$, supporting the presence of the three regimes proposed in Fig. 3.9. Regime 1: Thin streaks of tiny bubbles along the circumference. Regime 2: The cavitation film develops near the walls of the venturi. Regime 3: The cavity drifts away from the walls while moving towards the center, and in the subsequent snapshots, it collapses into tinier bubbles with the liquid phase being regenerated further downstream. The vertical red lines demarcate the three regimes.

This would correspond to regime 2 hypothesized in Fig. 3.9. However, beyond a certain point, these cavities drift away from the walls and begin to collapse (for example, consider Sections C and D in Fig. 3.10). This cavity detachment and subsequent regeneration of the liquid phase would be beneficial for shadowgraphy. This would correspond to regime 3 illustrated in Fig. 3.9.

On first sight, it appears that regime 1 shown in Fig. 3.9 is absent in the tomographic reconstructions considered in Fig. 3.10. This happens due to the smoothing of the bubble streaks in the time-averaged images. Thus, an instantaneous snapshot from the shadowgraphy measurements is considered in Fig. 3.11, which too illustrates the different regimes. Regime 1, in the short distance immediately downstream of the throat, has short streaks of

3

tiny bubbles along the walls, which does not hinder the camera's view much. This explains the initial region of positive correlation from the intensity comparison graphs (Figs. 3.6 to 3.8(d)). By the time the bubbles coalesce near the walls to form a cavity film, the vapor fraction near the walls is high enough to obstruct the camera's view and give an incorrect impression of the void fraction. This returns the region with relatively poorer correlation coefficients from the intensity comparison graphs. Downstream of the streamwise location of the cavity length, the cavity detaches from the circumferential wall, meanders towards the center, before collapsing into tinier bubbles and turning back into the liquid phase. This region marks an improvement in the correlation coefficients comparing the two techniques. Upon taking a time average of many such instantaneous images, a smoother version of the instantaneous snapshot in Fig. 3.11 shall be obtained. The intermittency of the flow would also determine the grayscale intensities in the time-averaged image.

It should also be noted that a correlation coefficient close to unity simply implies the existence linear relation between the quantities being compared (i.e. $I_S = m \cdot I_X$, where m is arbitrary). If actual line-integrated void fractions were being compared instead of intensities, the slope relating the line-integrated void fractions extracted from the two techniques would have to equal unity in order to establish equivalency of the two imaging techniques. However, such a comparison is not possible as the grayscale intensities from shadowgraphy do not have a straightforward relation with line-integrated void fractions. For example, in both cases, where the venturi contains only air or only water, identical grayscale intensities would be recorded by shadowgraphy. For this reason, an uncertainty analysis on the accuracy of shadowgraphy for void fraction estimation is impractical.

In quantifying void fractions from X-ray imaging, the two dimensional X-ray image possessing information on the line-integrated void fractions, is only an intermediate step. A tomographic reconstruction akin to the one shown in Fig. 3.10 would be necessary for local void fraction quantification. A hypothetical tomographic reconstruction of the two-dimensional shadowgraphy images would give different estimates of the void fraction than that of X-ray, stemming from the differences in the original two-dimensional images. Thus, it can be said that quantitative estimates of the void fraction in cavitating flows from time-averaged shadowgraphy experiments are likelier to represent the truth, only in regions with low fractions of dispersed bubbles or detachment of the cavities from the walls (regimes 1 and 3). However, it is highly likely to provide improper estimates of the void fractions in regions with coalesced cavities near the walls, as evidenced by the regions of negative correlations for cavitation numbers of 0.72 and 0.88. These conclusions could also be extrapolated to the other multiphase flows introduced at the beginning of this chapter.

An influential factor that has been unaccounted for in the entire analysis thus far, is the relative placement of the measurement section (venturi) with respect to the illuminating source (LED panel/X-ray source) and detector (High-speed camera/X-ray detector). It can be expected that a configuration different to the one used in the current study would result in a different grayscale intensity map in the two-dimensional images. This would be a result of a new line of sight between the source and the detector. Eventually, this would translate into a different estimate of the void fraction at a given location. However, this factor is not expected to affect the qualitative hypothesis postulated in Fig. 3.9, i.e. on

the applicability of shadowgraphy to the three regimes. Nevertheless, differences can be expected in the cavity lengths as well as the slopes of the linear fits to local correlation coefficients in Table 3.1.

A look-up table like procedure to correlate the void fractions and the grayscale intensities in shadowgraphy images can be implemented for the different regions. This would allow for a more accurate estimation of void fractions via shadowgraphy, especially when knowledge of the precise locations of the regimes is available. However, if this information is unavailable, the look-up table would prove fruitless, as there is no unique value of line-integrated void fraction for a single grayscale intensity obtained by shadowgraphy. For example, $I_S = 0.4$ in Fig. 3.8(d) has two possible values for I_X , depending on the regime under consideration. Constructing and implementing a careful look-up table procedure for different regimes in an internal flow is likely to prove an arduous task.

3.5. CONCLUSIONS

Images from shadowgraphy and X-ray measurements were compared. Correlations were made based on the grayscale intensity values along the streamwise direction for a cavitating flow through a venturi, at three different cavitation numbers of 0.60, 0.72 and 0.88. It was assumed that the information obtained through the X-ray imaging technique represented the truth.

Three distinct ‘correlation regimes’ were identified for the flow considered. The first region, associated with a swarm of tiny bubbles along the walls, is short in extent with a positive correlation between the grayscale intensity values from the two techniques. The second region, associated with a cavity film growing near the wall, shows more variability across the different cavitation numbers and may display either a positive ($\sigma = 0.60$) or a negative ($\sigma = 0.72$ and 0.88) correlation. The third region, associated with the drifting of the cavity away from the walls towards the central region of the venturi as well as collapse of the cavities, is found beyond the estimated location of the cavity lengths. While shadowgraphy may still return reliable estimates of void fractions in flows resembling the first and third regions, it could lead to improper conclusions about the void fraction profiles in flows that resemble the second region.

REFERENCES

- Bauer, D., Chaves, H., and Arcoumanis, C. (2012). Measurements of void fraction distribution in cavitating pipe flow using x-ray CT. *Measurement science and technology*, 23(5):055302.
- Dunn, P. F., Thomas, F. O., Davis, M. P., and Dorofeeva, I. E. (2010). Experimental characterization of aviation-fuel cavitation. *Physics of Fluids*, 22(11):117102.
- Ganesh, H., Mäkiharju, S. A., and Ceccio, S. L. (2016). Bubbly shock propagation as a mechanism for sheet-to-cloud transition of partial cavities. *Journal of Fluid Mechanics*, 802:37–78.
- Gnanaskandan, A. and Mahesh, K. (2016). Large eddy simulation of the transition from

- sheet to cloud cavitation over a wedge. *International Journal of Multiphase Flow*, 83:86–102.
- Jahangir, S., Hogendoorn, W., and Poelma, C. (2018). Dynamics of partial cavitation in an axisymmetric converging-diverging nozzle. *International Journal of Multiphase Flow*, 106:34–45.
- Khlifa, I., Vabre, A., Hočevár, M., Fezzaa, K., Fuzier, S., Roussette, O., and Coutier-Delgosha, O. (2017). Fast X-ray imaging of cavitating flows. *Experiments in Fluids*, 58(11):157.
- Kowalski, K., Pollak, S., Skoda, R., and Hussong, J. (2018). Experimental study on cavitation-induced air release in orifice flows. *Journal of Fluids Engineering*, 140(6):061201.
- Leandro, J., Bung, D., and Carvalho, R. (2014). Measuring void fraction and velocity fields of a stepped spillway for skimming flow using non-intrusive methods. *Experiments in Fluids*, 55(5):1732.
- Leandro, J., Carvalho, R., Chachereau, Y., and Chanson, H. (2012). Estimating void fraction in a hydraulic jump by measurements of pixel intensity. *Experiments in fluids*, 52(5):1307–1318.
- Long, X., Zhang, J., Wang, J., Xu, M., Lyu, Q., and Ji, B. (2017). Experimental investigation of the global cavitation dynamic behavior in a venturi tube with special emphasis on the cavity length variation. *International Journal of Multiphase Flow*, 89:290–298.
- Lorenzi, M., Mitroglou, N., Santini, M., and Gavaises, M. (2017). Novel experimental technique for 3D investigation of high-speed cavitating diesel fuel flows by X-ray micro computed tomography. *Review of Scientific Instruments*, 88(3):033706.
- Mitroglou, N., Lorenzi, M., Santini, M., and Gavaises, M. (2016). Application of X-ray micro-computed tomography on high-speed cavitating diesel fuel flows. *Experiments in Fluids*, 57(11):175.
- Nadeem, H. and Heindel, T. J. (2018). Review of noninvasive methods to characterize granular mixing. *Powder Technology*, 332:331–350.
- Perpar, M., Polutnik, E., Pečar, M., and Žun, I. (2014). Bubbly structures in a cavitating slot orifice. *Experimental Thermal and Fluid Science*, 53:57–69.
- Puli, U. and Rajvanshi, A. (2012). An image analysis technique for determination of void fraction in subcooled flow boiling of water in horizontal annulus at high pressures. *International Journal of Heat and Fluid Flow*, 38:180–189.
- Rana, K., Agrawal, G., Mathur, J., and Puli, U. (2014). Measurement of void fraction in flow boiling of ZnO–water nanofluids using image processing technique. *Nuclear Engineering and Design*, 270:217–226.
- Ursenbacher, T., Wojtan, L., and Thome, J. R. (2004). Interfacial measurements in stratified types of flow. Part I: New optical measurement technique and dry angle measurements. *International Journal of Multiphase Flow*, 30(2):107–124.

- van Aarle, W., Palenstijn, W. J., Cant, J., Janssens, E., Bleichrodt, E., Dabravolski, A., De Beenhouwer, J., Batenburg, K. J., and Sijbers, J. (2016). Fast and flexible X-ray tomography using the ASTRA toolbox. *Optics express*, 24(22):25129–25147.
- Van Ommen, J. R. and Mudde, R. F. (2008). Measuring the gas-solids distribution in fluidized beds—A review. *International Journal of Chemical Reactor Engineering*, 6(1).
- Wang, C., Huang, B., Zhang, M., Wang, G., Wu, Q., and Kong, D. (2018a). Effects of air injection on the characteristics of unsteady sheet/cloud cavitation shedding in the convergent-divergent channel. *International Journal of Multiphase Flow*, 106:1–20.
- Wang, D., Song, K., Fu, Y., and Liu, Y. (2018b). Integration of conductivity probe with optical and x-ray imaging systems for local air–water two-phase flow measurement. *Measurement Science and Technology*, 29(10):105301.
- Wind, L. and Szymanski, W. (2002). Quantification of scattering corrections to the Beer-Lambert law for transmittance measurements in turbid media. *Measurement Science and Technology*, 13(3):270.
- Wojtan, L., Ursenbacher, T., and Thome, J. R. (2004). Interfacial measurements in stratified types of flow. Part II: Measurements for R-22 and R-410A. *International Journal of Multiphase Flow*, 30(2):125–137.
- Wojtan, L., Ursenbacher, T., and Thome, J. R. (2005). Measurement of dynamic void fractions in stratified types of flow. *Experimental Thermal and Fluid Science*, 29(3):383–392.
- Wosnik, M. and Arndt, R. E. (2013). Measurements in high void-fraction bubbly wakes created by ventilated supercavitation. *Journal of Fluids Engineering*, 135(1):011304.

4

VOID FRACTION MEASUREMENTS IN PARTIAL CAVITATION REGIMES BY X-RAY COMPUTED TOMOGRAPHY

This chapter is based on: S. Jahangir, E.C. Wagner, R.F. Mudde, C. Poelma, *Void fraction measurements in partial cavitation regimes by X-ray computed tomography*, International Journal of Multiphase Flow **120**, 103085 (2019).

4.1. INTRODUCTION

Cavitation in a flow occurs when the static pressure in the flow falls below the vapor pressure of the liquid, resulting in the formation of vapor bubbles. In many hydrodynamic applications, such as ship propellers, hydro turbines or diesel injectors, cavitation often cannot be avoided due to their operating conditions. If a cavitation bubble or cloud collapses close enough to a solid wall, it will produce a high-speed micro-jet and shock waves, which can result in erosion (Dular and Petkovšek, 2015; Franc and Michel, 2006; Peng et al., 2018). Understanding the correct cavitation physics is important because then the adverse consequences such as erosion can be diminished.

It is of great importance to understand the development and dynamics of local void fractions in cavitating flows. Among the studies on cavitation, high-speed visualization is the most popular technique to investigate the cavitation evolution (Chen et al., 2015; Laberteaux et al., 1998). Simple optical methods are limited to investigating cavitation occurring close to the wall region. However, quantitative information regarding the void fractions is difficult to obtain from high-speed imaging, because the cavitation bubbles block and scatter light and thus make the flow opaque (Dash et al., 2018). Due to the lack of penetrability of visible light in such optically opaque flows, advanced alternative techniques have been developed over the years to quantitatively characterize the phenomena occurring in the interior of the flow and to quantify void fractions. Broadly, these techniques include optical probes, Electrical Capacitance Tomography, Radioactive Particle Tracking, (X-ray/Gamma ray) Computed Tomography (CT), Magnetic Resonance Imaging, with each technique having its advantages and limitations. Quantitative non-intrusive techniques have been reviewed in literature (Chaouki et al., 1997; Kastengren and Powell, 2014). Impedance tomography systems have been developed to investigate multiphase flows, and they are reviewed by Holder (2004). Impedance tomography systems are relatively cheap, but such systems are limited by the number of electrodes that can be located on the boundary. This limits the spatial resolution that can be achieved in the reconstruction. Gamma and X-ray imaging have been used to study multiphase flows such as cavitating flows and bubbly flows. X-ray imaging has been demonstrated as a valuable technique to quantify the void fractions in various cavitation related studies (Bauer et al., 2012; Khelifa et al., 2017; Mäkiharju et al., 2013; Mitroglou et al., 2016). Void fractions are of high importance for the understanding of shedding behavior in periodic cavitation. Recently Ganesh et al. (2016) found that under particular conditions a condensation shock can be the dominant mechanism for periodic cavitation shedding, instead of the re-entrant jet. Time-resolved X-ray densitometry was used to investigate the local void fractions in the flow field. They found that void fractions increase with an increase in cavitation intensity. These experiments were performed on a 2D wedge. A converging-diverging nozzle ('venturi') is used in this study. Due to its high contraction ratio, a broader cavitation dynamic range can be attained. However, by using a standard 2D X-ray densitometry system, only information integrated along lines of sight about the void fraction within the region of interest can be determined from a single viewing angle. It is unlikely to obtain information regarding the structures inside the cavitation.

X-ray CT is widely used in medical imaging. It uses the relation between the material properties and the attenuation coefficient of X-rays. Images are created using the attenu-

ation along the beam paths recorded at various viewing angles. This capability inspired the idea to use X-ray CT to measure the void fraction distribution and radial geometric characteristics in the flow. Bauer et al. (2012) did the first study to investigate an internal cavitation flow with the X-ray CT-scanner on a purpose-built nozzle. Mitroglou et al. (2016) also performed X-ray CT measurements on a smaller scale nozzle ($D = 3$ mm). From both of these studies, the obtained time-averaged CT images gave useful insights on the flow structures inside the nozzle. However, all the previous studies which investigated the internal cavitation flow were performed on nozzles, to the best of authors knowledge. Using a nozzle with a constant diameter, it is impossible to obtain different partial cavitation regimes.

Jahangir et al. (2018) used a venturi in combination with high-speed visualization to distinguish between two partial cavitation regimes: the re-entrant jet mechanism and the bubbly shock mechanism. The authors further showed that the non-dimensional frequency (Strouhal number) can be used to identify the two partial cavitation regimes. The Strouhal number (St) is defined as:

$$St = \frac{fD_0}{u_0}, \quad (4.1)$$

where D_0 is the throat diameter, the shedding frequency of the cavitation clouds is given by f and u_0 is the free stream velocity of the flow in the venturi throat. In Fig. 4.1, the Strouhal number (St) is shown as a function of the cavitation number. The cavitation number (σ) is defined as:

$$\sigma = \frac{p - p_v}{\frac{1}{2}\rho u_0^2}, \quad (4.2)$$

where p is the downstream pressure, p_v is the vapor pressure¹ of the liquid at the temperature of the setup and ρ is the density of the fluid. The shedding frequency was determined using high-speed shadowgraphy. Details can be found in Jahangir et al. (2018). The study found that all points collapsed on a single curve, with the shedding frequency being a function of cavitation number. From visual inspection of the shadowgraphy data taken for various cases in Fig. 4.1, two different cavitation mechanisms were identified as a function of cavitation number: for $\sigma > 0.95$ cloud cavitation shedding is governed by the re-entrant jet mechanism. For $\sigma < 0.75$ cloud cavitation shedding is governed by the bubbly shock mechanism. The cavitation region in between is governed by both mechanisms, so it is called the transition region. In this study, we will examine the void fractions using X-ray CT in the above-mentioned regimes using the same geometry (see also Fig. 4.2, discussed in detail later). To that end, one of the representative case from both the re-entrant jet mechanism and the bubbly shock mechanism will be used for the determination of void fractions. A case with the cavitation number of $\sigma = 1$ from the re-entrant jet mechanism is selected and another case with $\sigma = 0.40$ from the bubbly shock mechanism is selected (shown with red arrows in Fig. 4.1).

The advantage of the X-ray CT is that it does not only measure the spatial average of the void fraction like it would be for standard X-ray imaging, but the void fraction

¹The vapor pressure is calculated using the Antoine equation at the temperature measured during the experiments (18 °C - 26 °C).

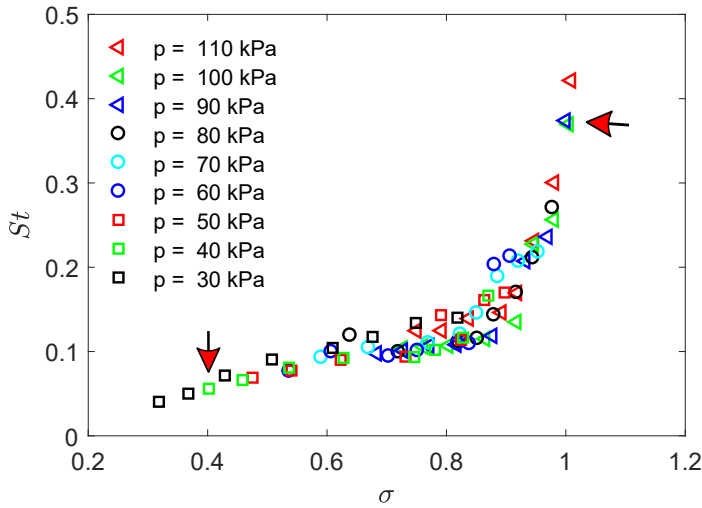


Figure 4.1: Dimensionless frequency of the cavitation shedding cycle as a function of the cavitation number for the venturi, replotted from Jahangir et al. (2018). The red arrows show the cavitation numbers selected for the CT reconstruction.

distribution along different cross-sections of the venturi. The data is essential to validate our assumptions regarding the physical mechanisms. Furthermore, it is currently being used to validate numerical models.

The chapter is organized in the following manner. The experimental details are described in Section 4.2, while Section 4.3 explains in detail the data processing and methods used to explain the flow dynamics. The calibration and results are reported in Section 4.4. The conclusions follow in Section 4.5.

4.2. EXPERIMENTAL DETAILS

4.2.1. FLOW FACILITY

A schematic overview of the flow setup utilized for the experiments is represented in Fig. 4.2[†]. The flow in the closed-loop system is driven by a centrifugal pump, and a flowmeter (KROHNE flowmeter, type: IFS 4000F/6) is used to measure the volumetric flow rate (Q). The measurements from the downstream pressure transducer (calculated from P_3 in Fig. 4.2), the flowmeter, and the temperature sensor are used to determine the cavitation number. A water column present at an angle (due to space constraints) is used to collect the air bubbles entrained in the flow during degasification, and to vary the global static pressure of the system. A vacuum pump is used to control the global static pressure below ambient pressure down to 20 kPa absolute. The experimental setup shown in Fig. 4.2 had to be reoriented for the X-ray imaging measurements compared to shadowgraphy measurements performed by Jahangir et al. (2018) due to space restrictions

[†]The experimental setup could not be constructed in horizontal position due to space constraints.

of the X-ray facility. Therefore, the entrance length had to be reduced from 40D to 10D. Nevertheless, the flows from the two experiments for the same cavitation number were confirmed to be equivalent, as the pressure loss coefficients across the venturi (K) were alike for both cases (explained in Section 4.4). The pressure loss coefficient K is given by:

$$K = \frac{\Delta p}{\frac{1}{2}\rho u_0^2}, \quad (4.3)$$

where Δp is the pressure loss over the venturi (calculated from P_1 and P_2 in Fig. 4.2). A visual examination also established symmetry of the top and bottom halves of the time-averaged shadowgraphy images by placing a mirror at an angle of 45° below the venturi in the horizontal configuration. The side-view and the bottom-view were visualized simultaneously, in order to verify whether the cavitation dynamics are axisymmetric. No significant difference was found, therefore effects due to gravity can be neglected.

In Fig. 4.2(inset), a picture of the venturi can be seen with its geometrical parameters. The venturi is milled out from a block of polymethylmethacrylate (PMMA) and has a throat diameter (D_0) of 16.67 mm. The convergence and divergence angles are 18° and 8° to the axis, respectively (inspired by previous studies: Hayashi and Sato (2014); Long et al. (2017); Tomov et al. (2016)). An area ratio of 1:9 (area of the throat versus exit area) is chosen. The flow direction is from bottom to top in the venturi. Further details on the experimental setup can be found in Jahangir et al. (2018).

4.2.2. EXPERIMENTAL PROCEDURE

A vacuum pump is utilized to degasify the water before the experiments. A water sample is taken for the determination of the gas content in the system using an oxygen sensor (RDO PRO-X Probe). After running the setup for 60 minutes at lower ambient pressure with cavitation, the oxygen content reduces from oversaturated to approximately 40%. All the measurements were performed at approximately the same oxygen content.

The setup is run for 5 minutes before the measurement series is started, in order to mix the water in the system and to obtain a uniform water temperature. The global static pressure of the system is fixed at a prescribed value. The measurements are started when the pressure readings are constant. For the specified global static pressure, measurements are conducted at different flow velocities. A data acquisition system is used to record all the sensor values (pressure, flow rate, and temperature). X-ray images (explained in the upcoming paragraph) are recorded simultaneously. In the end, the oxygen content is measured again by taking a water sample from the setup.

4.2.3. X-RAY IMAGING

In this study, the cavitating flow inside the venturi was measured using X-ray imaging. The X-ray setup originally consisted of three standard industrial type X-ray sources (Yxlon International GmbH) with a maximum energy of 150 keV working in cone beam mode. Each X-ray source generates a cone beam that can be detected by a detector plate on the opposite side of each X-ray source. For this study, the experiments were performed with one X-ray source and one detector plate to obtain the projected 2D output signals from the 3D cavitating flow.

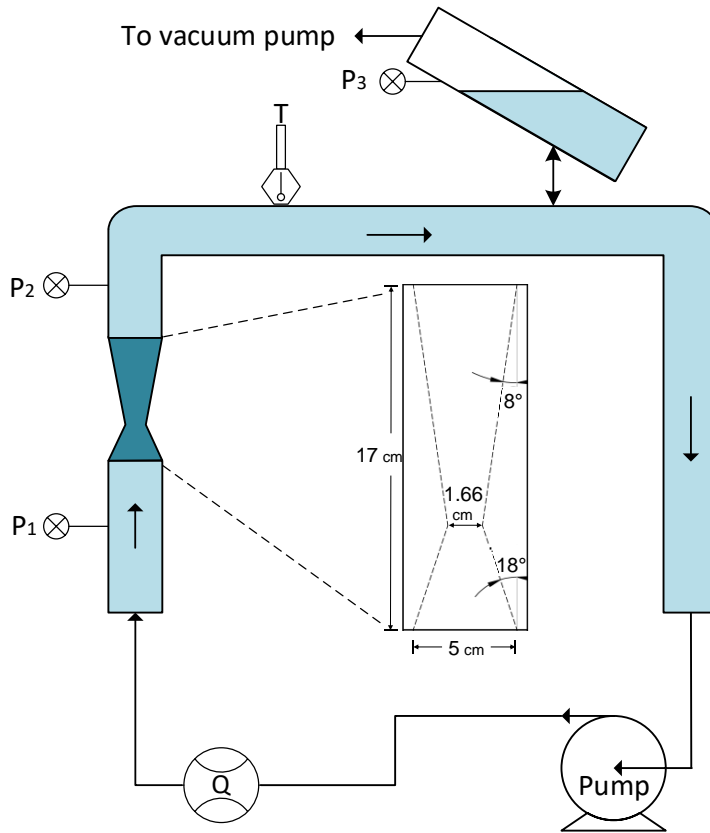


Figure 4.2: Schematic overview of the experimental facility indicating essential components (dimensions not to scale). The inset shows the geometry and relevant dimensions of the converging-diverging section.

Fig. 4.3(a) and (b) show a photograph of the measurement section in the X-ray setup and schematic overview of the method, respectively. A source-detector pair is used to measure the attenuation of the X-rays through the cavitating venturi. For the experiments, the venturi is placed (inclination ± 1 mm/m) in the center of the setup and 323 ± 2 mm from the X-ray source and 584 ± 2 mm from the detector plate. The X-ray source (Yxlon-Y.TU 160-D06) has a tungsten anode. The source is operated at 120 keV and 5 mA in order to achieve a high contrast between the liquid and vapor phases within the venturi. The flat detector, Xineos-3131 CMOS model, consists of a 307×302 mm² sensitive area. The detector provides the total photon count in the range of 40-120 keV. For the experiments, a field of view of 1548×660 pixels is chosen. Each pixel has a size of 198×198 μm^2 with 14 bits of pixel depth.

The entire experimental procedure was controlled with a workstation outside the setup room (closed with a lead sheet) guaranteeing a safe working condition. Using the workstation, it was possible to trigger the X-ray source and read out the signals from the

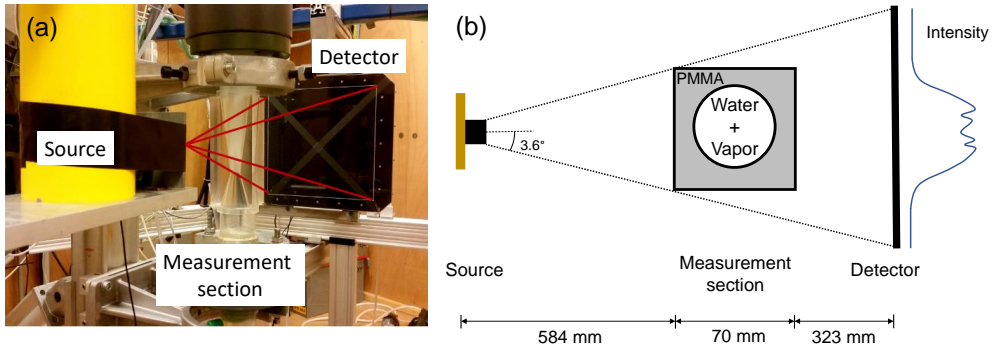


Figure 4.3: The basic arrangement and components of the X-ray setup and the flow facility. (a) Test-rig inside the X-ray setup. (b) Schematic of the X-ray imaging method with the source on the left, the measurement section in the middle, and the detector on the right indicating the superficial intensity (dimensions not to scale).

detector plate. Further details on the X-ray setup and the measurement technique can be found in Helmi et al. (2017); Maurer et al. (2015); Mudde et al. (2008). The X-ray images are recorded at 61 Hz during approximately 1 minute, which corresponds to 3700 images. Afterwards, these images are averaged. All results reported in the present study are based on the time-averaged X-ray images. As the typical shedding frequency is 40 Hz at $\sigma = 0.46$, this ensures that the statistics are based on sufficient shedding cycles.

4.3. DATA PROCESSING

4.3.1. IMAGE PROCESSING

The raw images acquired by the X-ray detector need several post-processing steps (black lines correction, background subtraction, and image adjustment) before they can be used to explain the cavitation dynamics. All of the following steps were performed using Matlab R2017a (The Mathworks Inc., Natick, USA) and the process is depicted in Fig. 4.4. Due to the orientation of venturi in the experimental setup, the images obtained from the X-ray detector show the venturi in a vertical position. The X-ray images were rotated by 90°; therefore, the bulk flow is from left to right in all images shown in the chapter.

The detector plate is constructed by a combination of smaller detector elements. Due to this construction, multiple black lines appear on the obtained images, as shown in Fig. 4.4(a). These black lines consist of a single pixel in either direction (vertical direction and horizontal direction), and they do not contain any data. These were replaced with intensities by linear interpolation of the pixel intensities on either side of the lines, as shown in Fig. 4.4(b). In the X-ray images, the vapor phase has higher grayscale intensities, while the liquid phase has lower grayscale intensities. This happens because the presence of vapor leads to lower attenuation of the X-rays along its path length (explained in Section 4.4.2). A background correction is performed for the X-ray images, for which background images with only the liquid phase without flow are captured. In order to improve the contrast, an image adjustment operation is performed on images. This process involves rescaling the grayscale intensities in order to have 1% of the data being saturated at high intensities and 1% of the data covering low intensities (Fig. 4.4(c)). This

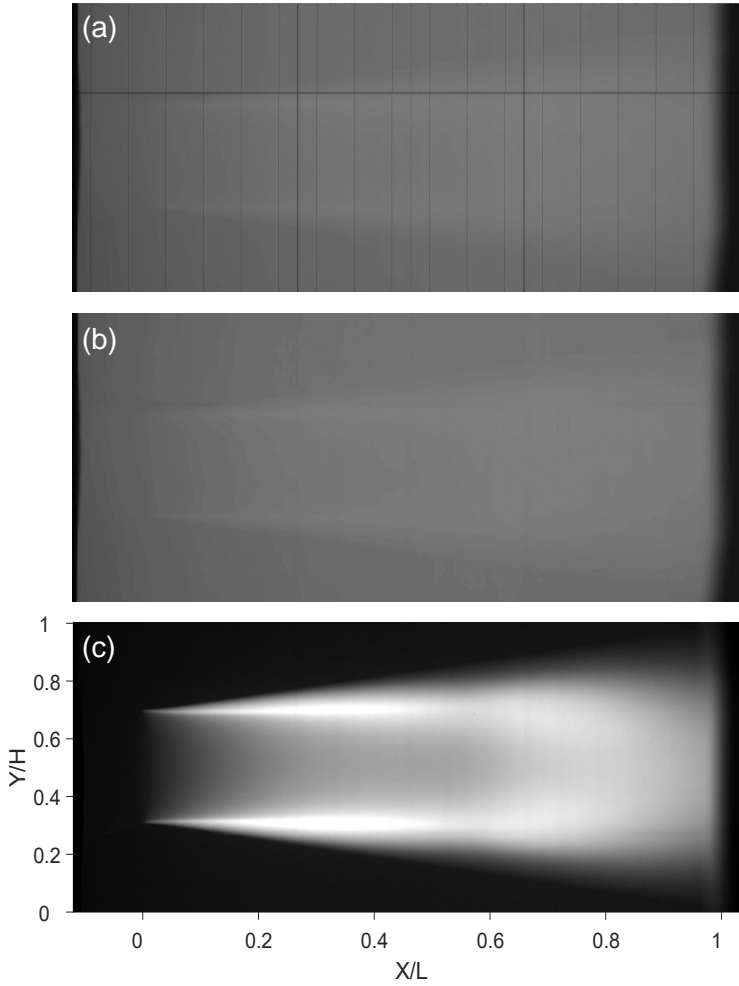


Figure 4.4: Time-averaged X-ray images of cavitating flow in the venturi at $\sigma = 0.40$: (a) raw time-averaged image obtained from the detector, (b) corrected image after removing black lines, and (c) the image obtained after background correction as well as adjusted to improve contrast (vapor is light gray, liquid is black). In all the images, the bulk flow occurs from the left to right.

arbitrary scaling has no influence on the quantitative void fraction, as this is based on a separate calibration procedure (discussed in Section 4.4.2).

As the vertical axis is not used (as will be discussed later), its origin is set arbitrarily. The origin of the horizontal axis, coinciding with the axial/streamwise direction, is set at the throat of the venturi. The axial location (X) is made dimensionless using the length of the measured part of the diverging section ($L = 9.3$ cm).

A convergence study was conducted on the X-ray data of the cavitating flow, as shown in Fig. 4.5. The term on the y-axis ('relative change') is calculated as follows: three points along the centerline are chosen: $X/L = 0.11$, 0.33 and 0.55 , which cover regions containing cavitation. The averaged grayscale intensities of these points are computed from the first 50 X-ray images. Subsequently, an additional 50 images are used to calculate the new mean intensities. The difference between the new and old mean, divided by the old mean is shown as a function of the amount of total images used. The relative error reduces to less than 0.1% after 3700 images. Hence, the sampling time of one minute allows obtaining sufficient data for statistics with a minimum error from the mean.

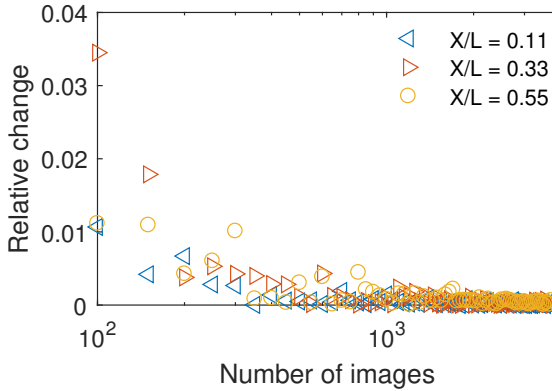


Figure 4.5: Convergence study of the time-averaged X-ray images, using three points on the centerline. The relative change is less than 0.1% after 3700 images.

4.3.2. COMPUTED TOMOGRAPHY

CT, also known as computed tomography, makes use of computer-processed combinations of many X-ray measurements taken from different angles to produce cross-sectional images ('slices'). The process of CT involves a collection of projections from several angles of the X-ray intensity attenuated by the object of interest on the detector. The collected data ('sinogram') is then reconstructed utilizing algorithms, such as filtered back projection.

In the X-ray imaging system used in this study shown in Fig. 4.3, the distance between the detector and the source is much larger than the measuring area, and the viewing angle is minimal. The difference between the path lengths measured at the maximum angle and parallel to the detector is 0.1% of the parallel beam path. Therefore, the cavitation cloud is assumed to be projected to the detector by parallel X-ray beams (Wang et al., 2018).

This assumption is also validated by comparing the reconstructed geometry against the nominal geometry, as shown in Fig. 4.7 (explained in the upcoming paragraph). As the measurement section is axisymmetric, we assume axisymmetry of the time-averaged flow. Fig. 4.6(a) shows a time-averaged X-ray image, the starting point for our analysis. The red lines indicate the overall shape of the venturi. Note that we have shifted these lines outward by a few pixels so that they do not obscure the data. For all upcoming figures this minor shift was used for clarity. A slice (vertical red line in Fig. 4.6(a)) is extracted from the time-averaged image and stacked 360 times to construct a sinogram of 600×360 pixels as shown in Fig. 4.6(b). This sinogram represents the projections from 360° . This is a necessary intermediate step before CT reconstruction using the particular software used here. Filtered back projection is applied to the sinogram using the ASTRA Toolbox v1.8 (van Aarle et al., 2016). This is a flexible CT reconstruction open source toolbox which uses CPU and GPU based reconstruction algorithms for 2D and 3D data sets. In the present study, we use a CPU based implementation of the filtered back projection (FBP) algorithm for 2D data sets. It takes the source and detector data as input and returns the reconstruction. For this study, just the sinogram was used as an input and reconstructed CT slice was returned (Fig. 4.6(c)). The reconstruction algorithm resembles the inverse operation of a forward projection. But instead of each detector getting the line integral of the object function, each point on the object domain receives the value of the detector point where it projects to. So, in essence, the detective function is smeared out over the object domain. This is then done over all projection angles summing up the values in each direction (van Aarle et al., 2016).

A common cause of errors when reconstructing X-ray CT image are artifacts within the image. Conventional sources of artifacts are beam hardening and abrupt changes in density. Beam hardening is the most common artifact found in X-ray CT reconstruction. It causes the edges of the scanned measurement section to appear brighter than the center, even for homogeneous materials (Ketcham and Carlson, 2001). This effect is caused by the difference in absorption coefficients for various wavelengths when using a non-monochromatic source. An efficient way to decrease beam hardening (which is more severe in metals than plastics) is filtering low-energy soft X-rays with metal filters. For these measurements, no beam hardening filtration was used primarily due to the absence of metals which would result in a potential reduction in the image contrast imposed by extra filtration. The absence of beam hardening is also confirmed from the calibration plot, explained in Section 4.4.2.

Two different tests were performed to check the quality of reconstruction. A check on the diameters from reconstructed CT slices across 14 different axial positions of the full length of empty venturi was performed. The results were compared to the nominal diameters, as shown in Fig. 4.7. The diameters from CT slices matched quite well to the nominal geometry, a maximum error of less than 1.2% of the local diameter was found. Another check was based on the distribution of void fractions α . The relative error was found to be less than 0.9%, as will be discussed in Section 4.4.2.

After constructing a single slice, the process is repeated and multiple density slices of the venturi perpendicular to the centerline axis are created. Fig. 4.8(a) shows reconstructed slices at different axial positions, showing growth of the cavitation cloud. Most of the vapor is attached to the nozzle wall and persists until four diameters downstream

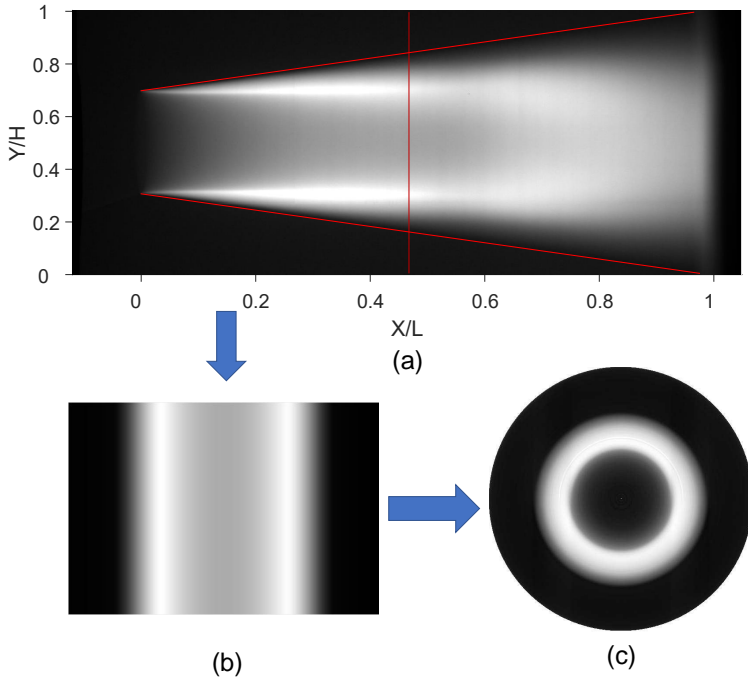


Figure 4.6: Schematic of post-processing procedure followed to obtain a cross-sectional CT slice. (a) Time-averaged X-ray image of the cavitating venturi at $\sigma = 0.40$ (vapor is light gray, liquid is black). (b) Sinogram created from an axial location at $X/L \approx 0.47$ (red line in (a)). (c) Cross-sectional CT image presented as side-view cut. See text for details on this procedure.

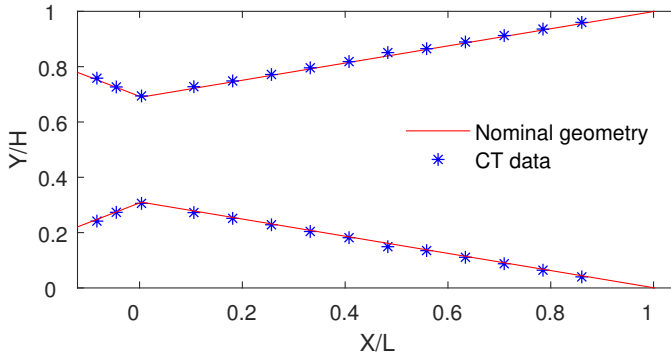


Figure 4.7: Validation of the diameters from CT slices using the nominal geometry. See text for details

of the throat. This is the point where the cavity detaches during the periodic shedding, which is also confirmed by the high-speed images (Jahangir et al., 2018). After detaching, the vapor cloud moves towards the center of the venturi and mixes with the liquid core. Fig. 4.8(b) shows the cross-section through the x - z plane. Fig. 4.8(b) is the cross-section,

and thus distinct from the X-ray image of Fig. 4.6(a). As can be seen in the figure, cavitation bubbles are also present in the liquid core, downstream of the venturi.

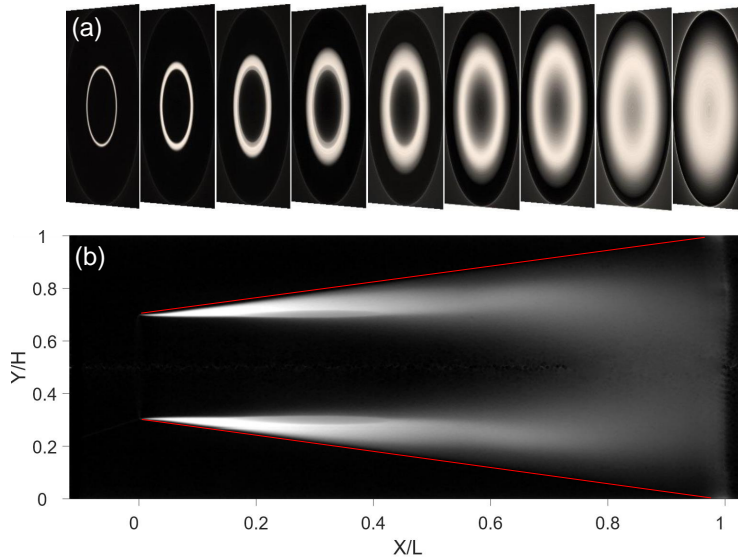


Figure 4.8: (a) Cross-sectional CT images at different axial positions showing growth of the cavitation cloud at $\sigma = 0.40$. The contrast in the images is adjusted individually for each slice for clarity. (b) Cross-section through the x - z plane, showing the presence of cavitation bubbles in the center of the liquid core downstream of the venturi.

4.4. RESULTS

With the venturi specified in Section 4.2, it is possible to initiate partial cavitation mechanisms such as the re-entrant jet mechanism and the bubbly shock mechanism at different cavitation numbers. An overview of these cavitation mechanisms can be found in Jahangir et al. (2018).

4.4.1. PRESSURE LOSS COEFFICIENT

The strength of cavitation is expressed using the cavitation number. With an increase in the flow velocity, the cavitation number decreases, implying more cavitation. With a decreasing cavitation number, the effective throat diameter is narrowed by the presence of the growing cavity. Because of the narrowed throat diameter for decreasing cavitation number, the pressure loss over the venturi will be higher. This is visible from measurement results, shown in Fig. 4.9. Here, the cavitation number is varied by changing the flow velocity at different static pressures, and the pressure loss coefficient K is reported. This implies that flow blockage is a function of cavitation number. For both the shadowgraphy experiments performed by Jahangir et al. (2018) and the present X-ray experiments, it can be seen that all points collapse on one line. The flows from the two experiments for the

same cavitation numbers are therefore assumed to be equivalent, as the pressure loss coefficients across the venturi (K) are similar for both cases.

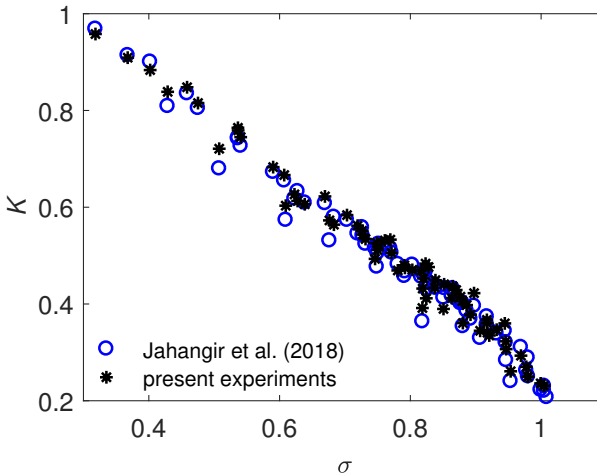


Figure 4.9: The pressure loss coefficient (K) as a function of the cavitation number for the experiments performed by Jahangir et al. (2018) (open markers) and the present experiments (asterisks).

4.4.2. CT VOID FRACTION CALIBRATION

Various approaches exist to obtain quantitative values of the local attenuation coefficient (or density, for simplicity). In our case, we opted for the following approach: images are recorded and divided by a reference image (I_R) for the case of only water. The ‘intensity’ that remains is proportional to the amount of vapor present between source and detector, as this has a lower attenuation than water. Using this reference method, all attenuation outside the region of interest (such as the non-axisymmetric PMMA parts of the test section) cancels out. The images are processed using the CT algorithm, which provides a three-dimensional reconstruction. Each voxel in this reconstruction contains information about the local attenuation coefficient. As our approach is based on relative X-ray image intensities, there is an unknown constant linking voxel values and the actual local attenuation. This coefficient is obtained from calibration experiments.

First, intensities were measured by the X-ray detector when the venturi contained only air and only water. Densities of air (1.27 kg/m^3) and water vapor² (0.804 kg/m^3) are far smaller than the density of water (997 kg/m^3). Therefore, air is a suitable alternative for water vapor because of the negligible difference in their mass densities and hence similar linear absorption coefficients (Bauer et al., 2018; Mitroglou et al., 2016). For the calibration with air, the venturi was left empty and it was filled with filtered water for the other case. The maximum intensity was recorded as 12580 for air, and it was 9045 for water at the streamwise plane of the throat, as shown in Fig. 4.10. Approximately 21% of

²The reported value for water vapor is at standard conditions. In reality, the pressure (and density) will be lower, but this difference is negligible compared to the difference between water vapor and water.

the total capacity of the 14-bit detector was utilized here. However, this range increases in the downstream direction with the increasing diameter of the venturi cross-section. The wiggles in the absolute intensities (Fig. 4.10(inset)) are due to different sensitivities of multiple pixels in the primary detector (described in Section 4.3.1) and not random noise.

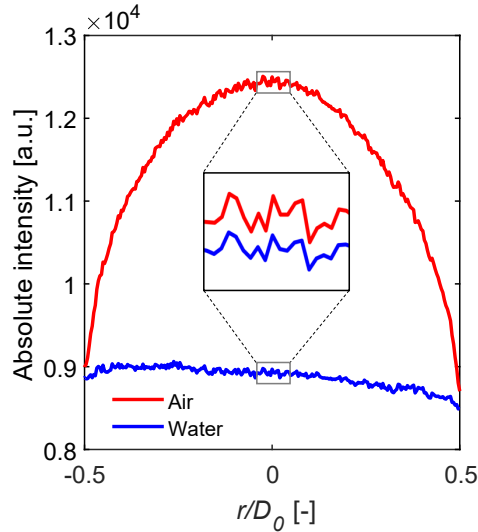


Figure 4.10: Profiles of the absolute intensities recorded on the X-ray detectors at one streamwise location: the venturi throat. The two cases considered are when the venturi contains solely air and solely water.

For purely monochromatic X-rays, this two-point calibration would have been sufficient to determine all possible values in between vapor/air and water. To ensure accurate results for our X-ray source, additional calibration experiments were performed with increasing volume fractions in between the two extremes. An additional reason is that the expected void fractions are low, so we would be close to one of the calibration points, making the result very sensitive to calibration errors. To perform these additional calibration experiments, empty calibration cylinders (air-filled plastic cylinders) of four different diameters and negligible wall thicknesses were inserted into the venturi, which was filled with water. The calibration cylinders were aligned with the axis of symmetry of the venturi. The diameters of calibration cylinders were measured with an accuracy of ± 0.5 mm. Calibration was then performed at multiple streamwise locations by recording the mean intensity along the centerline of the cylinders. As the diameters of the calibration cylinders were known, the intensity at the center of the cylinder is related to the line-integrated void fraction. In Fig. 4.11, the calibration relation is shown for seven X/L locations selected from the full length of the venturi. The diameter of the venturi increases with increasing X/L, which corresponds to the different attenuation of X-rays due to the presence of more water and less PMMA. However, by dividing the recorded intensity by the reference intensity this effect of different attenuation cancels out. A linear fit through mean can be seen in the Fig. 4.11. The standard error from the mean for the measured intensities for the various calibration cylinders was found to be less than 3.65%,

which is considered acceptable. The relationship obtained between the logarithm³ of the intensities in the X-ray images and the diameter of calibration cylinders (known void fraction) is used to determine the calibration constant, which is then used to calculate the vapor distribution on the reconstructed CT slices (explained in the upcoming paragraph).

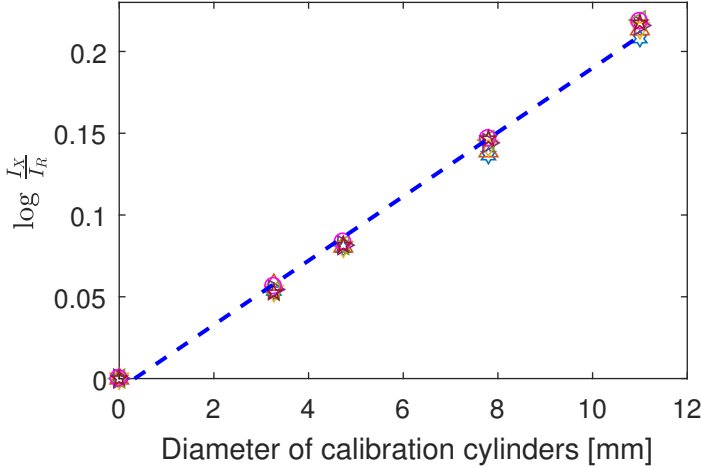


Figure 4.11: The logarithm of the ratio of intensities ($\frac{I_X}{I_R}$) versus the diameters of the calibration cylinders representing the actual line-integrated void fractions. The measured grayscale intensity is based on an average of 3700 images.

To use these calibration results of line-integrated quantities for our CT results, a procedure was followed that is a common method in the X-ray community (selectively Bauer et al. (2018); Duke et al. (2015); Mitroglou et al. (2016)). The images from the CT reconstruction provide 3D information. To find the void fraction for each voxel, we collapse the data back to 2D X-ray images, i.e. projecting the tomographic reconstruction onto a 2D plane. We can then assign an integrated void fraction to each projected intensity using the calibration curve. This integrated void fraction is subsequently redistributed over the constructed slice, so that the sum of the voxel values matches the projected void fraction.

Fig. 4.12(a) shows the time-averaged X-ray intensity data for a calibration cylinder. This panel is before tomographic reconstruction i.e. a projection along the line between source and detector. Fig. 4.12(b) shows the reconstructed CT slice at an axial position (red line in Fig. 4.12(a)) with the void fractions. A very homogeneous distribution of air can be seen. Here, $\alpha = 0.995 \pm 0.004$, which shows a maximum error of approximately 0.9% with respect to real void fraction, which is considered acceptable. This error is associated with various facts, the most notable being: the reconstruction method, which is an approximate approach, and the variation of noise in the X-ray images. The diameter of the cylinder measured from the CT slice also compares very well to the known diameter

³As the intensity decays exponentially in a given medium (cf. the Lamber-Beer law), taking the logarithm of the intensity leads to a linear relation between attenuation (and intensity) and the void fraction.

of the cylinder with an error of less than 1%.

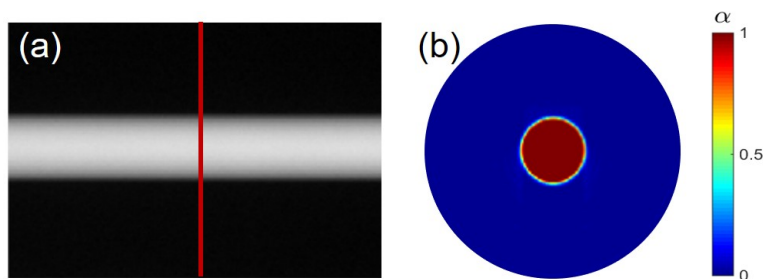


Figure 4.12: (a) Time-averaged X-ray image of the calibration cylinder (air is light gray and liquid is black). (b) Cross-sectional CT image presented as a side-view cut with $\alpha = 0.995 \pm 0.004$. The red region indicates the presence of vapor (air in this case) and the blue region indicates the presence of liquid.

4

4.4.3. CROSS-SECTIONAL DISTRIBUTION OF VOID FRACTION

This section presents the quantitative void fraction measurements for the bubbly shock mechanism and the re-entrant jet mechanism. The results shown are a mix of qualitative high-speed shadowgraphy images and quantitative time-averaged X-ray measurements. Their combination will assist in interpreting the flow behavior in the venturi.

High-speed shadowgraphy was performed in a prior study, which also provides all relevant technical details (Jahangir et al., 2018). A bright, uniform illumination source is placed behind the venturi and a CMOS camera is used to capture images. Vapor bubbles will block light and thus appear as dark spots in the image. This way the presence and position of vapor cavities can be determined. A framerate of 9000 Hz is used in combination with an exposure time of 1/9000 Hz.

In Fig. 4.13, video frames of the bubbly shock mechanism are presented. The flow direction is from left to right. The light gray regions indicate the presence of liquid and the dark gray areas indicate the presence of cavity (vapor). A case with cavitation number of $\sigma = 0.40$ ($u_0 = 13.7$ m/s and $p = 40$ kPa) is shown. In Fig. 4.13(a) and (b), a growing cavity can be seen (left side of sub-panels) with the previously shedded cavity (right side of sub-panels). In the subsequent frame, the cavity collapses and emits a pressure wave. When the pressure wave reaches the venturi throat, the cavity detaches, as shown in Fig. 4.13(d). This is the start of the next cycle of the periodic shedding process.

The corresponding void fraction distribution slices for the bubbly shock mechanism are shown in Fig. 4.14(a) - (f). The CT slices are reconstructed at the axial positions indicated in the time-averaged X-ray image. The flow direction is from left to right. The light gray regions indicate the presence of a cavity (vapor) and the black areas indicate the presence of liquid in the X-ray image, while the red regions show cavity and blue regions show the presence of liquid in the CT slices. Quantitative measures for the total surface area of vapor and liquid A_V and A_L are also obtained for each CT slice. The total surface area of vapor for each CT slice is given by $A_V = \iint \alpha(y, z) dy dz \approx [\sum \sum \alpha(y, z)] dy dz$, where dy and dz are the physical dimensions of a reconstructed voxel. A_L follows from the nominal local cross-sectional area of the venturi, minus the area covered by vapor.

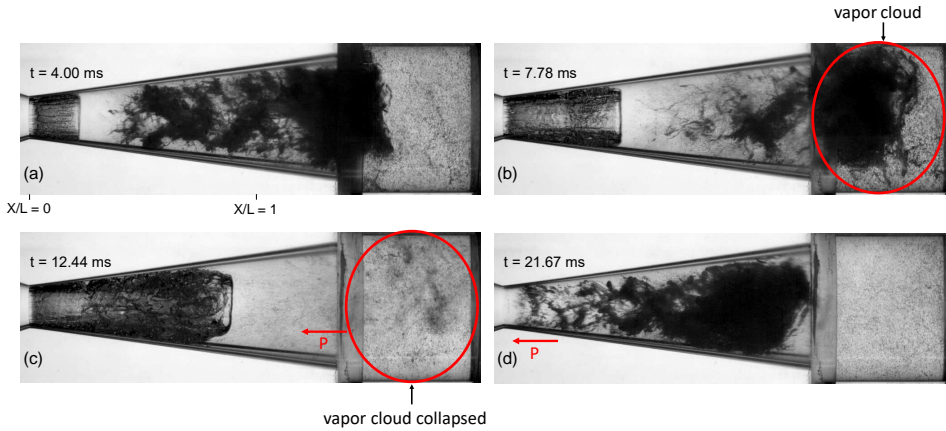


Figure 4.13: Video frames of bubbly shock development at $\sigma = 0.40$. The light gray regions indicate the presence of liquid and the dark gray areas indicate the presence of cavity (vapor). (a,b) A growing cavity can be seen (left side of sub-panels) with the previously shed cavity (right side of sub-panels). (c) In the subsequent frame the cavity collapses and a pressure wave is emitted (P). (d) Cavity detachment can be observed when the pressure wave reaches the throat.

A core of liquid can be seen in a short distance just downstream of the venturi throat with a concentrated ring of cavitation around it (Fig. 4.14(a)). This thin film of cavitation has the maximum void fraction of $\alpha_{max} = 0.86$. The center of annulus consists of pure liquid without any cavitation (threshold of liquid being set at $\alpha = 0.016$, explained in Section 4.4.2). Further downstream of the venturi throat, the vapor film starts to become more like a cloud as its thickness increases, as shown in Fig. 4.14(b) and (c). A decrease in the maximum void fraction can be seen; however, the average void fraction is similar in both CT slices (Fig. 4.15).

The cavitation bubbles are present in the liquid core further downstream, hinting at the appearance of a thick cloud of vapor, as shown in Fig. 4.14(d) and (e). A diffused interface between the liquid and vapor can be also be seen. The vapor film which was previously attached to the circumferential wall can now be seen turning into a cloud and detaching from the wall (Fig. 4.14(e)). The value of α_{max} steadily decreases with increasing X/L . The cavitation cloud becomes thicker as the liquid core decreases. Note that these are time-averaged void fractions. This is relevant, in particular further downstream, as the cavitation is not present at each instance for a given location: it alternates between liquid and vapor (Fig. 4.13). The instantaneous void fractions will likely be much higher than the time-averaged data reported here.

In Fig. 4.14(f), it can be seen that only cloud cavitation appears at the exit of the venturi. The maximum void fractions (α_{max}), the mean void fractions (α_{mean}) and the total surface areas (A_V and A_L) are shown in Fig. 4.15 and Fig. 4.16. The value of A_V rapidly increases with the increase in axial location until $X/L \approx 0.65$. Here, a maximum of A_V is found of 134.7 mm^2 . With a further increase in X/L , a slight decrease in A_V can be seen. At $X/L = 0.9$, the value of A_V is 129 mm^2 , vapor and liquid are thoroughly mixed with an average void fraction of about 12% and a maximum void fraction of about 16%.

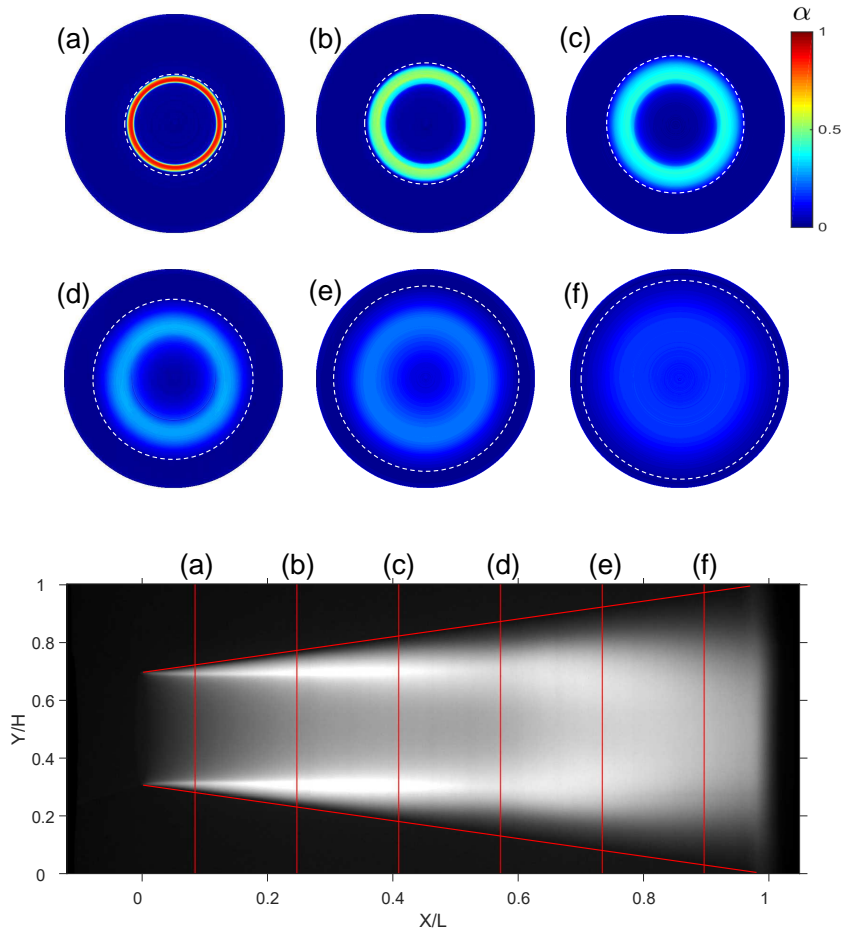


Figure 4.14: (Bottom) Time-averaged X-ray image of an experiment in the bubbly shock regime. The light gray regions indicate the presence of vapor and the black regions indicate the presence of liquid. The cavitation number is $\sigma = 0.40$ ($u_0 = 13.7$ m/s and $p = 40$ kPa). (a-f) Quantitative measurements of time-averaged void fractions at six different locations along the venturi.

We should not ignore the fact that some part of these void fractions may be attributed to non-condensable gas, instead of just water vapor. The diffusion rate into the cavity is related to the dissolved gas content, the local cavity pressure, and the flow within and around the cavity (Lee et al., 2016). However, to minimize this effect, the measurements were performed at relatively low dissolved gas content (described in Section 4.2.2).

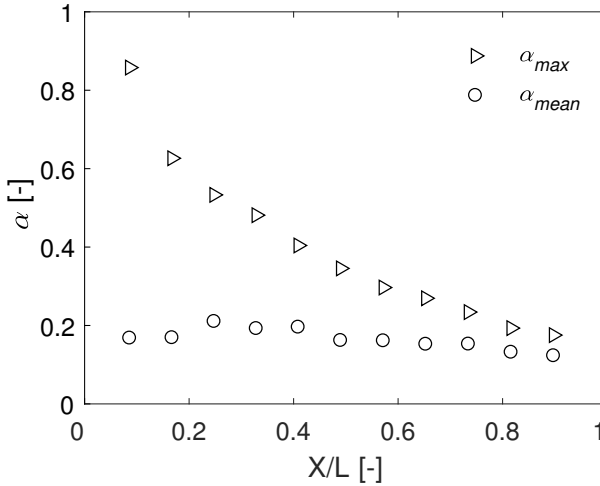


Figure 4.15: Time-averaged mean and maximum void fractions of vapor as a function of position for $\sigma = 0.40$.

A second case is selected, but this time in the re-entrant jet dominant regime. The video frames for $\sigma = 1$ ($u_0 = 13.5$ m/s and $p = 90$ kPa) are shown in Fig. 4.17. One full cycle of the re-entrant jet mechanism and shedding can be observed. The re-entrant jet develops with the growing cavity (Fig. 4.17(a) and (b)). The re-entrant jet front can be recognized by the chaotic interface, which can be seen by the arrow. Then the jet front starts to propagate in the direction of the venturi throat, as shown in Fig. 4.17(c). The re-entrant jet reaches the throat and the entire cavity detaches from the throat (Fig. 4.17(d)). This marks the start of the next cycle.

The corresponding void fraction distribution slices for the re-entrant jet mechanism are shown in Fig. 4.18(a) - (f). Note the difference in color scale compared to Fig. 4.14. The CT slices are similarly reconstructed at the axial positions indicated in the time-averaged X-ray image. It is evident from the X-ray image that the cavity length is smaller as compared to the bubbly shock case. Therefore, the axial locations for the CT reconstruction are selected accordingly.

One thing that is clearly visible within the CT slices is that the α values for this regime are smaller than those in the bubbly shock governed regime. Once again the core consisting of liquid can be seen in a short distance just downstream of the venturi throat (Fig. 4.18(a)). The cavitation ring at the circumferential wall is still present; however, its void fraction is less pronounced, compared to Fig. 4.14. Here, the maximum void fraction is 45%, which is approximately half the void fraction of the bubbly shock governed case. It can also be seen that the extent of the cavitation structure is slightly growing from

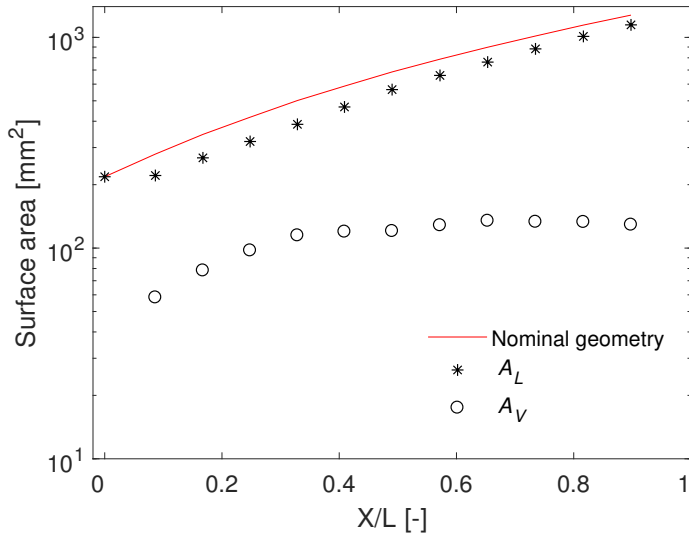


Figure 4.16: The total area covered by vapor (A_V) and liquid (A_L) as a function of position for $\sigma = 0.40$. Also shown is the local cross-sectional area of the venturi geometry.

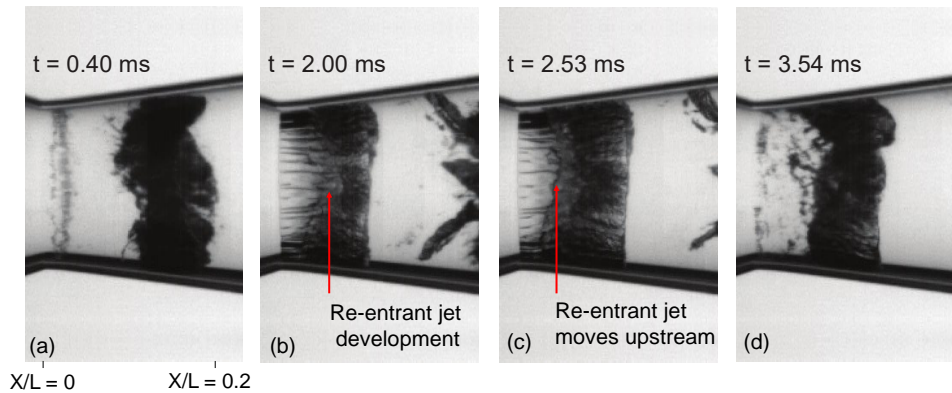


Figure 4.17: Video frames of re-entrant jet development at $\sigma = 1$. In (a) and (b), cavity development can be seen and the re-entrant jet starts to develop. The jet front can be recognized by the chaotic interface, which can be seen by the arrow. The propagation of the jet front towards the venturi throat can be seen in (c). In the end, cavity detachment is caused by the re-entrant jet as can be observed in (d).

Fig. 4.18(a) to (c) but its shape is overall conserved. A decrease in the α_{max} can be seen downstream of the venturi throat (Fig. 4.18(b)-(d)). However, the average void fraction does not decrease within these three CT slices. In Fig. 4.18(e) and (f), the cavitation ring changes into cloud cavitation before it vanishes. This proves once more the capabilities of this measurement method.

The maximum and mean void fractions and the total surface areas are shown in

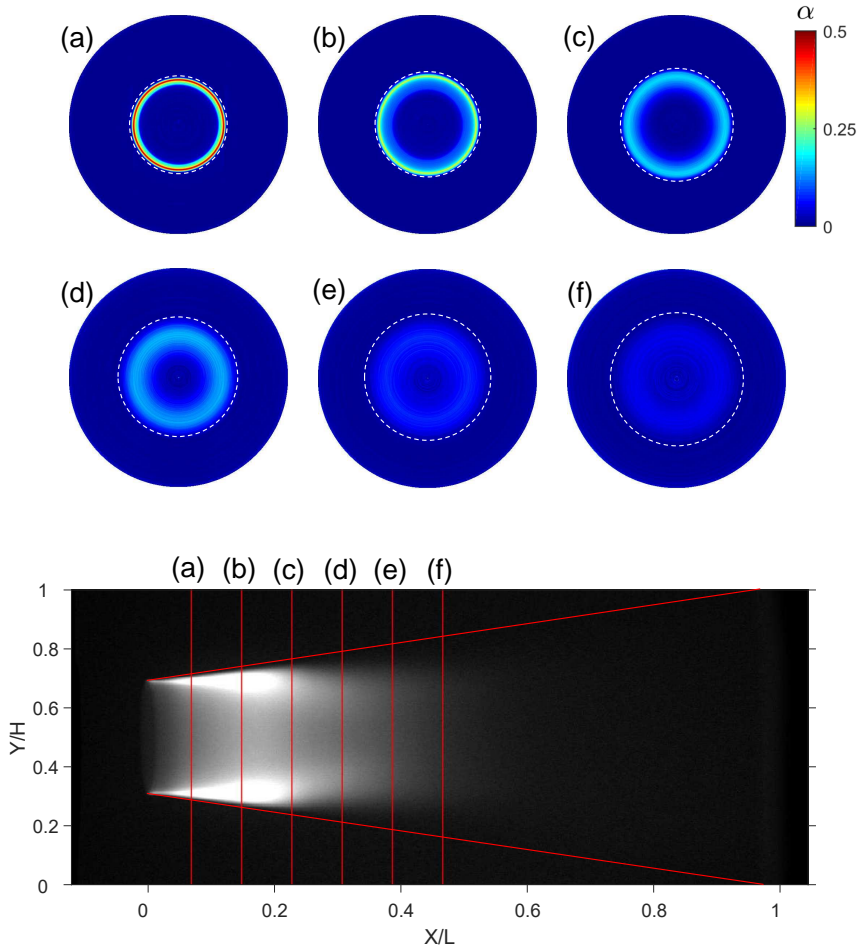


Figure 4.18: (Bottom) Time-averaged X-ray image of an experiment in the re-entrant jet regime. The light gray regions indicate the presence of vapor and the black regions indicate the presence of liquid. For this case $\sigma = 1$ (corresponding to: $u_0 = 13.5$ m/s and $p = 90$ kPa). (a-f) Quantitative measurements of time-averaged void fractions at six different locations along the venturi. Note the difference in the color scale compared to Fig. 4.14.

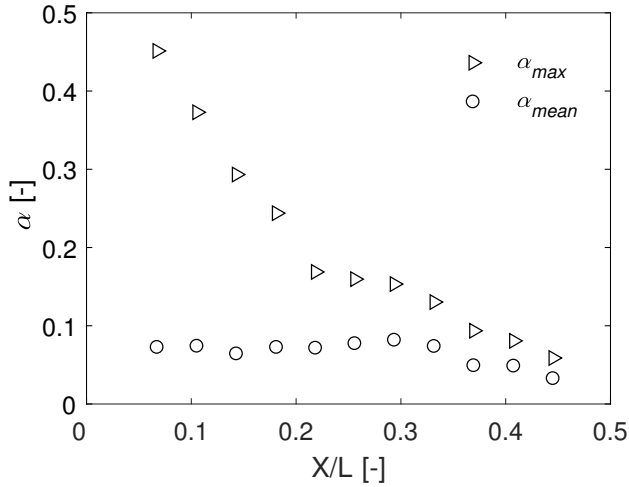


Figure 4.19: Time-averaged mean and maximum void fractions of vapor as a function of position for $\sigma = 1$.

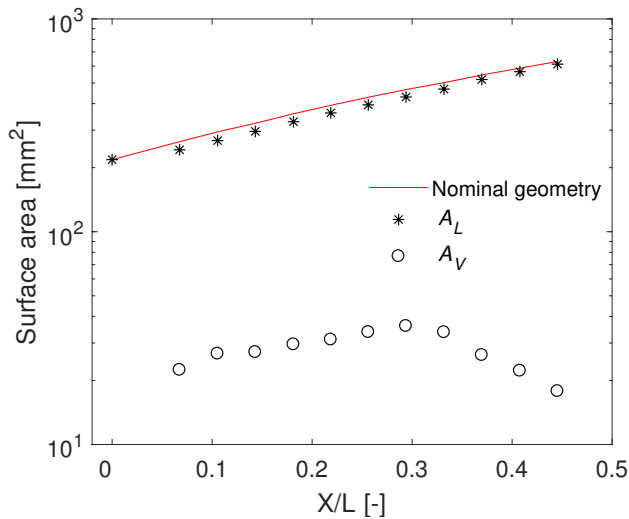


Figure 4.20: The total area covered by vapor (A_V) and liquid (A_L) as a function of position for $\sigma = 1$. Also shown is the local cross-sectional area of the venturi geometry.

Fig. 4.19 and Fig. 4.20. A_V is the same as the difference between A_L and the nominal local cross-section area, representing the flow blockage caused by cavitation. It is clear that the flow blockage caused by the bubbly shock regime (Fig. 4.16) is more significant compared to the re-entrant jet regime (Fig. 4.20). This agrees with the observed difference in pressure drop, see the values of K in the inset of Fig. 4.9. An increase in A_V can be seen until $X/L \approx 0.3$. Here, $A_V = 33.7 \text{ mm}^2$. The maximum value of A_V is found to be approximately 4

times smaller than the maximum value of A_V in the bubbly shock case. This is a major new insight, as the high-speed shadowgraphy showed fairly similar (time-averaged) data. The value of A_V starts to decrease sharply as we move further downstream and reaches 17.8 mm^2 at $X/L = 0.45$. Here, the maximum void fraction is found to be 6% (Fig. 4.18(f)), which is quite low as compared to the bubbly shock case. It also hints at the presence of a lower void fraction downstream of the venturi in the re-entrant jet regime as compared to the bubbly shock regime.

4.5. CONCLUSIONS AND OUTLOOK

In this chapter, the phenomenon of cavitation was examined by CT measurements of the flow through a venturi. Time-averaged void fractions were obtained after a detailed image correction and calibration procedure. More information about the cavitation development is extracted using the cross-sectional CT measurements as compared to the high-speed shadowgraphy. We can now quantify the radial geometric features of this complex two-phase flow. The void fraction downstream of the venturi in the bubbly shock mechanism is found to be more than twice compared to the re-entrant jet mechanism. Moreover, the vapor phase mixes with the liquid phase downstream of the venturi, resulting in cloud-like cavitation. This data will be essential to validate our assumptions regarding the physical mechanisms. Furthermore, it will be helpful for the validation of numerical studies.

Using the CT reconstruction, we are able to explore the internal structures of the cavitating flow and to quantify the void fractions. The combination of high-speed shadowgraphy data and CT data gives unprecedented insight into this complex multiphase flow. Despite the new insight that this approach generated, there still is a major limitation: the current study was performed using the time-averaged X-ray measurements; hence, further studies are needed to investigate the transient behavior of the vapor cloud. These investigations are planned and will be performed using phase-locked X-ray measurements.

REFERENCES

- Bauer, D., Barthel, F., and Hampel, U. (2018). High-speed X-ray CT imaging of a strongly cavitating nozzle flow. *Journal of Physics Communications*, 2(7):075009.
- Bauer, D., Chaves, H., and Arcoumanis, C. (2012). Measurements of void fraction distribution in cavitating pipe flow using X-ray CT. *Measurement Science and Technology*, 23(5):055302.
- Chaouki, J., Larachi, F., and Duduković, M. P. (1997). Noninvasive tomographic and velocimetric monitoring of multiphase flows. *Industrial & Engineering Chemistry Research*, 36(11):4476–4503.
- Chen, G. H., Wang, G. Y., Hu, C. L., Huang, B., and Zhang, M. D. (2015). Observations and measurements on unsteady cavitating flows using a simultaneous sampling approach. *Experiments in Fluids*, 56(2):32.

- Dash, A., Jahangir, S., and Poelma, C. (2018). Direct comparison of shadowgraphy and X-ray imaging for void fraction determination. *Measurement Science and Technology*, 29(12):125303.
- Duke, D. J., Swantek, A. B., Kastengren, A. L., and Powell, C. F. (2015). X-ray Diagnostics for Cavitating Nozzle Flow. *Journal of Physics: Conference Series*, 656(1):012110.
- Dular, M. and Petkovšek, M. (2015). On the mechanisms of cavitation erosion – coupling high speed videos to damage patterns. *Experimental Thermal and Fluid Science*, 68:359 – 370.
- Franc, J.-P. and Michel, J.-M. (2006). *Fundamentals of cavitation*, volume 76. Springer Science & Business Media.
- Ganesh, H., Mäkiharju, S. A., and Ceccio, S. L. (2016). Bubbly shock propagation as a mechanism for sheet-to-cloud transition of partial cavities. *Journal of Fluid Mechanics*, 802:37–78.
- Hayashi, S. and Sato, K. (2014). Unsteady Behavior of Cavitating Waterjet in an Axisymmetric Convergent-Divergent Nozzle: High Speed Observation and Image Analysis Based on Frame Difference Method. *Journal of Flow Control, Measurement & Visualization*, 2:94–104.
- Helmi, A., Wagner, E., Gallucci, F., van Sint Annaland, M., van Ommen, J., and Mudde, R. (2017). On the hydrodynamics of membrane assisted fluidized bed reactors using X-ray analysis. *Chemical Engineering and Processing: Process Intensification*, 122:508 – 522.
- Holder, D. S. (2004). *Electrical impedance tomography: methods, history and applications*. CRC Press.
- Jahangir, S., Hogendoorn, W., and Poelma, C. (2018). Dynamics of partial cavitation in an axisymmetric converging-diverging nozzle. *International Journal of Multiphase Flow*, 106:34 – 45.
- Kastengren, A. and Powell, C. F. (2014). Synchrotron X-ray techniques for fluid dynamics. *Experiments in Fluids*, 55(3):1686.
- Ketcham, R. A. and Carlson, W. D. (2001). Acquisition, optimization and interpretation of X-ray computed tomographic imagery: applications to the geosciences. *Computers & Geosciences*, 27(4):381 – 400.
- Khelifa, I., Vabre, A., Hočevár, M., Fezzaa, K., Fuzier, S., Roussette, O., and Coutier-Delgosha, O. (2017). Fast X-ray imaging of cavitating flows. *Experiments in Fluids*, 58(11):157.
- Laberteaux, K. R., Ceccio, S. L., Mastrocola, V. J., and Lowrance, J. L. (1998). High speed digital imaging of cavitating vortices. *Experiments in Fluids*, 24(5):489–498.
- Lee, I. H., Mäkiharju, S. A., Ganesh, H., and Ceccio, S. L. (2016). Scaling of gas diffusion into limited partial cavities. *Journal of Fluids Engineering*, 138(5):051301.

- Long, X., Zhang, J., Wang, J., Xu, M., Lyu, Q., and Ji, B. (2017). Experimental investigation of the global cavitation dynamic behavior in a venturi tube with special emphasis on the cavity length variation. *International Journal of Multiphase Flow*, 89:290–298.
- Mäkiharju, S. A., Gabillet, C., Paik, B.-G., Chang, N. A., Perlin, M., and Ceccio, S. L. (2013). Time-resolved two-dimensional X-ray densitometry of a two-phase flow downstream of a ventilated cavity. *Experiments in Fluids*, 54(7):1561.
- Maurer, S., Wagner, E. C., Schildhauer, T. J., van Ommen, J. R., Biollaz, S. M., and Mudde, R. F. (2015). X-ray measurements of bubble hold-up in fluidized beds with and without vertical internals. *International Journal of Multiphase Flow*, 74:118 – 124.
- Mitroglou, N., Lorenzi, M., Santini, M., and Gavaises, M. (2016). Application of X-ray micro-computed tomography on high-speed cavitating diesel fuel flows. *Experiments in Fluids*, 57(11):175.
- Mudde, R. F., Alles, J., and van der Hagen, T. H. J. J. (2008). Feasibility study of a time-resolving X-ray tomographic system. *Measurement Science and Technology*, 19(8):085501.
- Peng, C., Tian, S., and Li, G. (2018). Joint experiments of cavitation jet: High-speed visualization and erosion test. *Ocean Engineering*, 149:1–13.
- Tomov, P., Khelladi, S., Ravelet, F., Sarraf, C., Bakir, F., and Vertenoeuil, P. (2016). Experimental study of aerated cavitation in a horizontal venturi nozzle. *Experimental Thermal and Fluid Science*, 70:85–95.
- van Aarle, W., Palenstijn, W. J., Cant, J., Janssens, E., Bleichrodt, F., Dabrovolski, A., De Beenhouwer, J., Batenburg, K. J., and Sijbers, J. (2016). Fast and flexible X-ray tomography using the ASTRA toolbox. *Optics express*, 24(22):25129–25147.
- Wang, D., Song, K., Fu, Y., and Liu, Y. (2018). Integration of conductivity probe with optical and X-ray imaging systems for local air–water two-phase flow measurement. *Measurement Science and Technology*, 29(10):105301.

5

CONCLUSIONS AND PERSPECTIVES

The main aim of this thesis was to understand the dynamics of partial cavitation. Different experimental techniques are employed to understand this flow phenomenon. Since it is opaque to visible light, we employed other techniques that rely on other parts of the electromagnetic spectrum, such as X-rays and MRI for which the fluid and cavitating bubbles are not opaque. The results presented in different chapters of the thesis exhibit significant progress in the field of cavitation. Each chapter of this thesis has its own conclusions as it is based on individual publications. In this chapter, we give a brief overview of the principal findings of this thesis and recommendations for future research.

5.1. CONCLUSIONS

Partial cavitation dynamics are observed in the venturi using high-speed shadowgraphy. Different cavitation regimes are produced systematically by independently altering the global static pressure and flow velocity. The flow blockage increases with decreasing cavitation number ($\sigma = \frac{p - p_v}{\frac{1}{2} \rho u_0^2}$). The cavity lengths and time scales are also functions of the cavitation number. Using the x-t diagrams, it is found that for $\sigma > 0.95$, the periodic cavity shedding is caused by the re-entrant jet mechanism (see Section 2.4.3). The shedding caused by the re-entrant jet mechanism is identified by a stick-slip behavior in the x-t diagram. For $\sigma < 0.75$, the prevalent mechanism for periodic cavity shedding is found to be the bubbly shock mechanism. Both mechanisms are encountered in the transition region, $0.75 < \sigma < 0.95$. The re-entrant jet mechanism is generated by an adverse pressure gradient and a stagnation point at the closure of the cavity. The bubbly shock in the developing cavity is caused by a shock wave, which is transmitted from the previously collapsing cavity. The shock wave velocity in the liquid phase was found to be 900 m/s (shown in Fig. 2.17) and around 15 m/s in the cavity region.

X-ray measurements are conducted to determine the void fractions in the cavitating flow. First, the images from shadowgraphy and X-ray measurements are compared to show the need for X-ray imaging. Correlations are made based on the grayscale intensity values along the streamwise direction for a cavitating flow through the venturi, at three different cavitation numbers of 0.60, 0.72 and 0.88. Three distinct 'correlation regimes' are classified for the flow considered (discussed in Section 3.4). The first region, associated with a swarm of tiny bubbles along the walls, is short in extent with a positive correlation between the grayscale intensity values from the two techniques. The second region, associated with a cavity film growing near the wall, shows more variability across the different cavitation numbers and may display either a positive ($\sigma = 0.60$) or a negative ($\sigma = 0.72$ and 0.88) correlation. The third region, associated with the drifting of the cavity away from the walls towards the central region of the venturi as well as collapse of the cavities, is found beyond the estimated location of the cavity lengths. While shadowgraphy may still return reliable estimates of void fractions in flows resembling the first and third regions, it could lead to improper conclusions about the void fraction profiles in flows that resemble the second region.

A follow-up study considered the role of void fractions in the partial cavitation regimes using X-ray CT. We quantify the radial geometric features of this complex two-phase flow. The void fraction downstream of the venturi in the bubbly shock mechanism is found to be more than twice compared to the re-entrant jet mechanism (see Section 4.4.3). Moreover,

the vapor phase mixes with the liquid phase downstream of the venturi, resulting in cloud cavitation. Using the CT reconstruction, we can explore the internal structure of the cavitating flow. The combination of high-speed shadowgraphy data and time-averaged CT data gives exceptional details of the partial cavitation regimes.

In conclusion, the re-entrant jet mechanism and the bubbly shock mechanism are the main responsible mechanisms for the shedding of cavitation clouds. The re-entrant jet mechanism can be identified by the typical stick-slip behavior and has a comparatively lower void fraction. On the other hand, the bubbly shock mechanism is caused by the shock wave emitted from the violent collapse of the previously shed cavity and has a higher void fraction.

5.2. PERSPECTIVES ON FUTURE RESEARCH

As shown in the previous section, significant insights were obtained in the understanding of partial cavitation regimes. However, there are various open questions and remaining issues. A number of recommendations for improvements and further study are presented in this section.

Flow loop In the present study, all experiments were performed in a closed flow loop. Due to the age of the flow loop and nature of experiments, each separate experiment turned out to require replacement or modification of one or more components. The main concerns in using this experimental facility are the proper degassing of water and sustaining lower static pressure with respect to atmospheric pressure. Any source of leakage (connections or pump) results in changing the operating pressure. To better control the gas content and pressure, it should be made possible to increase and decrease the static pressure in the flow loop without any leakage.

Water quality The main path towards the understanding of cavitation is the study of sources of its excitation. In the current study, measurements were performed using filtered water. Cavitation exhibits different characteristics in fresh water and sea water. The effect of water quality on cavitation inception and radiated pressures are available from the full-scale applications. Recently, the AQUA project has been launched to better understand the effect of water quality on cavitation. This project will be implemented by the Delft University of Technology in collaboration with well-known institutions and industrial partners. The effect of water quality on cavitation will be studied by systematically varying water quality and gas, both in terms of dissolved air content and bubble spectra. These measurements will be performed in the new Multiphase Flow tunnel at the Delft University of Technology. The new Multiphase Flow tunnel makes it possible to vary the water quality by (de-)aerating the water and separating the free air at decreasing working pressures. Three types of working fluid will be applied: clean water, water with a single salt (NaCl) and artificial seawater.

Time-resolved void fractions As mentioned in chapter 4, we are able to quantify the void fractions in the venturi using X-ray CT. The combination of high-speed shadowgraphy data and CT data gives significant insight into this complex multiphase flow. Despite the new insight that this approach generated, there still is a major limitation: the current

study was performed using time-averaged X-ray measurements; hence, further studies are needed to investigate the transient behavior of the vapor cloud. Currently, there is no dedicated X-ray facility available in Delft for time-resolved void fraction measurements. These investigations are planned and will be performed using phase-locked X-ray measurements.

Flow field in cavitating flow PIV measurements were performed in the non-cavitating flow (Section 1.5). However, the production of vapor bubbles makes the flow opaque and PIV is not applicable anymore. Due to the nature of the bubble cloud, magnetic resonance velocimetry (MRV) is well-suited to see the influence of cavitation on the velocity fields. These experiments were performed at the University of Rostock. Initially, the non-cavitating PIV data was compared with the MRV data, and the results were published (John et al., 2020). Measurements were also performed for the cavitating flow. With further increase in flow velocity, the turbulence in the flow increases, which ultimately results in a drop of mean signal intensity. The data acquisition time for these measurements is also very long (hours), so that the flow properties should remain constant over the course of the measurements. Therefore, MRV results for cavitating flow are not fully converged compared to MRV results for non-cavitating flow. In order to get converged mean velocity data in cavitating flows, measurements with longer acquisition times are proposed.

Cavitation erosion Surface erosion is one of the most significant drawbacks of cavitation, as described in Section 1.1. For this purpose, an experimental campaign was conducted in a channel with a semi-circular cylinder obstacle at the Hydraulic Laboratory of ANDRITZ HYDRO in Vevey (Jahangir et al., 2019). The obstacle promotes and localizes cavitation-induced erosion. The flow field behind the semi-circular cylinder was investigated as a characteristic example of bluff bodies, which exhibit a distinct separated vortex flow in their wake. A detailed study on the cavitation dynamics behind the bluff body was published (Ghahramani et al., 2020). The erosion tests were performed using *paint* (stencil ink). Three erosive cases at different cavitation numbers are shown in Fig. 5.1(a) – (c). The flow is from left to right and light gray represents the cavitation region. At lower cavitation number, more intense cavitation can be seen. In Fig. 5.1(d) – (f), the erosion patterns (removal of paint) after 40-60 mins of operation can be seen for the corresponding cavitation numbers. For a high cavitation number, a large number of Karman-vortex-like cavities are shed downstream of the obstacle. This results in a higher number of collapse events and ultimately more erosion. On the other hand, at lower cavitation numbers the erosion took place at the closure line of the cavity. The paint tests provide an efficient and economical way to investigate erosion patterns compared to expensive material loss tests. Using the paint test approach, it is possible to decrease the erosion test period from 75 hours to 60 mins. Painting the lower half of the venturi in combination with high-speed shadowgraphy measurements through the upper half are proposed to investigate surface erosion.

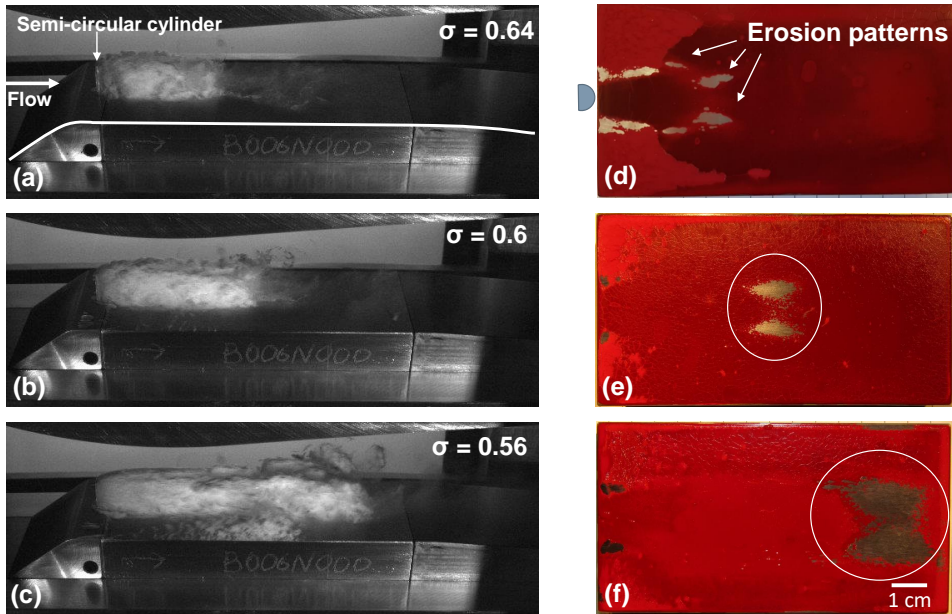


Figure 5.1: (Left) Video frames of cavitating flow behind the semi-circular cylinder. The flow is from left to right and light gray represents the cavitation region. (Right) Photographs representing the corresponding erosion patterns after 40-60 mins of operation (from: Jahangir et al. (2019)).

REFERENCES

- Ghahramani, E., Jahangir, S., Neuhauser, M., Bourgeois, S., Poelma, C., and Bensow, R. E. (2020). Experimental and numerical study of cavitating flow around a surface mounted semi-circular cylinder. *International Journal of Multiphase Flow*, 124:103191.
- Jahangir, S., Ghahramani, E., Neuhauser, M., Bourgeois, S., E Bensow, R., and Poelma, C. (2019). Experimental study of cavitation erosion around a surface-mounted semi-circular cylinder. In *10th International Conference on Multiphase Flow, Rio de Janeiro, Brazil*.
- John, K., Jahangir, S., Gawandalkar, U., Hogendoorn, W., Poelma, C., Grundmann, S., and Bruscheckski, M. (2020). Magnetic resonance velocimetry in high-speed turbulent flows: sources of measurement errors and a new approach for higher accuracy. *Experiments in Fluids*, 61(2):27.

ACKNOWLEDGEMENTS

*If we knew what it was we were doing,
it would not be called research,
would it?*

— Albert Einstein

This thesis would not have been possible without the help of many people. Their support during these four and half years has been a great help. I want to express my gratitude to all of them.

First of all, I am grateful to my daily supervisor and promotor Christian Poelma for providing me the opportunity to pursue my PhD research under his guidance. You showed me the exciting research area of cavitation and the challenges that are required to be addressed experimentally. You were more than helpful in my research, starting from giving me an idea, designing a new experiment, processing the data, and finally correcting my paper drafts (very quickly). I also appreciate the autonomy you granted me to modify the research topic just after a year into the start of the project.

I would also like to thank my second promotor Jerry Westerweel for his support. I very much appreciate that you allowed me to do the experimental work freely in well-equipped Laboratory of Aero & Hydrodynamics. I am also thankful to my PhD committee and reviewers of my papers for taking the time to read and provide their useful comments.

I had the opportunity of collaborating and visiting project partners for a number of months during the course of my PhD. I extend my gratitude to Manolis Gavaises (CITY), Magdalena Neuhauser (ANDRITZ Hydro), Sébastien Bourgeois (ANDRITZ Hydro), Ebrahim Ghahramani (CHALMERS), Martin Bruschewski (University of Rostock) and Kristine John (University of Rostock) for hosting me. Our collaborations lead to a set of works that speaks for itself. Because of you guys, we managed to go hiking in Vevey, have dinners and visit museums in London and sightseeing at the Baltic sea in Rostock. I would also like to acknowledge the support of Rob Mudde (TU Delft) and Evert Wagner (TU Delft) during the X-ray measurements. Your fruitful discussions and hands-on actions lead to improvements in our results.

Several students decided to do their M.Sc. thesis and B.Sc. project with me. I genuinely appreciate their contribution to this work. In particular, I want to mention Willian Hogendoorn (ending up as a PhD colleague), for helping me in two experimental campaigns (shadowgraphy and MRV experiments). In a way, we explored most of this complex multiphase flow phenomena together. I would like to extend my thanks to Udhav Gawan-dalkar, who did the PIV measurements in a very tight schedule. The experimental facility

modifications and upgrades have genuinely been a challenge. I want to thank Jasper Ruijgrok, Jan Graafland and Edwin Overmars for their technical support and Caroline for the administrative help.

Other colleagues that shared in the intriguing topic of cavitation were Sören Schenke, Gem Rotte and Themis Melissaris. Thank you for sharing your thoughts during informal coffee chats, understanding of measurements, and sharing project meetings and conferences at exotic locations.

An achievement is never executed with a single person's effort. I have been blessed with a number of supportive colleagues that were always there to assist me. I would like to thank Amitosh, Mike, Wout, Wouter, Tariq, Sudarshan, Yavuz, Lina, Andries, Jerke, Greta, Henk, Ankur, Pepijn, Melika, Arati, Maurice, Arnoud, Pedro, Ernst Jan, Mark, Gerrit, Gosse, Mathieu, René Delfos, Marieke, Manu, Florian, Jasper Tomas, Sita, Koen, Guillermo, John, Parviz, Junaid, Daniel, Wim-Paul, Ruud, Gema, Göktürk, Jana, Ankur, Haoyu Li, Bob, Willem, Teng, Luuk, Bidhan, Angeliki, Christian Potma and Swaraj. I very much enjoyed working in the same lab with you.

I would also like to thank all my Pakistani friends in Delft: Imran, Irfan, Hussam, Tabish, Shakeel, Qasim, Nauman, Tanveer, Aftab, Mohsan, Fahim, Hamid, Aitazaz, Hassan, Sarmad, Hameed and their families for all the gatherings, BBQ's and card games. I never felt away from home.

A big thanks to my parents, brothers and sister for supporting me throughout the years. Their lifetime hard work and prayers made me capable enough to own this degree. My final expression of appreciation goes to my wife: Aleeha. Aleeha! I do not have words to express my gratitude towards you. Without you, I would not have had the peace of mind to work. I thank you for your understanding and cooperation, especially during the busy times of my PhD process. Rameen (my daughter), thank you so much for bringing joy and happiness in our lives.

Saad Jahangir
Delft, May 2020

CURRICULUM VITÆ

Saad JAHANGIR

20-09-1989 Born in Lahore, Pakistan.

EDUCATION

1996-2005 Primary education
Crescent Model Higher Secondary School, Lahore, Pakistan

2005-2007 Secondary education
Forman Christian College, Lahore, Pakistan

2007-2011 B.Sc. in Mechanical Engineering
University of Engineering and Technology Lahore, Pakistan

2012-2015 M.Sc. in Power Engineering
Brandenburg University of Technology Cottbus - Senftenberg, Germany

2015-2020 Ph.D. Delft University of Technology, The Netherlands
Thesis: Experimental Investigation of Partial Cavitation
Promotors: C. Poelma & J. Westerweel

LIST OF PUBLICATIONS

7. **S. Jahangir**, E. Ghahramani, M. Neuhauser, S. Bourgeois, R. E. Bensow, C. Poelma, *Experimental investigation of cavitation erosion behind a bluff body*, (in preparation).
6. M. Brunhart, C. Soteriou, M. Gavaises, I. Karathanassis, P. Koukouvinis, **S. Jahangir**, C. Poelma, *Investigation of cavitation and vapor shedding mechanisms in a Venturi nozzle*, (submitted to Physics of Fluids).
5. E. Ghahramani, **S. Jahangir**, M. Neuhauser, S. Bourgeois, C. Poelma, R. E. Bensow, *Experimental and numerical study of cavitating flow around a surface mounted semi-circular cylinder*, International Journal of Multiphase Flow **124**, 103191 (2020).
4. K. John, **S. Jahangir**, U. Gawandalkar, W. Hogendoorn, C. Poelma, S. Grundmann, M. Bruscheckski, *Magnetic resonance velocimetry in high-speed turbulent flows: sources of measurement errors and a new approach for higher accuracy*, Experiments in Fluids **61**, 27 (2020).
3. **S. Jahangir**, E.C. Wagner, R.F. Mudde, C. Poelma, *Void fraction measurements in partial cavitation regimes by X-ray computed tomography*, International Journal of Multiphase Flow **120**, 103085 (2019).
2. A. Dash, **S. Jahangir**, C. Poelma, *Direct comparison of shadowgraphy and x-ray imaging for void fraction determination*, Measurement Science and Technology **29**(12), 125303 (2018).
1. **S. Jahangir**, W. Hogendoorn, C. Poelma, *Dynamics of partial cavitation in an axisymmetric converging-diverging nozzle*, International Journal of Multiphase Flow **106**, 34-45 (2018).